The University of Nottingham

UNITED KINGDOM · CHINA · MALAYSIA

NTEC

Nottingham Transportation Engineering Centre

Energy harvesting pavements using air convection

Andrea Chiarelli, M.Sc.

Thesis submitted to The University of Nottingham

for the degree of Doctor of Philosophy

July 2016

Dedicated to my wife Sara and to my family.

Thank you all for the never-ending support!

Abstract

Pavements are one of the most important components of modern civil infrastructure systems. Being constantly exposed to weather conditions, pavements may be subject to heating and cooling cycles, which vary as a function of the location and are proven to reduce the lifespan and reliability of our transport infrastructure. The most extreme effects of weather are generally seen in the form of overheating of the paving materials or freezing of the pavement surface.

In this Thesis, natural convection of air is considered as a means to harvest heat from pavements during hot periods and to provide heat to them when the weather is cold. In the research presented, a buoyancy-driven air flow is allowed through metal pipes installed under an asphalt wearing course. The analysis of the phenomena at work is performed from an experimental, computational, and theoretical point of view.

The main contribution to research provided by this Thesis it that the experiments performed show that a convection-powered air flow can be effectively used for the reduction or increase of pavement temperatures up to about ± 5°C. Moreover, the effects of variations in the design of energy harvesting pavements are quantified and discussed, proving that the installation of all pipes in a single row under the wearing course of a pavement is the overall best solution for the implementation of this technology. Finally, CFD simulations

suggest that the air pores that are naturally present in asphalt mixtures are not suitable to allow the air flow required for convection-powered energy harvesting, due to both fluid-dynamic and practical reasons.

Keywords: energy harvesting, asphalt pavements, temperature management, natural convection, asphalt pores.

Acknowledgements

The present work was carried out at the Nottingham Transportation Engineering Centre (NTEC) at the University of Nottingham under the supervision of Dr. Alvaro García and Mr. Andrew Dawson. The preparation of this Thesis was possible thanks to their support and to the collaboration of a number of colleagues at NTEC and in other research groups.

I would like to thank my supervisors for their interest and availability throughout my studies at the University of Nottingham, as they never stopped encouraging me to dig deeper into the topics of my research and to further improve the quality of my work.

I would also like to thank the technical staff at NTEC, specifically J. Watson, R. Blakemore, and M. Barrett, who always supported my ideas and helped me build the experimental equipment that was used to perform the research described in this Thesis. Thanks are also due to Chris Fox, who helped me perform the X-ray CT scans required for my work, and Martin Corfield, who allowed me to use his research equipment at the University. In addition, I would like to thank the Centre Manager K. Sanderson, who assisted me whenever I needed help for administrative matters.

My gratitude goes to the University of Nottingham, too, for providing the funds for my studies, and to the IWHM Bernard Butler Trust Fund, which awarded me a grant for the purchase of equipment for my research.

Finally, I would like to extend my sincerest thanks to my wife Sara, to my family in Italy, and to all my friends, for always supporting my choices and helping me when I most needed it.

Contents

List of Figures

List of Tables

List of Symbols and Abbreviations

The next list describes several symbols and abbreviations that will be later used within the body of the document.

Energy Harvesting Pavements

α absorptivity , (-)

ε emissivity , (-)

η efficiency , (-)

η_{th} Carnot factor , (-)

κ permeability , (m^2)

μ dynamic viscosity , (kg/(m s))

ρ density , (kg/m^3)

σ Stefan-Boltzmann constant , ($W/(m^2 K^4)$)

τ tortuosity , (-)

A area , (m^2)

B exergy , (J)

D diameter , (m)

f_D Darcy Friction Factor , (-)

Gr Grashof number , (-)

L length , (m)

Nu Nusselt number , (-)

Pr Prandtl number , (-)

Q thermal energy , (J)

Ra Rayleigh number , (-)

Re Reynolds number , (-)

S Sutherland's constant , (K)

T temperature , (K)

V volume , (m^3)

c_p specific heat capacity , (J/(kg K))

g gravitational acceleration , (m/s^2)

h convective heat transfer coefficient , ($W/(m^2 K)$)

h_{fg} latent heat of vapourisation , (J/kg)

k thermal conductivity , (W/(m K))

m mass , (kg)

$\dot{m}$ mass flow , (kg/s)

$\dot{m}''$ mass flow per unit area , ($kg/(s\ m^2)$)

p pressure , (Pa)

q heat flux , (W)

q'' heat flux per unit area , (W/m^2)

q_v volumetric heat generation , (W/m^3)

r Pearson's correlation coefficient , (-)

t time , (s)

u velocity in x direction , (m/s)

v velocity in y direction , (m/s)

w velocity in z direction , (m/s)

x x coordinate , (m)

y y coordinate , (m)

z z coordinate , (m)

Abbreviations

CFD Computational Fluid Dynamics

GSHS Ground Source Heat Simulator

UHI Urban Heat Island

CHAPTER 1

Introduction

1.1 What is energy harvesting?

In the past years, it has become increasingly clear that we are surrounded by a large amount of energy that could be somehow extracted and used for a number of purposes. This "free" energy can be either immediately available or stored in the environment and it is found in different forms, including:

- thermal energy;
- solar energy;
- wind energy;
- tidal energy;
- mechanical energy.

If the energy that is available in the environment in any of these forms is collected for a chosen purpose, the term energy harvesting is commonly used. Based on the kind of energy that is considered, it can be used as is (this is what happens with thermal energy, i.e., heat, in most cases) or it can be converted into something more valuable such as electricity (e.g., in the case of solar and wind power generation).

In this Thesis, the focus will be on the thermal energy. Once thermal en-

ergy is harvested or obtained from a chosen source, it can be exploited in two alternative ways, i.e.:

- heat can be used as is, as long as it is required for a given purpose, e.g., to satisfy the heating needs of a building;
- heat can be converted into electricity, however, this is done only with high temperature heat sources, e.g., in the case of heat recovery steam generators.

Both approaches require specific technical solutions to be implemented, but an efficient conversion of heat into electricity usually involves higher investments. As a result, this is done only in specific cases, while the use of thermal energy, as is, is both technically simpler and more widespread.

1.2 Energy and asphalt pavements

It is not very common to read about asphalt pavements and energy in the same context. The reason for this is that asphalt pavements, like everything else in the environment, accumulate and emit energy continuously, but this is mostly treated as an inevitable fact. Disregarding pavements when talking about energy is understandable, as the thermal energy accumulated in them is clearly different from, e.g., coal or natural gas. However, it would be naive to ignore an energy source today, as society is developing at a very high pace and the demand for energy is continuously increasing.

The energy accumulated in pavements is in the form of heat and it is present only during warm or hot periods. As a result, pavements can be considered as a time-dependent source of energy that needs to work as infrastructure at the same time.

Harvesting the heat available in an asphalt pavement can be approached in

Table 1.1: Research objectives of the Thesis and approach chosen.

Objective number	Objective	Approach
1	Proving the feasibility of energy harvesting in asphalt pavements	Experimental
2	Studying the effect of variations in the design of energy harvesting prototypes	Experimental and computational
3	Studying a possible construction technique with precast concrete	Experimental and computational
4	Finding an application for the air channels during cold weather	Experimental and computational
5	Evaluating the effects of the weather on an energy harvesting prototype	Experimental
6	Simplified testing of fluid flow in isolated asphalt pores	Computational

different ways, however, this is usually done by circulating a fluid under the hot or warm wearing course (see, e.g., Loomans et al. (2003)). This is because, according to basic heat transfer principles, heat moves from hotter areas to colder ones, thus, if the aim is to remove energy from the pavement and use it somewhere else a moving fluid colder than the asphalt surface is necessary.

The presence of a fluid flowing under or through the pavement during hot or warm periods allows the design of systems that can reduce the surface temperature. These systems involve the installation of pipes or, more generally, channels, in the aggregate layer under the asphalt wearing course and through which the above-mentioned fluid can flow.

1.3 Aims and objectives of the thesis

In this Thesis, the rather new field of convection-powered energy harvesting is investigated by the means of a path-finder approach. This choice was made because little knowledge was available on this topic before the research presented here was conducted. Thus, it was decided to focus on a range of features of

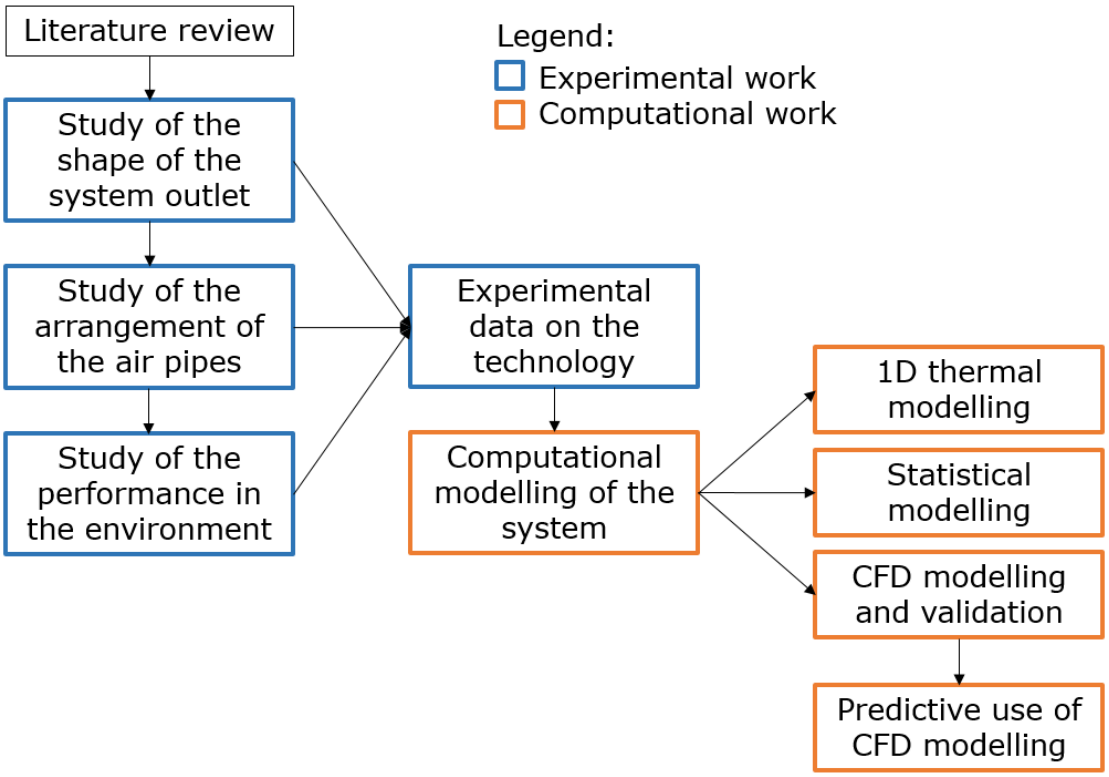

Figure 1.1: Flowchart of the chosen research approach.

the technology (see Figure 1.1) rather than on a specific one, with the aim of providing a wide enough body of knowledge that could enable effective future research in the field.

The choice of using air as the operating fluid is at the core of this Thesis. In fact, using air as opposed to more common fluids (e.g., water) is expected to yield advantages, such as the exploitation of natural ventilation in the place of pumps or other electrical devices. It is, however, recognised that air has worse thermal properties than water. Therefore, this study also aims to show the amount of thermal energy that air can harvest when it flows through a suitably designed pavement.

Based on the above-mentioned ideas, this work is designed to address the following research questions:

- How can channels allowing air flow under an asphalt wearing course be arranged and configured to harvest heat from a pavement during hot or

warm periods?

- Can these channels be exploited for other purposes during cold periods?
- Are artificial channels required, or can asphalt pores be used in their place?

These aims were met by defining a number of objectives, which are listed in Table 1.1 along with the approach chosen to study each topic. The research performed led to the preparation and publication of three articles, which are cited within the text and reported in Appendix B for convenience.

It appears clear that the main focus of this Thesis is on the energy performance of the technology and on the effects that design changes have on it. Before a real life implementation, the energy harvesting approach presented here should undergo further investigations, e.g., on the structural resistance, sustainability, and recyclability of the materials used. The study of the technology from these perspectives may or may not prove the approach unfeasible, as the pavement could possibly be found too weak to be realistically used in a road or too unsustainable to be considered for implementation. The discussion of the structural resistance and the sustainability of the energy harvesting pavement, however, are out of the scope of this Thesis. Therefore, it is suggested that these topics are considered for future work, when the convection-powered energy harvesting technique will possibly be closer to a real-life implementation and a more structured approach to design will be available.

CHAPTER 2

Energy harvesting pavements

2.1 Energy harvesting powered by air convection

As mentioned in Section 1.2, the thermal energy accumulated in an asphalt pavement can be harvested by circulating a fluid under the wearing course. The assembly composed of the wearing course, the aggregate layer, and channels where an operating fluid can flow is what is called an energy harvesting pavement.

Energy harvesting pavements can be built following the structure shown in Fig. 2.1, however, the channels may also be in the form of a serpentine.

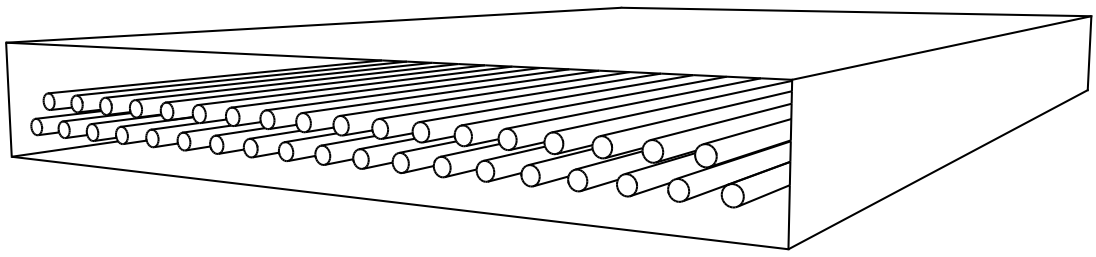

Figure 2.1: Generic structure for energy harvesting pavements.

Since the efficiency of an energy harvesting pavement depends on how effectively heat is exchanged within the system in the first place, it is clear how the choice of an appropriate operating fluid is a very important issue. As reported by Bobes-Jesus et al. (2013), the fluid needs to be compatible with the

Table 2.1: Comparison between water and air.

Property	Unit	Water	Air
Thermal conductivity	$W/(m \cdot K)$	0.58	0.0257
Specific heat capacity	$kJ/(kg \cdot K)$	4.181	1.005
Melting point	°C	0	-215
Density	kg/m^3	999.103 (15°C)	1.225 (15°C)

materials used in the system, provide a good heat transfer performance, and as inexpensive as possible. Moreover, the operating fluid is required to have a high specific heat, in order to allow an effective collection of the energy stored in the pavement.

The practically simplest option is the use of water, but the designer has to take into account the fact that if the temperature reaches 0°C the fluid will turn into ice. For this reason, water is generally used with anti-freezing additives, such as glycols. Moreover, in the case of a leakage, water can damage the pavement structure, thus, reducing its durability. Water is, however, the most commonly used fluid for energy harvesting purposes and there is a number of studies on the topic from both an experimental and a numerical point of view (see, e.g., Guldentops et al. (2016), where both approaches are used).

The use of air in the place of water was first considered by García & Partl (2014). Of course, air and water have very different thermal properties, thus, the amount of energy they can harvest is clearly different, as one could easily imagine by looking at the values shown in Table 2.1. As reported by García & Partl (2014), one of the most important advantages of the use of air as the operating fluid is that it can flow naturally through convection, thus, not needing electricity-powered devices such as pumps or fans. Such air flow is caused by air density differences between the inlet and outlet of the system and can also be called a buoyancy-driven flow. This means that air may not always be a

suitable replacement for other operating fluids when no electrical devices are used, as an appropriate density difference must exist for a buoyant flow to be measured.

Moreover, air is a rather safe operating fluid, because it cannot induce mechanical damages in the pavement in the case of a leakage. In the next chapters, some of the features of the design of energy harvesting pavements powered by air convection are described and discussed.

2.2 Possible uses of the harvested thermal energy

In this Thesis, the focus is on the design of convection-powered energy harvesting pavements rather than on the use of the harvested energy, however, it is important to provide some insight on the possible applications. This is because with no perspective for the use of the harvested energy the technology would not be useful and, consequently, there would be no interest in its implementation.

2.2.1 Reduction of the UHI effect

The Urban Heat Island (UHI) effect is described by Gago et al. (2013) as the accumulation of heat in urban environments as a result of human activities and solar irradiation. The accumulated heat is slowly discharged during the night and, throughout the day, it modifies the thermal environment that would exist in an undisturbed condition, e.g., in the countryside. As a matter of fact, Gago et al. (2013) state that the UHI effect has two consequences:

- the urban cooling load is 25% higher than in the rural environment;
- the urban heating load is 22% lower than in the rural environment.

The increased use of air conditioners to cool down buildings during summer

as a consequence of the UHI effect involves a massive consumption of electrical energy, therefore, it raises obvious environmental concerns. One of the solutions to the UHI effect portrayed in Gago et al. (2013) is the use of suitably designed pavements. Gago et al. (2013) acknowledge that the use of proper materials for pavements, e.g., light-coloured surface coatings, is extremely important to reduce their temperature.

As an alternative, Mallick et al. (2009*b*) report that a possible way to achieve heat removal from pavements is the use of channels buried under the wearing course of pavements and similar to those described in Section 2.1. The amount of energy that is removed from a pavement is what influences the reduction of the UHI effect, thus, it is very important to try and evaluate this parameter. In the context of this Thesis, this aspect is analysed for energy harvesting pavements using air as the operating fluid. Note that, when the heat collected by energy harvesting pavements is used to replace other energy sources, the reduction of the UHI effect is always achieved, whether it is a goal of the designer or not.

2.2.2 HVAC systems

As reported by Loomans et al. (2003), it is possible to use the thermal energy harvested from pavements for HVAC (Heating, Ventilation and Air Conditioning) purposes. The design of this kind of system with the use of energy harvesting pavements (or, in other terms, asphalt solar collectors) is complicated, as it involves a deep knowledge of building physics.

According to Loomans et al. (2003), energy harvesting pavements can be used to heat up buildings when coupled with an aquifer, which works as a heat accumulator. The aquifer enables the system to work for a large part of the day, even when there is a difference in timing between supply and demand.

The system presented by Loomans et al. (2003) is clearly an interesting concept, but it relies on the presence of a thermal storage facility of some kind, because aquifers are often not available around buildings. For this reason, and for the complexity of the design procedure, few commercial applications of this technology are available, such as Road Energy System (RES), which was developed by Ooms Avenhorn Holding, Tipspit, and WTH Vloerverwarming.

In the field of convection-powered energy harvesting, the heat collected from pavements by an air flow could be used in a similar way and accumulated in a thermal storage to allow its use when needed. Since a buoyant flow is based on somewhat small pressure differentials, however, the system would require a more careful design aimed at minimising head losses. This aspect is not studied in this Thesis, because convection-powered energy harvesting is currently not advanced enough to be considered for practical applications.

2.3 Heat transfer in energy harvesting pavements

In this section, a brief introduction to heat transfer mechanisms is provided. This is necessary to understand all the phenomena that are relevant in the field of energy harvesting pavements, since all the main means of heat transfer have to be considered for the design of this technology.

As suggested by García & Partl (2014), an energy harvesting pavement may be ideally separated in two parts:

- control volume above the street level: in this layer, the solar radiation and the heat generated by natural and human sources flow to and from the pavement. The heat is exchanged in the forms of solar radiation, thermal radiation, and convection.
- control volume below the street level: in this layer, the heat absorbed

by the pavement flows as a conductive flux until it reaches the internal surface of the buried pipes, then it is transferred to the operating fluid by the means of thermal convection.

These heat transfer mechanisms are shown in Fig. 2.2, which represents an elementary physical model of the system under investigation. The expected temperature profiles in the control volume below the street level are shown in Fig. 2.3. The slope of the lines in Fig. 2.3 is not representative of the real thermal conductivities of the materials, as these may vary based on the mix chosen.

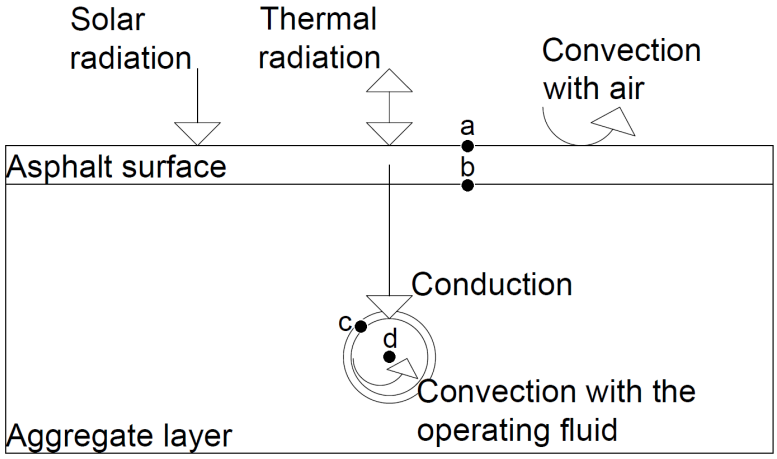

Figure 2.2: Heat transfer mechanisms (letters from Fig. 2.3).

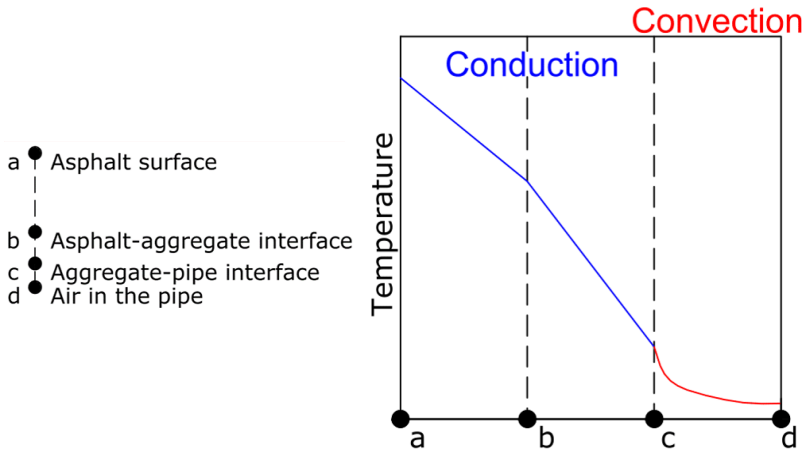

Figure 2.3: Qualitative representation of the expected 1D temperature profile below the street level.

2.3.1 Heat conduction

Heat conduction happens when heat flows through a body because of a temperature difference, following Fourier's Law:

$$\frac{\delta Q}{\delta t} = -k \cdot \oint_S \overrightarrow{\nabla} T \cdot \overrightarrow{dA} \tag{2.3.1}$$

where $\delta Q/\delta t$ is the heat transferred per unit time in J/s (i.e., W), k is the thermal conductivity in W/(m K), T is the temperature in K, and $\overrightarrow{dA}$ is an oriented surface area element in m^2.

In the simple case of a homogeneous 1D material, the formula shown in Eq. 2.3.1 may be integrated, thus, obtaining:

$$\frac{\Delta Q}{\Delta t} = -k \cdot A \cdot \frac{\Delta T}{\Delta x} \tag{2.3.2}$$

where ΔT is the temperature difference between the endpoints chosen for the integration and Δx is the distance between them (horizontal direction if Fig. 2.3). This is the case shown in Fig. 2.3, where Eq. 2.3.2 describes a straight line.

2.3.2 Heat convection

Convection is a heat transfer mechanism that involves a heat exchange between a solid and a fluid in motion.

In the case of energy harvesting pavements, convection is very important, because it involves both the control volumes defined in Section 2.3. Convection allows both the heat transfer between the environmental air and the surface of the pavement and the heat transfer between the internal surface of the pipes and the operating fluid.

There are two types of convective heat transfer, i.e., forced and natural convection, depending on how the fluid motion is originated. An example

of natural convection is the heat transfer between air and the pavement when there is no wind (buoyancy-driven flow). On the contrary, heat transfer is in the form of forced convection when a fluid is forced to flow by an external source.

Moreover, the characteristics of the fluid flow strongly influence how heat is exchanged, therefore, it is important to verify whether the motion is laminar or turbulent. To be specific, the motion has to be turbulent in order to achieve the best convective heat transfer conditions. In the case of energy harvesting pavements, it is possible to control the features of the fluid flow by choosing the proper diameter and flow rate for the pipes, as reported by Bobes-Jesus et al. (2013).

An equation can be used for the calculation of the convective heat flux between a fluid and a surface at a given temperature:

$$q = h \cdot A \cdot (T_s - T_f) \tag{2.3.3}$$

where q is the thermal flux exchanged through convection in W, h is the heat transfer coefficient in W/(m^2 K), A is the surface area between the solid and the fluid in m^2, T_s is the surface temperature in K, and T_f is the temperature of the fluid in K. The calculation of the heat transfer coefficient is not trivial, because it depends on the Nusselt number, Nu, and on the fluid flow regime:

$$h = Nu \cdot \frac{k}{L} \tag{2.3.4}$$

where k is the thermal conductivity in W/(m K) and L is the characteristic length in m. In order to find some correlations to calculate the Nusselt number, please see Table 2.3.

2.3.3 Heat radiation

Thermal radiation is defined as a form of electromagnetic wave that is emitted by any body at a temperature higher than absolute zero (-273.15°C). The most

characteristic feature of this means of heat transfer is that it does not require any material medium to work. Thermal radiation may be absorbed, reflected, or transmitted, depending on the material it reaches. For every material three parameters are defined, i.e., absorptivity (α), reflectivity (ρ), and transmissivity (τ), and the following Eq. 2.3.5 has to be respected at any time:

$$\alpha + \rho + \tau = 1 \tag{2.3.5}$$

In the field of thermal radiation, scientists often refer to a theoretical concept called black body, which is interesting because it provides useful simplifications that help better understand how radiation works. According to Massoud (2008), a black body has three main features:

- it is a perfect emitter: at given temperature and wavelength no other body can emit more radiation than the black body;
- it is a perfect absorber: all incident energy is absorbed by the black body;
- it is a diffuse emitter: the energy emitted by the black body does not depend on the direction, but only on the temperature and the wavelength.

All real bodies are described as imperfect forms of the black body, and may show a range of different behaviours that depend on the values of α, ρ, and τ. One or more of these parameters may be zero for some materials. Asphalt is regarded as an opaque body ($\tau = 0$, see Bobes-Jesus et al. (2013)), therefore:

$$\alpha + \rho = 1 \tag{2.3.6}$$

A pavement can emit a fraction of the energy it would emit if it was a black body and the radiation will be strongly linked to the direction of the hypothetical receiver. Moreover, the incident energy is not completely absorbed, therefore heating a pavement by thermal radiation is not as efficient as heating an ideal black body.

Solar radiation

The sun emits radiation continuously, but only part of it reaches the Earth's surface, since some energy is absorbed by the atmosphere. The fraction of solar radiation reaching the Earth's surface is called incident radiation (q_i''), and it interacts with all the physical bodies it reaches. Since a pavement is not a black body, only part of the incident radiation, q_a'', is absorbed:

$$q_a'' = \alpha \cdot q_i'' \tag{2.3.7}$$

where the radiation is in W/m^2. It is important to keep in mind that pavements receive reflected radiation from many other sources, such as the surrounding buildings or vehicles. The additional amount of heat absorbed by the pavement from these sources may be calculated in the same way shown in Eq. 2.3.7, replacing q_i'' with the heat emitted by all the objects in the control volume under analysis.

Knowledge about the solar radiation is essential in the field of energy harvesting pavements, as this parameter describes the incoming energy on the asphalt surface. As a result, the solar radiation is a common input parameter when modelling energy harvesting systems. There exist equations to forecast the radiation on a horizontal surface at every time of the year (see, e.g., Paulescu et al. (2013)), however, in the case of convection-powered energy harvesting pavements, real values should be preferred due to the strict dependence of the buoyant air flow on weather conditions. For instance, the incident radiation can be measured with specific devices, such as pyrheliometers (direct solar irradiance) and pyranometers (global or diffuse solar irradiance). As an alternative, the solar radiation on the ground can be found in databases such as PVGIS[1] or the NASA Surface Meteorology and Solar Energy (SMSE[2]). Many other al-

[1] See http://re.jrc.ec.europa.eu/pvgis/

[2] See https://eosweb.larc.nasa.gov/sse/

ternative services exist and the selection of the database must be based on the quality of the data available for the location of interest.

Thermal radiation

Thermal radiation is due to the fact that bodies with a temperature above absolute zero emit energy at any time. The emitted energy is usually evaluated through the use of the Stefan-Boltzmann Law:

$$q_e^{''} = \varepsilon \cdot \sigma \cdot T_s^4 \tag{2.3.8}$$

where ε is the emissivity of the material, σ is the Stefan-Boltzmann constant, $5.67 \cdot 10^{-8}$ W/(m^2 K^4), and T_s is the surface temperature of the emitter in K. The emissivity is defined as the ratio between the energy emitted by a chosen material at a given temperature over the energy emitted by a black body at the same temperature.

According to Bobes-Jesus et al. (2013), a pavement can also absorb long-wave radiation coming from the atmosphere. There is more than one way to calculate this amount of absorbed long-wave thermal energy ($q_{long-wave}^{''}$), because it depends on the temperature of the sky:

$$q_{long-wave}^{''} = \alpha_a \cdot \sigma \cdot T_{sky}^4 \tag{2.3.9}$$

where α_a is the material absorptivity to long-wave radiation, and T_{sky} is the effective sky temperature. As there is no broadly accepted way for the computation of T_{sky}, a few options are listed:

$$T_{sky} = T_{air} \tag{2.3.10a}$$

$$T_{sky} = T_{air,\, dry\ bulb} - 6\ K \tag{2.3.10b}$$

$$T_{sky} = T_{air} \cdot \left(0.8 + \frac{T_{dp}}{250}\right)^{0.25} \tag{2.3.10c}$$

where T_{dp} is the dew point temperature, i.e., the temperature at which the evaporation of water vapour in the air is in equilibrium with the condensation of the water vapour itself, provided that the pressure is constant.. Eq. 2.3.10c is called the Bliss equation, and, according to Hall et al. (2012), it is the best option to match the experimental results.

In some cases, it may be interesting to know the net flux generated by the long-wave radiation. According to Bobes-Jesus et al. (2013), its calculation can be performed with the assumption that the absorptivity to long-wave radiation is equal to the emissivity, i.e.,

$$q''_{net,\, long-wave} = \varepsilon \cdot \sigma \cdot (T_s^4 - T_{sky}^4) \tag{2.3.11}$$

where T_s is the temperature of the surface receiving the heat flow. The calculation of the contributions due to long-wave radiation, however, often cannot be pursued, as it depends on weather-related variables that are not always available.

2.3.4 Heat transfer phenomena due to rainfall

Even if most studies tend to neglect this aspect due to data unavailability, rainfall does influence the performance and behaviour of pavements, as reported by Yavuzturk et al. (2005). Therefore, it is important to provide at least a general description of the physical phenomena involved.

Heat transfer processes involving rain include both sensible and latent heat. The simplest way to tackle this problem is to perform a mass/energy balance on the surface of the pavement, i.e.,

$$q''_{rain,\, sensible} = \dot{m}''_{rain} \cdot c_p \cdot (T_{air} - T_{surface}) \tag{2.3.12a}$$

$$q''_{rain,\, latent} = h_{fg} \cdot \dot{m}''_{evaporation} \tag{2.3.12b}$$

where q'' is the heat exchanged per unit area in W/m^2, $\dot{m}''$ is the mass flow per unit area in kg/(s m^2), c_p is the specific heat capacity in J/(kg K), and h_{fg} is the latent heat of vapourisation in J/kg.

In Yavuzturk et al. (2005), latent heat transfer is taken into account only when $T_{surface} > 0.55$°C. Moreover, this model does not consider the accumulation of rain, thus, assuming that rain is drained as soon as it touches the pavement surface. A thin film of water on the pavement surface is considered in order to take evaporation into account.

The mass flow of the evaporating water shown in Eq. 2.3.12b has to be calculated with a proper method. Yavuzturk et al. (2005) chose the j-factor analogy by Chilton and Colburn, therefore,

$$\dot{m}''_{w,\,evaporation} = h_d \cdot (w_{air} - w_{surface}) \tag{2.3.13a}$$

$$h_d = \frac{h}{Le^{2/3} \cdot c_p} \tag{2.3.13b}$$

$$Le = \frac{\alpha}{D_{AB}} \tag{2.3.13c}$$

where h_d is the mass transfer coefficient, w_{air} is the humidity ratio of the ambient air, $w_{surface}$ is the humidity ratio of saturated air on surface of the pavement, h is the convection coefficient for the air-pavement surface defined in Section 2.3.2, α is the thermal diffusivity of the air, and D_{AB} is the binary diffusion coefficient. Both α and D_{AB} need to be evaluated at the pavement-air film temperature.

Similarly to what happens with the calculation of the heat flux due to long-wave radiation, the heat fluxes due to rain phenomena are often not calculated, because the equations listed in this section require the knowledge of parameters that are not commonly measured in a real life installation or in weather data. Therefore, unless an approximated measure of such heat fluxes is needed for a specific purpose, they are hardly considered.

2.4 Thermal properties of asphalt pavements

In the case of this Thesis, the thermal properties of asphalt pavements are relevant because they influence how heat is transmitted to the air flow. In Table 2.2, some typical values of these properties are gathered.

As reported by Bobes-Jesus et al. (2013), variations in the thermal properties of an asphalt pavement cause different effects:

- during warm or hot periods, a higher thermal conductivity causes the surface temperature to decrease and the in-depth temperature to increase. The variation in the thermal conductivity has a stronger influence on the in-depth temperature;
- the specific heat capacity parameter influences the heat storage capacity, thus, its increase leads to a longer time to reach the maximum temperature of the pavement. An increased heat storage capacity makes the temperature variations decrease;
- an increase in the reflectivity causes the temperatures to decrease, as more energy is reflected. Moreover, in winter, this parameter may rise due to snow or ice, because their lighter colour makes the surface reflect a higher amount of radiation;
- if the algebraic difference between emissivity and absorptivity is kept constant there are no or very little changes in the temperature profile of the pavement. If the emissivity increases, the maximum temperatures reached throughout the day decrease. An increase in the absorptivity makes the surface temperature drop. Since with time the colour of the pavement surface gets lighter, a decrease in the absorptivity has to be expected. Dirt causes a drop in the absorptivity of up to 0.1.

It is important to specify that it is possible to add a number of substances to an asphalt mixture to improve its physical properties, therefore, the values out-

Table 2.2: Typical physical properties of asphalt, from Çengel (2008) and Bobes-Jesus et al. (2013).

Property	Range	Unit
Thermal conductivity	$0.74 - 2.89$	$W/(m \cdot K)$
Specific heat capacity	$800 - 1853$	$J/(kg \cdot K)$
Absorptivity (α)	0.9	//
Reflectivity (ρ)	$0.2 - 0.35$	//
Emissivity (ε)	$0.85 - 0.93$	//

lined in Table 2.2 only apply to a generic mixture with no man-made additives. There are many examples of such man-made additives, including, but not limited to, metals (see, e.g., Arabani & Mirabdolazimi (2011) and García et al. (2014)), recycled scraps from old pavements (see, e.g., Sengoz & Oylumluoglu (2013)), rubber (see, e.g., Oliveira et al. (2013)), polymers (see, e.g., Xiao et al. (2014)), or natural substances (see, e.g., Seidel & Haddock (2014)): each one of these materials generates measurable modifications in the properties of the resulting mixture.

In the case of energy harvesting pavements, improvements to the thermal performance could be pursued by an increase in the thermal conductivity, which may be obtained with the following additives:

- graphite (see Wu et al. (2009), Wu et al. (2010), Wu et al. (2011), or Wang et al. (2010));
- quartz (see Mallick et al. (2008), Mallick et al. (2009*a*), Mallick et al. (2009*b*), or Dawson et al. (2012));
- copper (see Mallick et al. (2008) or Dawson et al. (2012));
- steel wool fibres (see García et al. (2014)).

According to Wu et al. (2009) and Mallick et al. (2009*b*), the first two additives in the list provide good results in the enhancement of the thermal properties of the aggregate, while the use of copper powder is discouraged by Mallick et al.

(2008), as there are concerns about its interaction with bitumen. Finally, García et al. (2014) report that the use of steel wool fibres only provides a slight increase in the thermal conductivity of the material.

Furthermore, Mallick et al. (2008) state that it is possible to increase the amount of energy that a pavement absorbs by using paints to decrease the reflectivity or to increase the absorptivity. However, since asphalt behaves approximately like a black body, the emission of long-wave radiation is high even when black surface coatings are used, as reported by Bobes-Jesus et al. (2013).

Nevertheless, in this Thesis, no modifications of the properties of the asphalt pavement prototypes were considered.

Table 2.3: Correlations for the calculation of Nu, adapted from Bobes-Jesus et al. (2013).

Type of flow	Correlation	
Natural convection		
Warm surface upwards or cold surface downwards	$Nu = 0.54 \cdot Gr_L \cdot Ra^{1/4}$	$10^4 \leq Ra \leq 10^7$
	$Nu = 0.15 \cdot Gr_L \cdot Ra^{1/3}$	$10^7 \leq Ra \leq 10^{11}$
Warm surface downwards or cold surface upwards	$Nu = 0.27 \cdot Gr_L \cdot Ra^{1/4}$	$10^5 \leq Ra \leq 10^{10}$
Forced Convection - Theoretical approach		
Laminar flow	$Nu = 0.664 \cdot Re_L^{1/2} \cdot Pr^{1/3}$	
Turbulent flow	$Nu = (0.037 \cdot Re_L^{4/5} - 871) \cdot Pr^{1/3}$	
	if $0.6 < Pr < 60$ and $5 \cdot 10^5 < Re_L < 10^8$	
Forced Convection - Empirical approach		
Asphalt surfaces		
$h_c = 698.24 \cdot [0.00144 \cdot T_m^{0.3} \cdot u_m^{0.7} + 0.00097 \cdot (T_s - T_{air})^{0.3}]$		
Jurges' empirical equation		
$h_c = 5.8 + 4.1 \cdot u_m$		
where $T_s = asphalt\ surface\ temperature$, $T_{air} = air\ temperature$, $T_m = 0.5 \cdot (T_s + T_{air})$		
$u_m = wind\ velocity$. Some restrictions apply to the use of this equation, as reported in Bobes-Jesus et al. (2013).		
Heat exchange between pipes and operating fluid (Dittus-Boelter equation)		
$Nu = 0.023 \cdot Re_D^{4/5} \cdot Pr^n$	$0.7 \leq Pr \leq 160$	
	$Re_D \geq 10000$	
	$L/D \geq 10$	
$n = 0.4$ if the fluid is being heated, $n = 0.3$ if it's being cooled		

CHAPTER 3

A first approach to convection-powered energy harvesting

The research conducted to develop this Thesis started with the construction of an energy harvesting asphalt pavement prototype. The prototype was built to simulate the structure of a real pavement in a low-trafficked area or a car park. Thus, two layers were considered for its construction (see Chiarelli et al. (2015*a*)): the top layer, i.e., a 50 mm thick asphalt wearing course, was built with a dense asphalt mixture (limestone aggregate, maximum size 11 mm), while unbound gravel was placed under it along with 13 straight pipes made of stainless steel (internal diameter of 30 mm). The layers forming this structure are common in car parks, where a thick open-graded stone bed can be used as the sub-base for the asphalt paving for the purpose of managing storm water (see, e.g., Speight (2016)). The decision to embed the pipes in the aggregate layer rather than directly in the asphalt wearing course is inspired by the installation technique used for drain pipes, which are sometimes embedded in a gravel bed (e.g., French drain). In the case of energy harvesting pavements,

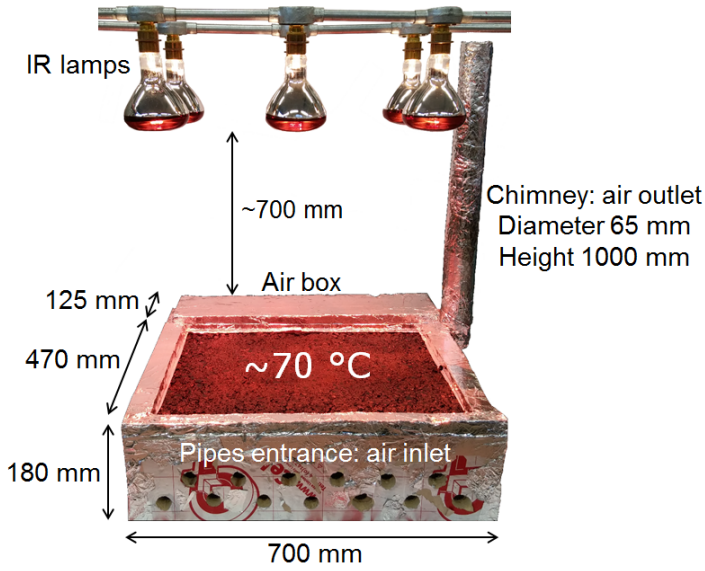

Figure 3.1: Energy harvesting asphalt pavement prototype.

however, the pipes do not serve any draining functions, as they are not meant to allow water penetration. As mentioned in Section 1.3, the study of the mechanical behaviour of this assembly is not discussed in this work due to the very early stage of design. The reason why a prediction on the mechanical behaviour of the system cannot be formulated at this time is that it reportedly depends on a wide range of parameters, such as width of the excavation, bedding height, mechanical properties of the natural soil surrounding the trench, mechanical properties and grade of compaction of the bedding material, pipe material, mechanical and geometric properties of the pipe, and material and geometry of the roadway pavement and its sub-pavement (see Barbato et al. (2010)). Nevertheless, it is expected that specialist tools such as the CANDE software (see Katona (2015)) will be effective for the identification of the possible weak areas in the system and their subsequent optimisation once likely ranges of values for the above-mentioned parameters will be available.

In Fig. 3.1, it can be observed that the steel pipes installed in the gravel layer go from the open end of the system to a closed volume called the air box, from which the air used as the operating fluid is free to exit the system through

a 1000 mm long chimney with an internal diameter of 65 mm. Furthermore, Fig. 3.1 shows a set of six infrared bulbs (250 W each), which were used as a heat source to reach about 70°C on the pavement surface and, thus, simulate the Sun's radiation in a hot location. This specific design was inspired by the prototype shown by García & Partl (2014), where the authors buried 60 metal pipes in a thick asphalt slab. The prototype shown in Fig. 3.1 and that used by García & Partl (2014) are similar in size, but the one used in this Thesis has a different internal structure. In fact, García & Partl (2014) considered pipes embedded directly in an asphalt slab, while, in the research presented here, they are buried in the aggregate layer under the wearing course. In addition, the total internal volume of the pipes considered in the present work is about 3.5 times larger than that used by García & Partl (2014). The larger internal volume allowed for air was chosen to try and compensate for the lower thermal conductivity of unbound aggregate layer compared to that of asphalt (see, e.g., Table 6.1). Furthermore, the larger pipes were chosen based on their ease of installation in the prototype and on the horizontal and vertical spacing (100 mm and 50 mm, respectively) that were fixed. These distances between the pipes were chosen to fill the aggregate layer with a regular pattern, because, at this stage, no guidelines for the construction of the system had been developed. For theoretical principles and experimental results involving different pipe arrangements, see Chapter 4.

The performance of this first prototype was tested based on changes in the chimney height and diameter (see Chiarelli et al. (2015*a*) and Chiarelli et al. (2015*b*)). The tests that were performed involved chimney heights of 250 mm, 500 mm, 1000 mm, 1500 mm, 2000 mm, and 2500 mm, while the (internal) diameters considered were 20 mm, 32 mm, 40 mm, and 65 mm. The performance of

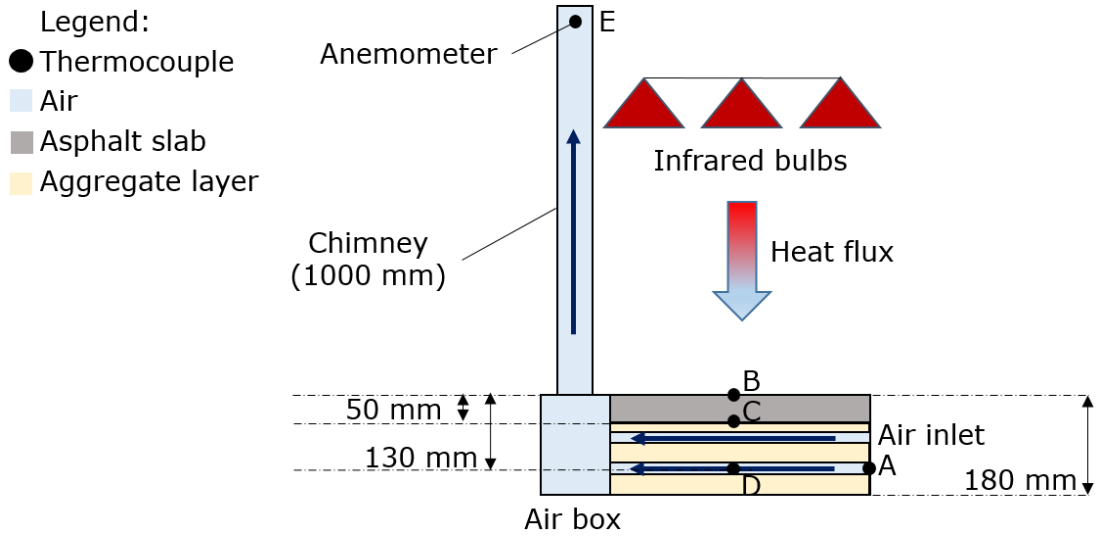

Figure 3.2: Position of the thermocouples in the prototype pavement pictured in Fig. 3.1. Thermocouple D was placed between the pipes in the bottom row.

the prototype was monitored using a OMEGA OMB-DAQ-54 datalogger[1] with OMEGA J-type thermocouples (limits of error: ± 1.1°C)[2] and with a PCE-423 anemometer[3]. The position of the thermocouples used is illustrated in Fig. 3.2. To be specific, thermocouple C was placed at 50 mm from the pavement surface, while thermocouple D was placed at 130 mm from the surface (between the pipes in the bottom row). In addition, the anemometer was placed in position E when needed. The tests performed consisted in a heating phase of 24 h and a cooling phase of 24 h. The measurements considered in the analysis were all taken at the end of the heating phase, i.e., in steady state conditions and with the maximum surface temperature. As an example, the temperature evolution recorded during a whole test (48 h) is shown in Fig. 3.3. It can be observed that the temperatures in the system all increase up to a maximum value during the heating transient, then, when the infrared lamps are powered off, they all go

[1]Manufactured by OMEGA ENGINEERING, United Kingdom, see www.omega.co.uk.
[2]ibid.
[3]Manufactured by PCE Instruments, United Kingdom, see www.pce-instruments.com.

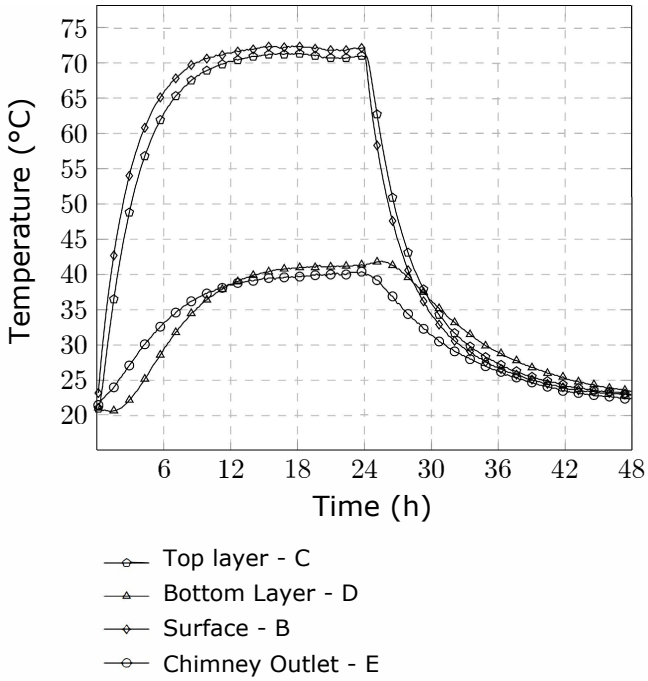

Figure 3.3: Evolution of the temperatures monitored during a whole test (chimney height 1000 mm, chimney diameter 65 mm, letters from Fig. 3.2).

back to their initial value. This is possible only in a laboratory environment, where the heating and cooling times are strictly controlled. Steady state conditions can be seen in Fig. 3.3 as the plateau between, approximately, hour 15 and hour 24.

3.1 Effect of the chimney height and diameter

In Fig. 3.4 and 3.5, the effect of chimney height and diameter on the performance of the system is shown. It is relevant to point out that the curve corresponding to a diameter of 20 mm does not have values for heights of 2.0 m and 2.5 m. The reason for this is that no air speed was measured in these cases, thus, meaning that no air flow due to thermal convection was generated. Furthermore, in Table 3.1, the temperatures measured in steady state conditions

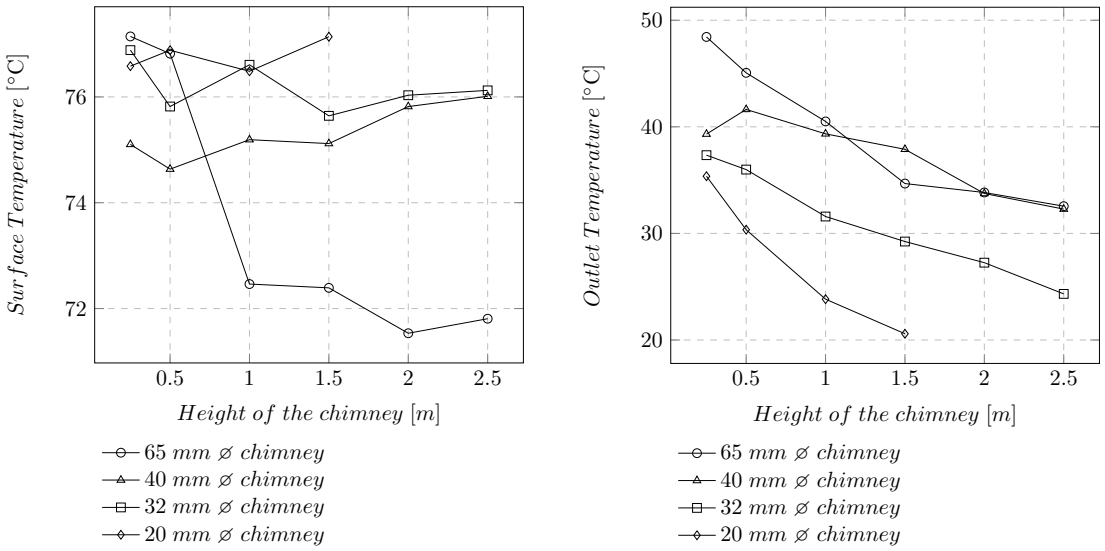

(a) Effects on the surface temperature (Point B in Fig. 3.2).

(b) Effects on the outlet temperature (Point E in Fig. 3.2).

Figure 3.4: Temperatures in the domain with changes in the chimney height and diameter, from Chiarelli et al. (2015*b*).

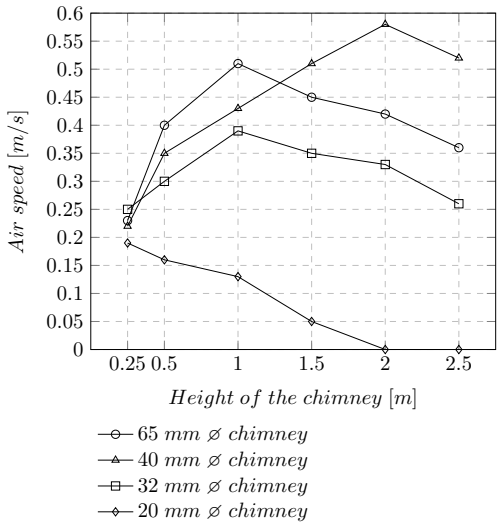

Figure 3.5: Effect of the chimney height and diameter on the outlet air speed, from Chiarelli et al. (2015*b*).

are gathered for all the tests performed. If the temperatures in Fig. 3.4 are considered alone, one may conclude that the behaviour of the system is erratic, as there does not appear to be any significant trend in the results. However, the observation of the data in Table 3.1 suggests that the values measured in

the prototype were coherent, as the temperatures decrease with depth in the prototype. Therefore, since the results in Fig. 3.4 cannot be explained easily, it is necessary to analyse fluid-dynamics in the system in order to gather more insight on the data that was obtained. The most natural way to try and explain what was observed in the experimental trials is the calculation of the Reynolds number, Re, which is meant to find out whether a fluid regime is laminar ($Re < 2040$) or turbulent ($Re > 2040$), as reported by Avila et al. (2011). This is because the flow regime influences how heat is exchanged, as explained in Section 2.3.2. The Reynolds number is dimensionless and can be found as:

$$Re = \rho \cdot v \cdot D_h / \mu \tag{3.1.1}$$

where ρ is the density of air in the chimney in kg/m^3, v is the air speed in m/s, D_h is the internal diameter of the chimney in m, and μ is the dynamic viscosity of air in kg/(m s). The specific reason behind the calculation of the Reynolds number is that the air speed measured and shown in Fig. 3.5 peaks at different heights for different chimney diameters. Therefore, it was expected that explaining the behaviour of the outlet air speed could also clarify the reasons behind the apparently erratic behaviour of the temperatures shown in Fig. 3.4.

As explained by Chiarelli et al. (2015*b*), the density of air in the chimney that needs to be used in Eq. 3.1.1 was calculated based on the ideal gas law under the assumption that, at the outlet, the air pressure is equal to the atmospheric pressure (p_{atm}):

$$Re = p_{atm} / (R T_E) \cdot v \cdot D_h / \mu \tag{3.1.2}$$

where R is the gas constant for air, i.e. 287.058 J/(kg K). This is not entirely accurate, because the air flow is powered by buoyancy, thus, by density differences. However, the difference is so small that the approximation was deemed

Table 3.1: Temperatures in the pavement prototype measured in the tests performed (adapted from Chiarelli et al. (2015*b*), column headers refer to Fig. 3.2).

Height (m)	B (°C)	C (°C)	D (°C)	E (°C)
Chimney ⌀65 mm				
0.25	77.1	76.0	47.9	48.4
0.5	76.8	75.7	45.9	45.1
1	72.4	71.4	41.9	40.5
1.5	72.4	69.9	38.4	34.7
2	71.5	68.6	37.9	33.8
2.5	71.8	68.8	37.6	32.6
Chimney ⌀40 mm				
0.25	75.1	73.7	44.7	39.3
0.5	74.6	73.3	45.9	41.6
1	75.2	73.8	45.1	39.3
1.5	75.1	73.8	44.9	37.9
2	75.8	74.4	45.3	33.7
2.5	76.0	74.7	45.5	32.3
Chimney ⌀32 mm				
0.25	76.9	76.5	50.6	23.6
0.5	75.8	75.1	49.2	24.2
1	76.6	75.9	48.6	23.5
1.5	75.6	74.5	46.8	23.4
2	76.0	75.0	47.0	27.8
2.5	76.1	75.1	48.9	27.1
Chimney ⌀20 mm				
0.25	76.6	76.1	51.4	35.4
0.5	76.9	76.5	51.4	30.4
1	76.5	76.2	51.2	23.8
1.5	77.1	76.6	51.7	20.6
2	n/a	n/a	n/a	n/a
2.5	n/a	n/a	n/a	n/a

Table 3.2: Reynolds number, Re, for the tests performed, adapted from Chiarelli et al. (2015*b*).

Chimney Height (m)	Chimney diameter			
	65 mm	40 mm	32 mm	20 mm
0.25	831	836	1006	739
0.50	1472	1313	1209	641
1.00	1926	1635	1593	541
1.50	1757	1955	1439	212
2.00	1648	2277	1344	n/a
2.50	1423	2059	1069	n/a

acceptable. Furthermore, the viscosity was calculated with Sutherland's equation:

$$\mu = \mu_{ref} \cdot \left(\frac{T}{T_{ref}} \right)^{3/2} \cdot \frac{T_{ref} + S}{T + S} \tag{3.1.3}$$

where μ_{ref} is the reference dynamic viscosity for air, 1.716E-5 kg/(m s), T is the temperature of air in the chimney in K, T_{ref} is equal to 273.15 K, and S is Sutherland's constant, which, in the case of air, is equal to 110.4 K.

Thanks to Eq. 3.1.1 and Eq. 3.1.3 it was possible to calculate the values of Re for all the cases considered (see Table 3.2).

The values in Table 3.2 show that the turbulence threshold was exceeded only in two cases, and Re was maximum for the case of a 2000 mm long chimney with a diameter of 40 mm, which is also the case with the highest air speed. The highest speed did not come with the highest surface temperature reduction (see Fig. 3.4), which, instead, corresponds to the case with a 2000 mm long chimney with a diameter of 65 mm. This observation hints at the complex interaction between the phenomena that rule the energy harvesting process, since temperatures and air speed are related in a non-trivial way. It appears clear that a simple observation of the experimental data is not sufficient to fully understand the results that were obtained. The reason for this will become

evident in Section 6.2.1 and is partially related to the presence of the air box, where air vortices cause an interruption of the air mass flow due to the change in its direction, from parallel to perpendicular to the ground.

Some further observations, however, can be made based on the data shown in Fig. 3.5. As reported by Chiarelli et al. (2015*b*), fluid dynamics teaches us that smaller chimney diameters usually cause higher head losses due to friction. Therefore, the air speed with a narrower chimney is supposed to be lower. This can be observed for chimney heights of 500 mm and 1000 mm, where the data points corresponding to the different diameters in Fig. 3.5 are sorted in ascending order. However, if the chimney height is increased, the air speed for the 65 mm chimney decreases and the order between the data points is disrupted. The reason for this is that the prototype used was small-sized and, consequently, the heat harvested from the pavement was not always enough to generate a reasonably high pressure difference between inlet and outlet (which is related to the density of air at the chimney outlet) when the volume of air in the system increased. In fact, with a higher diameter the volume of air is higher and requires more energy to circulate by the means of buoyancy, because the working mechanism of the prototype is density-driven.

Furthermore, it is relevant to point out that the curve corresponding to a diameter of 20 mm in Fig. 3.5 seems not to peak, unlike all the others. This happened because of the increase in the head losses with the decrease in the chimney diameter, which was discussed above. The case of the 20 mm chimney is particularly interesting, because it shows the above-mentioned phenomenon in a quite striking way, since the air speed becomes negligible with chimney heights above 1500 mm. This is further proven by the observation of Fig. 3.4b, where, in the case of a 20 mm diameter and a length of 1500 mm, the chimney temperature is very close to the ambient temperature, which in turn means that

there is almost no difference in the air density and that a buoyancy-powered flow cannot be measured.

As mentioned in Section 1.1, energy harvesting processes can be used to produce electricity. In this case, it can be seen that no configuration achieved an outlet air speed above 0.60 m/s. However, the threshold to convert the buoyant mass flow into electricity with a small wind turbine is at least 2 m/s for standard air powered systems, as reported by Singh & Ahmed (2013). Therefore, at the current stage of development, the prototype described in this chapter does not appear to be able to reach the cut-in speed of a turbine (about 2 m/s) and, consequently, to generate electricity. It is, however, likely that, in this case, the limiting factor is the very small size of the prototype pavement surface compared to the volume of air in the system. In fact, a higher surface area may lead to a higher outlet air flow and a higher air speed, as reported by Chiarelli et al. (2015*b*). Further considerations on this aspect are available in Section 6.2.2.

3.2 Thermal efficiency of the energy harvesting process

Since the energy harvested by the prototype cannot be converted into electricity at this time, it is worth trying to quantify at least the thermal efficiency of the energy harvesting process. A possible approach is the use of an energy-based definition of efficiency, as reported by Chiarelli et al. (2015*a*) and Chiarelli et al. (2015*b*):

$$\eta = \frac{\dot{m} \cdot c_{p,c} \cdot (T_E - T_e)}{q_{max}} \tag{3.2.1}$$

where $\dot{m}$ is the mass flow of air at the chimney outlet, $c_{p,c}$ is the specific heat capacity, T_E is the temperature of air at the chimney outlet, T_e is the temperature of the environment, and q_{max} is the maximum heat flux available for harvesting.

As seen in García & Partl (2014), the value of q_{max} can be calculated as follows:

$$q_{max} = q_a - q_{wa} - q_{ca} \tag{3.2.2}$$

where q_a is the total heat flux available in the pavement, q_{wa} is the heat lost by radiation, and q_{ca} is the heat exchanged by convection with the ambient air by the pavement surface. The values of q_{wa} and q_{ca} can be found as:

$$\begin{cases} q_{wa} = \sigma \cdot A_a \cdot \varepsilon_a \cdot (T_e^4 - T_B^4) \\ q_{ca} = h_a \cdot A_a \cdot (T_e - T_B) \end{cases} \tag{3.2.3}$$

where σ is the Stefan-Boltzmann constant ($5.67 \cdot 10^{-}8$ W/(m^2 K^4)), ε_a is the emissivity of the pavement surface, T_e is the temperature of the environment, T_B is the temperature of the pavement surface, and h_a is the mean convective heat transfer coefficient for the pavement-air interface.

The value of h_a can be calculated with a variety of approaches, as seen in Table 2.3 (see Jurges' empirical equation) or as reported by Li et al. (2013). Generally speaking, however, such a parameter is a function of the speed of the wind flowing over the asphalt surface, which, in a laboratory environment, is extremely low. As a result, the air speed above the pavement surface can be considered as a constant, as in the laboratory it does not influence the results in a significant way.

Furthermore, it is relevant to point out that the air speed at the chimney outlet influences the value of the efficiency shown in Eq. 3.2.1, as the mass flow $\dot{m}$ is calculated as:

$$\dot{m} = \rho \cdot v_E \cdot A \tag{3.2.4}$$

where ρ is the density of air at the chimney outlet, v_E is the air speed, and A is the chimney cross section.

Based on Eq. 3.2.1, the thermal efficiency of the prototype was calculated.

The values obtained range between about 1% and 15% and the maximum thermal efficiency was achieved with a 500 mm long chimney with an internal diameter of 65 mm.

The way efficiency is quantified in Eq. 3.2.1 is focused on an energy balance, however, other points of view may be considered. As reported by Chiarelli et al. (2015*b*), it is possible to focus on the reduction of the UHI effect and, therefore, write a new definition of the efficiency based on the temperature reduction potential of the pavement prototype:

$$\eta_{UHI} = \frac{T_{B,NH} - T_B}{T_{B,NH}} \tag{3.2.5}$$

where $T_{B,NH}$ is the pavement surface temperature with no energy harvesting and T_B is the pavement surface temperature found in the experimental trials. The exact same equation can be used with the temperature at the bottom of the prototype pavement, using $T_{D,NH}$ and T_D in the place of $T_{B,NH}$ and T_B. The temperatures called T_{NH} represent the temperature at the point under consideration when no energy harvesting was present and were found by obstructing all the energy harvesting pipes in the prototype.

The values of $T_{B,NH}$ and $T_{D,NH}$ are 78.81°C and 65.16°C respectively, as reported in Chiarelli et al. (2015*b*). It is important to point out that these temperatures might differ from values gathered in the field, because the thermal insulation covering the prototype pavement causes heat accumulation and prevents heat from moving to underlying layers. The results obtained using Eq. 3.2.5 are shown in Fig. 3.6 for both T_B and T_D. It can be observed that the experimental setup with the best temperature reduction efficiency for both layers is the one with a 65 mm internal diameter when a chimney height above 1000 mm is considered. This result is consistent with what is shown in Fig. 3.5, where the chimney with an internal diameter of 65 mm has rather high values of outlet air speed when compared to most of the other configurations.

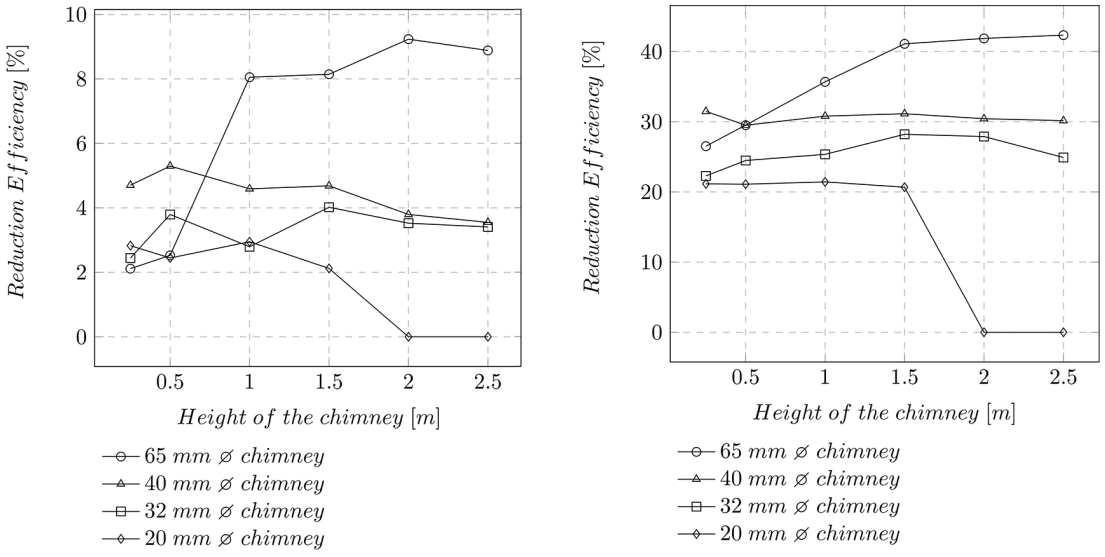

(a) Surface temperature, T_B.

(b) Bottom temperature, T_D.

Figure 3.6: Temperature reduction efficiency based on Eq. 3.2.5, adapted from Chiarelli et al. (2015*b*).

The reason why the configuration with the maximum thermal efficiency (500 mm height, 65 mm internal diameter) is not the one with the the best temperature reduction potential is related to the way efficiency is defined. In fact, the thermal efficiency relies on the maximum outlet temperature, while the temperature reduction potential is based on the minimum temperature (surface or bottom) obtained in the experiments.

Furthermore, even if the configuration with a 40 mm diameter yielded the highest air speed, it did not yield the maximum temperature reduction potential nor the maximum thermal efficiency. The reason why this result does not violate the findings of Bobes-Jesus et al. (2013) is that the speed throughout the prototype pavement is not constant due to its shape. As shown in Section 6.2.1, the change in the direction of the flow in the air box (from the horizontal pipes to the vertical chimney) creates eddies that affect the velocity in the system. Consequently, measuring a high outlet speed does not always imply that the speed in the pipes beneath the pavement surface will be high. In fact, based

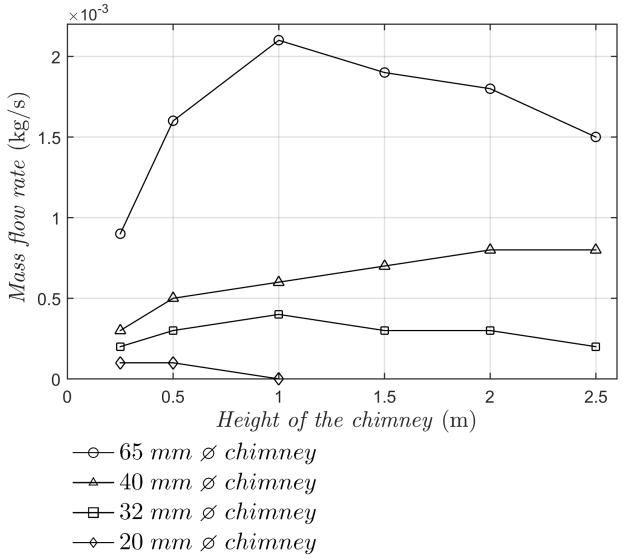

Figure 3.7: Mass flow calculated with Eq. 3.2.4.

on the observation of the experimental results, it can be hypothesised that the highest speed in the energy harvesting pipes corresponded to the configuration with a 65 mm internal diameter, as it showed a high efficiency in the majority of the cases under consideration.

Moreover, based on Eq. 3.2.4, the mass flow through the outlet of the prototype can be represented as a function of the chimney height for all the diameters considered (see Fig. 3.7). The observation of Fig. 3.7 provides further insight on the results seen so far, because, for chimney heights above 1000 mm, the curves in Fig. 3.7 are in the same order as those shown in Fig. 3.6 and in the opposite order as those represented in Fig. 3.4a. This suggests that higher mass flows through the chimney cause lower surface temperatures and, as a result, yield a higher efficiency. Therefore, it can be hypothesised that the mass flow at the system outlet is an important parameter for the design of energy harvesting pavements, as higher values of mass flow appear to allow a more effective extraction of heat. Note that these observations on the mass flow highlight the fact that fluid flow should be considered alongside thermodynamics when analysing the experimental results obtained with the energy harvesting proto-

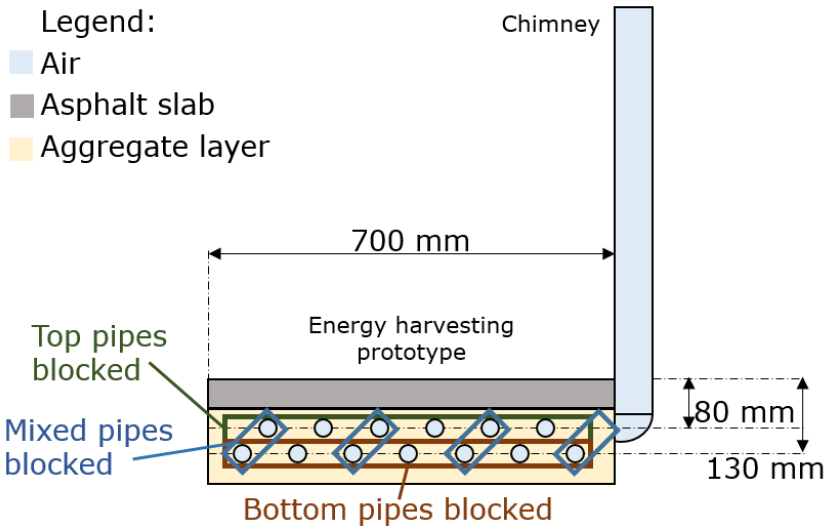

Figure 3.8: Scheme of the modifications to the pipes in the energy harvesting prototype described in Table 3.3.

type.

Finally, it is important to point out that the difference in efficiency results for different chimney heights with the same internal diameter are related to different air density differences between the air box and the chimney outlet, which are in turn caused by different outlet pressures and temperatures.

3.3 Additional tests on the prototype

The prototype shown in Fig. 3.1 cannot be easily modified. However, as reported in Chiarelli et al. (2015*b*), it was decided to perform further tests to investigate the sensitivity of the system to some modifications (see Fig. 3.8). The changes tested are shown in Table 3.3 and they were all made with a 1000 mm high chimney with a 65 mm internal diameter (standard setup in Table 3.3) due to its better performance for the reduction of the pavement temperatures (see Section 3.2). The first observation that can be made is that obstructing a whole row of pipes, no matter if the bottom or the top one, causes a very similar effect on all the parameters considered. The difference between the two rows,

Table 3.3: Modified experimental setups for qualitative analysis, adapted from Chiarelli et al. (2015*b*).

Experimental setup	T_B (°C)	T_C (°C)	T_D (°C)	T_E (°C)	Air speed (m/s)
Top pipes blocked	74.70	74.58	44.26	37.25	0.34
Bottom pipes blocked	71.47	69.93	46.01	39.13	0.36
Mixed pipes blocked	72.63	72.16	45.71	36.87	0.36
50% air box volume	71.35	69.84	39.65	38.40	0.36
Standard setup	72.46	71.39	41.90	40.50	0.51

however, is that if the top layer is blocked a higher surface temperature (T_B) is found. This means that the highest contribution to the surface temperature reduction comes from the top row of pipes, which is reasonable considering that it is closer to the wearing course where the thermal energy enters the pavement.

Furthermore, from the observation of Table 3.3 it appears clear that the performances of the modified setups are similar to that of the standard one, however, they always have much smaller outlet air speeds. This result is likely to be related to the lower amount of air inside the system in all the modified configurations, which reduces the amount of energy that can be harvested. This observation can be confirmed by the observation of the values of T_E, which reached its maximum value in the standard configuration.

CHAPTER 4

Construction hypotheses for energy harvesting pavements

The knowledge available in the literature on convection-powered energy harvesting pavements is rather poor, as the topic has not been extensively studied in the past. However, some information on the design of water-based energy harvesting systems is available and, therefore, should be considered.

The main sources of information for water-based systems are Loomans et al. (2003), Mallick et al. (2008), Mallick et al. (2009*a*), Mallick et al. (2009*b*), Wu et al. (2009), Wang et al. (2010), Wu et al. (2011), and Bobes-Jesus et al. (2013), while García & Partl (2014) performed a study on convection-powered energy harvesting. The parameters that were studied in the literature are:

- the diameter of the pipes;
- the distance between the pipes;
- the depth of the pipes;
- the material of the pipes (e.g., copper, PEXAL, ONIX, PEX, or steel);
- the pipe arrangement (straight pipes or serpentine);
- the type of aggregates (standard or high conductivity).

The diameter of the pipes was analysed by Wang et al. (2010) with computa-

tional simulations. The results obtained suggest that a larger diameter (with constant distance between the pipes) implies a lower surface temperature and that, consequently, the heat is transmitted more effectively to the operating fluid (i.e., water). However, Wang et al. (2010) also state that the use of very large diameters can cause structural issues. Moreover, a high diameter may not be acceptable for generating a buoyancy-driven mass flow, as the temperature profile inside the pipes could be too inhomogeneous.

A larger amount of data is available on the distance between the pipes, as all authors usually choose a personalised value for this parameter. The comparison of the performance of a given, fixed system (i.e., a chosen mixture with a chosen aggregate layer) while varying the pipe spacing, however, is not usually evaluated. Wang et al. (2010), show how having a higher density of pipes (i.e., a lower pipe spacing) increases the heat gathering ability of the pavement. This aspect is important, but a designer also has to consider the fact that a very high density of pipes in the ground may generate thermal interactions between them, thus, reducing the global efficiency, as reported by Bobes-Jesus et al. (2013). According to Bobes-Jesus et al. (2013), economic aspects should also be taken into account when choosing the pipe spacing.

For what concerns the depth of the pipes, some considerations are found in Loomans et al. (2003), where the authors show that the performance of the system increases if the pipes are closer to the pavement surface. Bobes-Jesus et al. (2013) report that, due to heat transfer phenomena, the maximum temperature of asphalt is at 20 mm from the surface, thus, that may be regarded as an optimal depth to bury the pipes. If the pipes are buried further from the pavement surface, the energy that the collector is able to harvest decreases, even if the temperature profile becomes more stable. This, however, may not be possible, as it strictly depends on the thickness of the asphalt layer and on

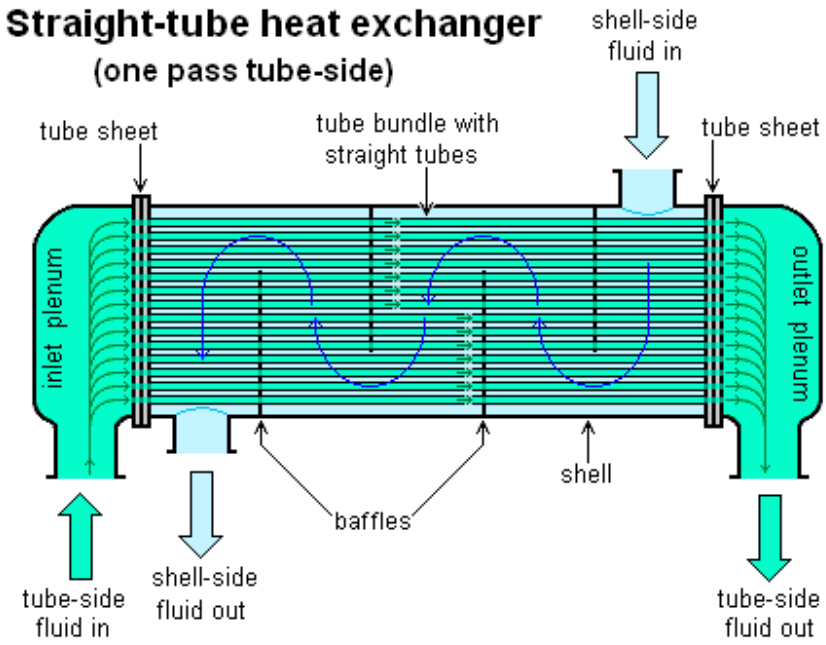

Figure 4.1: Scheme of a section of a shell-and-tube heat exchanger, from Padleckas (2006).

the diameter of the pipes.

The principles and findings described so far are, unfortunately, not entirely suitable for the study of convection-powered energy harvesting, because the exploitation of buoyancy is very different from the use of a constant water flow controlled by a pump. For this reason, in the context of this Thesis, experimental trials were designed to provide a starting body of information on convection-powered energy harvesting and to guide future research on the topic.

The lack of specific guidance on natural air flow in this kind of system led to an approach based on the comparison between heat exchangers and energy harvesting pavements. In particular, shell-and-tube heat exchangers with one pass tube-side (see Fig. 4.1) were used for this comparison. Such a system consists of a series of pipes containing a fluid that exchange heat with a second fluid flowing inside the shell. In the case of an energy harvesting pavement,

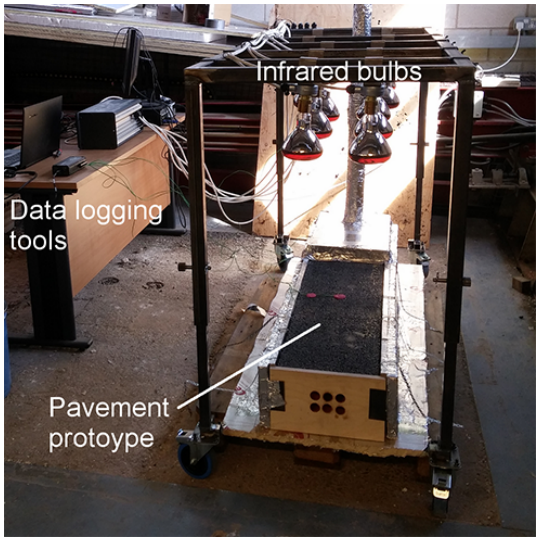

(a) Photo of the prototype in the laboratory.

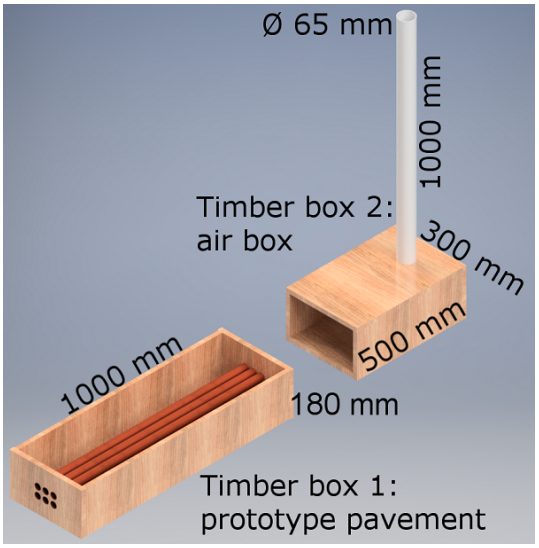

(b) Main parts of the prototype disassembled (project phase rendering).

Figure 4.2: Energy harvesting prototype powered by air convection for the study of construction techniques.

the analogy is made considering that the shell-side fluid is not moving, thus, considering it as the layers comprising the pavement.

Based on the experience obtained by analysing the energy harvesting prototype described in Chapter 3, a new energy harvesting prototype with a flexible layout was built (see Fig. 4.2). The new prototype consisted of two layers, i.e., an asphalt wearing course (maximum aggregate size of 10 mm, 6% air void content, 50 mm thickness) and an aggregate layer (silica sand, 130 mm thickness). The prototype described in this chapter was built to allow the study of:

- the effect of pipe arrangements based on the comparison with a shell-and-tube heat exchanger;
- the feasibility of a realistic construction technique considering precast concrete slabs with channels for the air flow.

The differences between the prototype seen in Chapter 3 and the experimental setup described in this section are gathered in Table 4.1. The aim of the changes

Table 4.1: Features of the energy harvesting prototype used in Chapter 3 and the setup shown in Fig. 4.2.

Feature	Prototype in Chapter 3	Prototype in Chapter 4
Pavement width	700 mm	300 mm
Pavement length	470 mm	1000 mm
Asphalt slab thickness	50 mm	50 mm
Prototype thickness	180 mm	180 mm
Air box width	700 mm	300 mm
Air box length	125 mm	500 mm
Pipe arrangement	Fixed	Variable
Material of the pipes	Steel	Copper
Aggregates	Gravel	Silica sand
Position of the chimney	Side	Top
Chimney height	Variable	1000 mm
Chimney diameter	Variable	65 mm

introduced in the new design was to improve the heat transfer performance within the pavement section and, in particular, to allow the air flowing through the system to absorb more energy. In fact, the prototype discussed in this chapter was used to evaluate the performance of the system with a range of pipe arrangements, which were not expected to yield highly different results. Therefore, pursuing better heat transfer within the system allowed the maximisation of the energy harvesting potential of each configuration considered, which, in turn, yielded clearly different results that could be easily told apart from one another. The design choices that were meant to improve the thermal performance of the pavement prototype were (i) the increased length of the system, (ii) the use of copper for the pipes in the place of steel (due to its higher thermal conductivity, see Kaye & Laby Online (2005)), and (iii) the use of silica sand in the place of gravel. Note that the width of the new prototype is lower than that of the previous one (see Table 4.1). This choice was made because (i) the

width of the structure holding the infrared bulbs used to heat up the pavement (see Fig. 4.2a) was fixed and (ii) the maximum size of the precast concrete slabs considered as an alternative to pipes was constrained by the equipment that was available and by practical concerns.

The reason why channels in concrete slabs were considered as an alternative to copper pipes is that they are more practical to install. In fact, controlling the pipe spacing is not easy when they must be placed in an aggregate layer at a chosen depth and with a chosen pitch ratio. On the other hand, concrete slabs can be laid on an aggregate layer due to the fact that the shape of the air channels is defined when slabs are fabricated. Furthermore, the use of pipes may not be an acceptable long-term solution as their cost is expected to be high, especially in the case of large installations.

All the external sides of the prototype seen in Fig. 4.2 were made of 18 mm thick timber and covered with extruded polystyrene foam and bubble foil to allow effective thermal insulation. The volume where the air mixes was called the air box, as in Chapter 3, in order to keep the same nomenclature. The chimney outlet was installed on top of the air box, as seen in Fig. 4.2. The sizes of all the major components of the prototype are displayed in Fig. 4.2b.

Finally, it is important to point out that the aim of this study was to test the effectiveness of the technology based on a constant total volume of air channels installed. Consequently, the energy harvesting pavement prototype built for this purpose was evaluated based on this approach and no conclusions can be drawn based on different metrics such as pipes installed per unit width of pavement. In fact, if that were the objective, edge effects would have a much stronger influence on the results and, therefore, they should be studied in detail.

4.1 Pipes buried in the ground

In heat exchangers, the components called tube sheets (see Fig. 4.1) are very important, because they hold the pipes in a specific arrangement. This aspect is relevant for energy harvesting pavements, because, in the literature, there is no information about how the pipes should be arranged under the asphalt wearing course in order to provide the most effective performance.

Therefore, a version of the tube sheets was developed and installed in the pavement prototype to test pipe arrangements in convection-powered energy harvesting pavements. The internal diameter chosen for the pipes was 30 mm. As shown in Fig. 4.3, five pipe arrangements were studied based on the technical guidance provided by Kakaç et al. (2012) in their analysis of the existing practice in the field of shell-and-tube heat exchangers. The implementation of

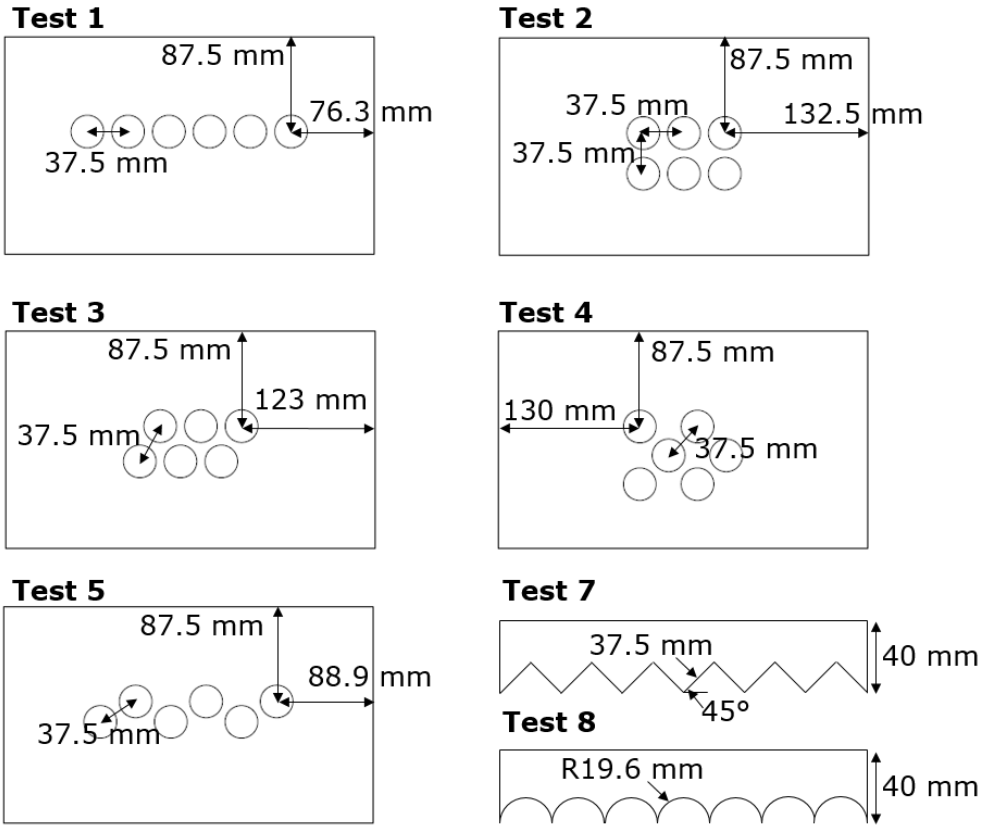

Figure 4.3: Configuration of the pipes and concrete corrugations.

Table 4.2: Overview of the experiments performed.

Test number	Objective
1	Pipes in a single row
2	Pipes installed in two rows, superimposed layers
3	Pipes installed in two offset rows with angle of 60° between pipes
4	Pipes installed in three offset rows with angle of 45° between pipes
5	Pipes installed in two offset rows with angle of 30° between pipes
6	No energy harvesting pipework
7	Concrete triangles
8	Concrete semicircles

the tube sheets consisted of perforated timber slabs placed both in the front and in the back of the prototype and able to hold the pipes in a chosen configuration (see Fig. 4.4). In addition, they allowed the control of the centre-to-centre distance of the pipes, i.e., the pitch ratio, which was fixed as 37.5 mm following the method outlined by Kakaç et al. (2012). As a result, the tests listed in Table 4.2 were performed in the laboratory.

Since the energy harvesting process requires the simulation of solar radiation, a set of six infrared bulbs (250 W each) were used. The infrared bulbs took the surface temperature up to about 80°C after a total time of 24 hours, after which steady state conditions were reached. This high temperature was preferred to more realistic values (e.g., 70°C, as reported by Pascual-Muñoz et al. (2013)) simply because preliminary tests showed that a higher temperature would allow an easier detection of the differences between all the configurations that were tested. The reason for this is that, in the laboratory, many thermal phenomena such as thermal convection and radiation cannot be controlled, thus, if the surface temperature is much higher than the environmental temperature, differences in the results related to differences in the experimental layouts are more easily seen.

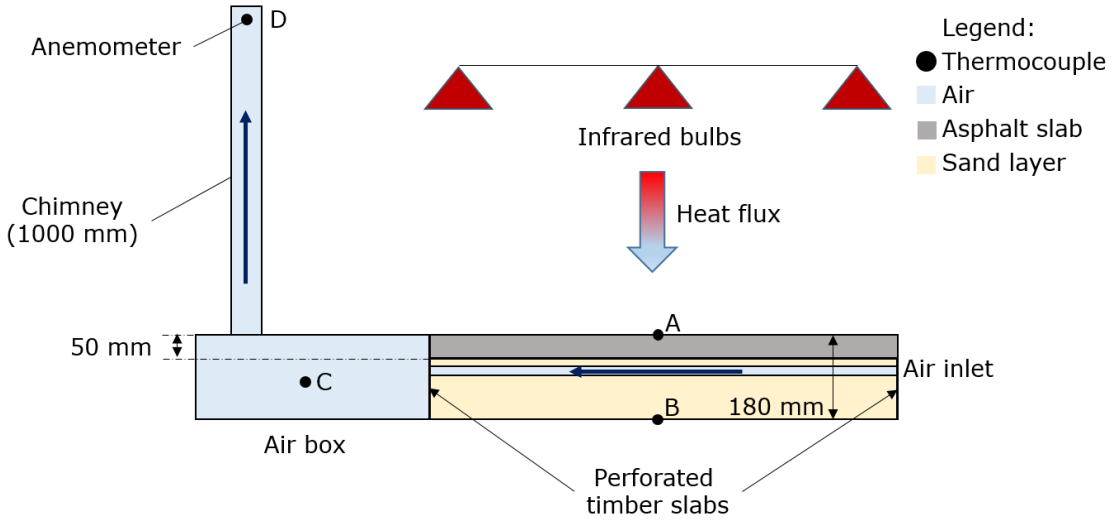

Figure 4.4: Cross section of the experimental setup and position of the thermocouples.

The temperatures in the system were monitored with thermocouples placed in the positions shown in Fig. 4.4, i.e., on the asphalt surface (position A), at the bottom of the system (position B), in the air box (position C), and at the chimney outlet (position D). As done in Chapter 3, the thermocouples were connected to an OMEGA OMB-82 DAQ-54 datalogger.

4.2 Concrete corrugations: manufacture and installation

As mentioned above, corrugated concrete slabs were considered as an alternative to the pipes in the energy harvesting pavement prototype. The slabs were manufactured by pouring concrete in timber moulds that were previously covered with a non-stick coating. The scheme of the installation of the slabs in the prototype pavement is shown in Fig. 4.5a, while the shapes of the corrugations that were chosen are pictured in Fig. 4.3. It can be observed that between the slabs and the sand layer a thin geotextile membrane was installed so that the

(a) Scheme of the concrete slabs; setup and position of the thermocouples.

(b) Photograph of the concrete slabs installed in the prototype.

Figure 4.5: Experimental configuration for testing concrete corrugations in the energy harvesting pavement.

roughness of sand would not influence the air flow. The thickness of the corrugated slabs was 40 mm and the total internal volume of the air channels was roughly the same as the total volume of pipes installed in the pavement prototype. This was done in order to keep a common parameter between the pipes and the concrete slabs, otherwise, it would have been hard to assess whether the performance of this construction technique was comparable or not to the original designs.

4.3 Energy and exergy in convection-powered energy harvesting

The results obtained in the experiments that were performed could not be easily interpreted because the arrangement of the components of the system changed every time. Consequently, in order to achieve a meaningful analysis of the results, the data were further processed. In particular, it was chosen to approach the analysis by calculating the energy absorbed by the pavement, Q_{abs}, during the energy harvesting process, as explained by Chiarelli et al. (2015*b*).

The expression used for this is the numerator of Eq. 3.2.1, where T_E should be replaced with T_D (with reference to Fig. 4.4). The other parameters needed for the calculation of Q_{abs} were found as reported in Section 3.2. Note that the unit of the numerator of Eq. 3.2.1 is W, thus, a suitable time interval must be considered to obtain a measure of energy.

Furthermore, the concept of exergy was used to provide a deeper insight in the interpretation of the results. As explained, e.g., by Çengel & Boles (2010), Paniagua et al. (2013), and Verda et al. (2014), the calculation of exergy leads to a more realistic representation of the energy available for use after the energy harvesting process. This is because the temperature of the environment is considered along with the temperature of the heat source to evaluate the maximum amount of work that can be done with the thermal energy stored in the air. This is done by means of the Carnot factor, η_{th}:

$$\eta_{th} = 1 - \frac{T_e}{T_c} \tag{4.3.1}$$

where T_e is the temperature of the environment in K and T_c is the temperature of the air at the chimney outlet in K. As a direct consequence of Eq. 4.3.1, it can be understood that the closer the temperature at the chimney outlet is to the environmental temperature, the lower the value of the Carnot factor will be. The Carnot factor is important because it allows the calculation of the exergy of the energy harvested B_{abs}:

$$B_{abs} = \eta_{th} \cdot Q_{abs} \tag{4.3.2}$$

As a result, if the Carnot factor is low, the value of exergy will be low. This means that if a pipe arrangement yields a low value of exergy the heat absorbed is close to the environmental temperature and, therefore, cannot be used effectively and efficiently in a thermal device without upgrading (e.g., through a heat pump system).

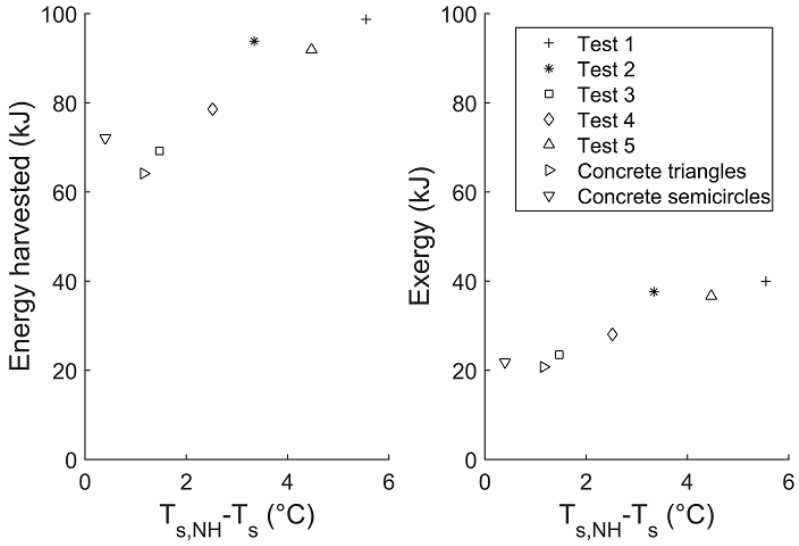

Figure 4.6: Surface temperature difference with no harvesting vs. Energy harvested and exergy.

In conclusion, exergy is used to compare in a more objective way the different pipe arrangements and construction techniques that were considered. In fact, due to the differences in geometry, heat transfer, and fluid-dynamics it is not possible to evaluate the performance based on a single criterion, e.g., the outlet air speed or the temperature reduction allowed by a given layout.

4.4 Performance of the system with different pipe arrangements and with concrete corrugations

The results of the experiments performed for the study of realistic construction techniques for convection-powered energy harvesting pavements are shown in Fig. 4.6-4.8 and are described by Chiarelli et al. (2015*b*). The values of energy on the vertical axis were calculated considering steady-state conditions using the method explained in Section 4.3 and a hypothetical period of 1 h.

The quantification of the effects of the energy harvesting process was pur-

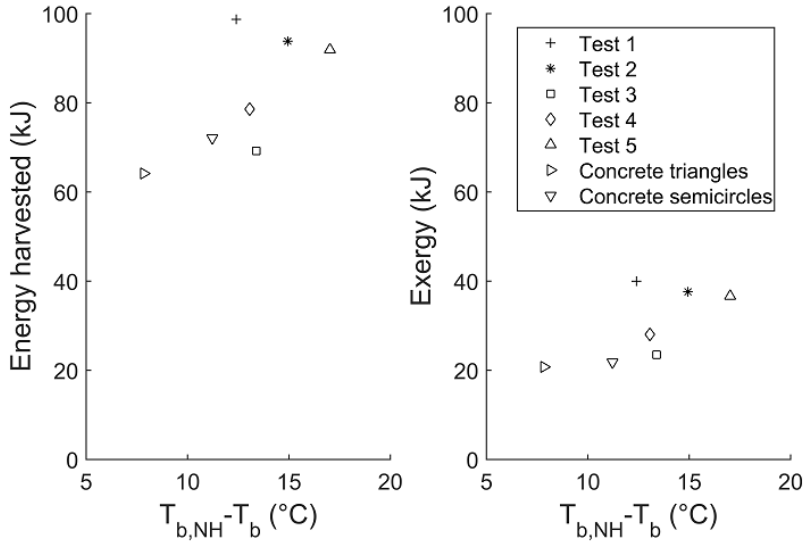

Figure 4.7: Bottom temperature difference with no harvesting vs. Energy harvested and exergy.

sued by calculating the difference between the temperatures measured in the experimental trials and the temperatures obtained with no energy harvesting. The former appear in Fig. 4.6 and 4.7 as T_s and T_b, while the latter are described by the subscript NH, which means "No Harvesting". The tests with no energy harvesting were performed by obstructing all the pipes, thus, not allowing an air flow through the pavement.

When Fig. 4.6-4.8 are examined, it must be kept in mind that the results belong to different datasets and are shown together just for the purpose of a comparison. Therefore, no trends can be found in such data. A first look at Fig. 4.6 and 4.8 suggests that Test 1 (all pipes in a row) provided the highest surface temperature reduction, the highest harvested energy, and a high air speed. As a result, the installation of all pipes in a row can be considered as a very effective option overall. In this analysis, the parameter that mostly determines the quality of a configuration is the reduction of the surface temperature, as it is more important than the bottom temperature when urban overheating, the UHI effect, and surface pavement shear under trafficking are considered. The

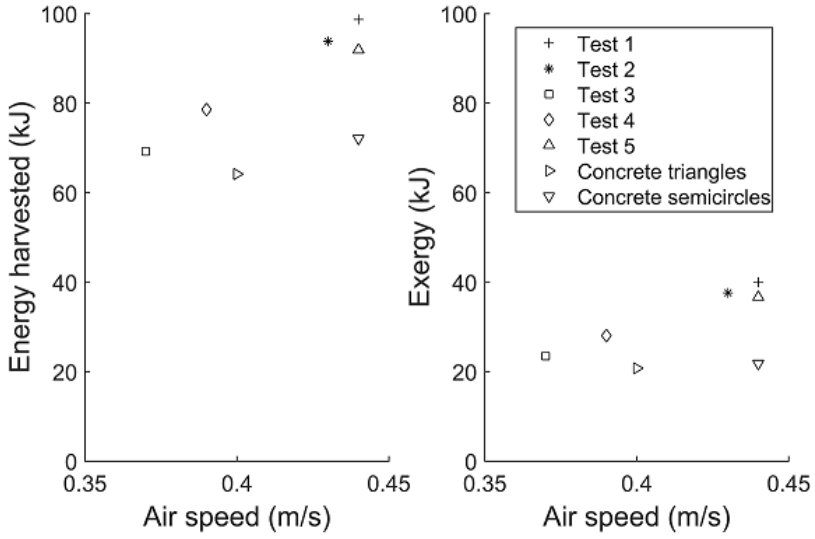

Figure 4.8: Air speed vs. Energy harvested and exergy.

reason for the better performance of Test 1 is that being closer to the surface the pipes can absorb the incoming thermal radiation more effectively. It is relevant to point out that if other purposes are taken into account the "best" configuration may differ (see, e.g., the different points of view presented in Section 3.2).

Furthermore, in Fig. 4.8, it can be observed that the concrete corrugations with the semi-circular cross section did not provide a very effective temperature reduction but allowed an outlet speed as high as the one found in Test 1.

One of the most striking details in the experimental results that were obtained is the fact that the range of variation of the values of exergy in Fig. 4.6 and Fig. 4.7 is smaller than that found for energy. In fact, the relative position of the points represented in the figures does not change between energy and exergy, however, the values of energy range between about 60 kJ and 100 kJ, while their exergy ranges between 20 kJ and 40 kJ. The comparison between energy and exergy clarifies that the actual gap between the different construction hypotheses that were considered is lower than would appear by considering energy alone. This is because the use of exergy in the place of energy allows a more realistic comparison between the performances of the configurations

under analysis based on the conversion of energy into work. This observation is very important, because it means that, under the assumptions made for this experimental campaign, the influence of the pipe arrangement on the final performance of the system is only minor.

When the concrete corrugations are considered, it appears quite clear that the development of this technique needs to be further pursued because of the quite low pavement cooling potential. The results obtained with the concrete slabs, however, were not unexpected, as (i) the roughness of concrete increases friction and reduces air velocity, thus, heat transfer to air is less effective; and (ii) concrete has a higher specific heat capacity than sand, which means that sand cooled down more quickly due to the lower amount of heat accumulated in the material. The somehow poor energy harvesting performance obtained with concrete slabs shows how such a system was meant as a simple pilot study to prove that concrete corrugations are a viable and somewhat more realistic option for the installation of convection-powered energy harvesting pavements. Further studies could focus on the construction of concrete slabs with improved thermal properties, different sizes, and different distances of the channels from the pavement surface (e.g., layers with different thicknesses).

Finally, it is important to point out that the energy harvested with the pavement prototype was always at a low temperature, even considering the rather high target surface temperature that was chosen for the experiments. This can be understood by considering the chimney temperatures obtained in the experimental trials, which ranged between 35°C and 41°C. Consequently, the energy harvested can be used only by low-enthalpy systems such as air-source heat pumps (see, e.g., Dongellini et al. (2015)) or thermal generators, since the production of large amounts of electricity with this technology is currently not a viable option.

4.5 Theoretical considerations on the outlet air speed

After looking in the current chapter (see Section 4.4) and in Chapter 3 at the values of air speed obtained, it appears clear that only rather low values were obtained. Such low air speeds are not fit to power a turbine (see, e.g., Singh & Ahmed (2013)) and they should be improved independently of the use of the harvested energy.Two methods are available for this purpose. The first and conceptually simplest solution is the modification of the thermal properties of the pavement, as hypothesised by, e.g., Pomerantz et al. (1997), Akbari et al. (1999, 2005), Gui et al. (2007), Synnefa et al. (2011), Dawson et al. (2012), Sarat & Eusuf (2012), Santamouris (2013), Carnielo & Zinzi (2013), and Guntor et al. (2014). The improvement of thermal properties would imply a higher heat absorption for the air flowing in the pipes (or channels), which in turn would allow a higher density difference between the outlet air box and the environment. As a result, the outlet air speed would be higher, as mandated by the physics of buoyancy-powered flows. This approach, however, makes asphalt pavements inevitably more expensive, thus, it might be unlikely for it to be widely adopted.

A second method to make air absorb more energy is to increase the length of its path under the pavement wearing course using, e.g., a serpentine. In this case, an issue might arise, because if the path of the air flow was made more complex the values of air speed could drop to even lower values instead of increasing. The reason for this is that the motion of air is controlled by natural convection and not by a chosen pressure differential, which would be the case if a fan were used. In order to provide further understanding of this phenomenon, it is helpful to introduce the concept of geometric tortuosity generally used for porous media. As explained by Gommes et al. (2009), this parameter is defined as the ratio between the length of a path completely inside

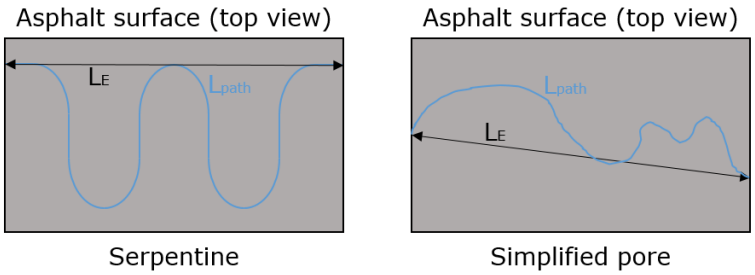

Figure 4.9: Parameters for the calculation of the tortuosity of a path (serpentine vs. simplified pore).

the pores and connecting two opposite faces of the material and the Euclidean distance between its start and end points (see Fig. 4.9):

$$\tau_g = \frac{L_{path}}{L_E} \tag{4.5.1}$$

where τ_g is the geometric tortuosity, L_{path} is the actual length of the path in the air pores of the material, and L_E is the Euclidean distance.

If a straight channel (e.g., a pipe or channels in a corrugated slab) is considered as a highly idealised pore, it will have a tortuosity of 1. Then, if the shape of such a channel were changed and made more complex, the tortuosity would increase based on Eq. 4.5.1. An increase in the tortuosity would lead to a decrease in the permeability of the air channel, which, in the case of gases, is measured using Darcy's law and is a function of the pressure difference between the ends of the material (see Bejan (2013)):

$$\kappa = v\frac{\mu\Delta x}{\Delta p} \tag{4.5.2}$$

where κ is the permeability of the material, v is the fluid velocity in the pores, μ is the dynamic viscosity of the fluid, Δx is the thickness of the material, and Δp is the pressure difference between the inlet and outlet of the pore(s).

When the tortuosity increases, in Eq. 4.5.2, a higher pressure is needed to obtain the same value of air flow seen with a straight channel. The reason for this is that a higher tortuosity generally implies higher head losses throughout the

path of the fluid. In fact, a higher length of the path causes higher friction losses and the presence of curves and potential changes in the cross section cause minor losses originated because of the disruption of the flow. These losses are highly important in the case of convection-powered flows in energy harvesting pavements, because they are ruled by rather low pressure differences. This means that, based on the experimental results obtained in Chapter 3 and in Section 4.4, paths more complex than straight lines may cause the air speed to decrease to values that are not acceptable for any purpose.

Therefore, the use of a serpentine layout could work if the the air flow were facilitated by a low-powered fan sized to overcome the head losses through the path. The use of this configuration, however, should undergo a thermoeconomic analysis, to assess whether the overall performance would be high enough to justify the additional energy consumption and expense.

Based on the ideas presented above, it appears clear that it would be desirable to further understand the role of pipes in convection-powered energy harvesting pavements. In fact, since pipes can be considered as highly idealised pores for the purposes of air flow through the pavement, it is natural to wonder whether they could be replaced by the pores themselves. In Chapter 7, asphalt pores are studied to assess their fitness for a low speed air flow and to evaluate if pipes are a necessary component in the convection-powered energy harvesting technology.

4.6 Air speed and head losses in the concrete corrugations

The results presented about the concrete corrugations in Fig. 4.6 and 4.7 cannot be easily interpreted, because it is not possible to compare this construction

technique to the pipes from the point of view of fluid-dynamics. Therefore, it was decided to perform simplified flow simulations in single channels with the cross sections shown in Fig. 4.3 using a fixed pressure difference of 20 Pa between inlet and outlet. This was done to compare the outlet flow rates obtained with the different cross sections and to determine how friction losses affect the air flow based on the shape of the channels. The pressure difference of 20 Pa, was chosen because values in this order of magnitude are usually considered when it is necessary to obtain a controlled natural convective flow between areas of a building, as reported by WHO (2007) and Whyte (2001). Therefore, such a value was expected to be representative for a quite small air flow such as the one seen in the experiments performed in the present chapter. It is clear that the choice of this pressure difference was arbitrary, however, the results of the simplified simulations were only used to compare head losses based on the shape of the channels and not to draw any other kind of conclusion for the whole energy harvesting setup.

The simulations were performed using the Navier-Stokes equation implemented in the software Autodesk Simulation CFD and further discussed in Section 6.2.

The results obtained through the CFD software showed that the reason for the lower outlet speed in the case of the triangular corrugation is related to the higher friction losses. In fact, with a pressure difference of 20 Pa between the inlet and outlet of the channel a relative difference in the outlet air speed of 16% was found between semicircular and triangular cross sections. This value is compatible with the relative difference between the outlet air speeds found experimentally for the concrete corrugations, which is about 10% (based on Fig. 4.8). The small mismatch between such results is related to three reasons, i.e.:

- the pressure difference used in the simulations was not the same as the one found experimentally, as this information was not available;
- the presence of eddies in the outlet air box (see Section 6.2.1) influenced the results obtained, while this aspect was not considered in the simulations described in this section;
- the lack of thermodynamics in the simplified simulations.

However, the result of the simulations clarified the reason why the semicircular corrugations outperformed the triangular ones. In fact, Bobes-Jesus et al. (2013) reported that a lower speed inside the energy harvesting channels caused a decrease in the energy harvesting potential, which means that fluid dynamic losses were responsible for a lower heat (thermal energy and exergy) absorption in the case of the triangular cross section. This phenomenon can be seen by comparing the results in Fig. 4.6-4.8 for the two concrete corrugations considered. As a result of a lower heat absorption, the density difference between the outlet air box and the chimney outlet is lower, thus, a lower air speed is expected when the flow is powered by buoyancy. Therefore, semicircular channels should be preferred due to their better fluid-dynamics behaviour, which allowed more effective pavement cooling in the cases considered.

CHAPTER 5

Energy harvesting in the environment

Energy harvesting pavements using water as the operating fluid have been tested in the laboratory and designed for use in actual roads. Numerous examples of this can be found in the literature, see e.g., Guldentops et al. (2016), Wu et al. (2011), Chen et al. (2011), Pascual-Muñoz et al. (2013), and Siebert & Zacharakis (2010). Commercial installations of energy harvesting pavements using water were also performed, as shown, e.g., in Fig. 5.1. Practical applications of convection-powered energy harvesting are, however, not considered in the literature, probably due to the very young age of the technology and to the difficulties related to the use of air. In fact, testing convection-powered energy harvesting pavements in the environment poses unique challenges, as a hypothesis for the configuration of the system must be made. In this Thesis, the configuration chosen is the one shown in Fig. 5.2 and discussed by Chiarelli et al. (2016). The concept in Fig. 5.2 shows that air could be allowed to enter the deep layers of the road and absorb geothermal heat from it. Then, owing to the decreased density due to the higher temperature, it would flow upwards and exit through a vertical chimney, which could be, e.g., a street lamp pole.

Figure 5.1: Example of asphalt solar collector (ICAX).

This particular layout was chosen to allow the use of the energy harvesting pavement both in summer and in winter. In fact, the research done for the preparation of this Thesis started as a study of heat absorption using air, but it evolved into a more complex work aimed at finding a suitable role for the technology during the whole year. The observation of Fig. 5.2a clarifies the last statement: in the figure, two heat fluxes are represented, one labeled "pavement cooling" and the other one called "pavement heating". The former corresponds to summer conditions or warm climates, when the air harvests heat from the pavement, while the latter represents energy release from the warmed-up air to the pavement during winter or in cold climates. This is possible because the heat exchange with the soil pre-heats the air flow during winter, thus, allowing the presence of a buoyant flow through the pavement. In fact, the difference between summer and winter is that, when the pavement is hot, there is no need for pre-heating, as buoyancy would be naturally present in the system, while, during cold periods, the pre-heating must exist in order to obtain an air flow based on natural convection.

In order to verify the feasibility of the concept, the energy harvesting pro-

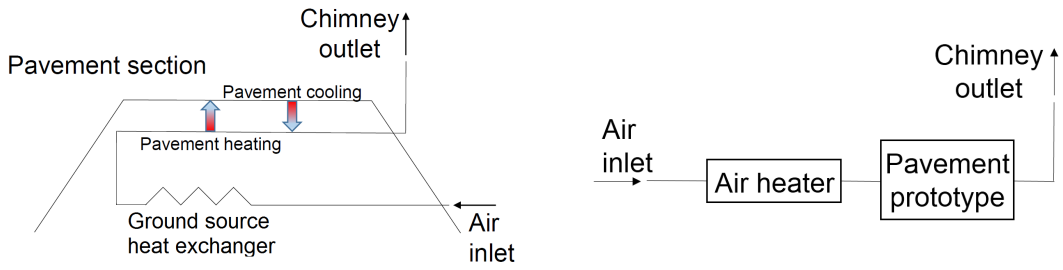

(a) Hypothetical full sized apparatus.

(b) Small-scale adaptation.

Figure 5.2: Concept of convection-powered energy harvesting pavement.

totype used in Chapter 3 was installed on a novel piece of equipment that was called a Ground Source Heat Simulator (GSHS), which is shown in Fig. 5.3 and described in the next Section 5.1. The use of the prototype from Chapter 3 is simply related to practical reasons, as its smaller size allowed the construction of a compact experimental setup. The following experimental trials were conducted using the GSHS:

- test of simulated summer and winter conditions in the laboratory (Section 5.2);
- test of the GSHS in the natural environment (Section 5.3).

5.1 The Ground Source Heat Simulator (GSHS)

The GSHS was built at the Nottingham Transportation Engineering Centre to simulate the geothermal heat exchange between warm ground and environmental air. In particular, the equipment built consists of a highly insulated stainless steel cabinet where a series of components have been installed to feed air at a controlled temperature to the energy harvesting prototype. The description that follows is partially based on the information available in Chiarelli et al. (2016).

A scheme of the GSHS is available in Fig. 5.4 along with the size of the

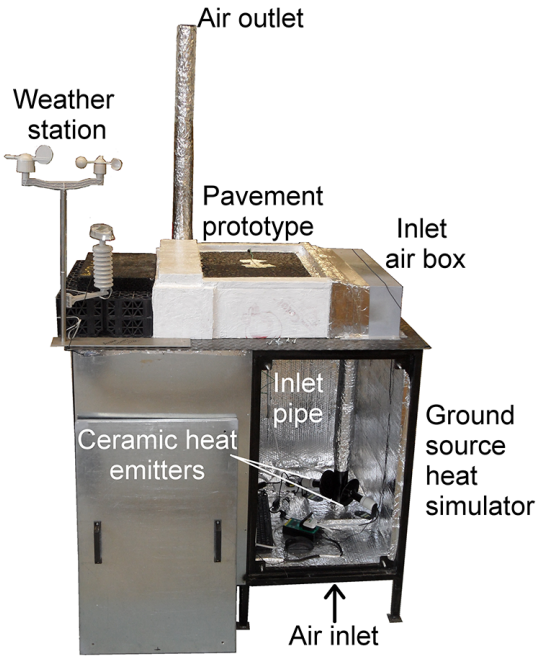

Figure 5.3: The Ground Source Heat Simulator (GSHS).

equipment. In Fig. 5.4, it can be observed that air enters the GSHS from the bottom of the cabinet, it is heated by ceramic heat emitters, and then reaches a volume called the inlet air box, which connects the GSHS to the inlet of the energy harvesting prototype. The regulation of the temperature inside the inlet air box is performed by means of a thermostat, which is able to turn on or off the ceramic heat emitters. As a result, the temperature regulation is discrete and not continuous. Nevertheless, preliminary experimental trials showed that this control mechanism was effective for the chosen application. Note that, in the experimental setup chosen, no cooling was possible for the inlet air box. Therefore, in principle, inlet temperatures higher than the one set in the thermostat could be obtained (see, e.g., Fig. 5.8).

In addition to what is shown in Fig. 5.4, an extractor fan was installed in the GSHS, so that the temperature inside the cabinet would not rise above 20°C. This was done to avoid any type of influence due to high temperatures on the

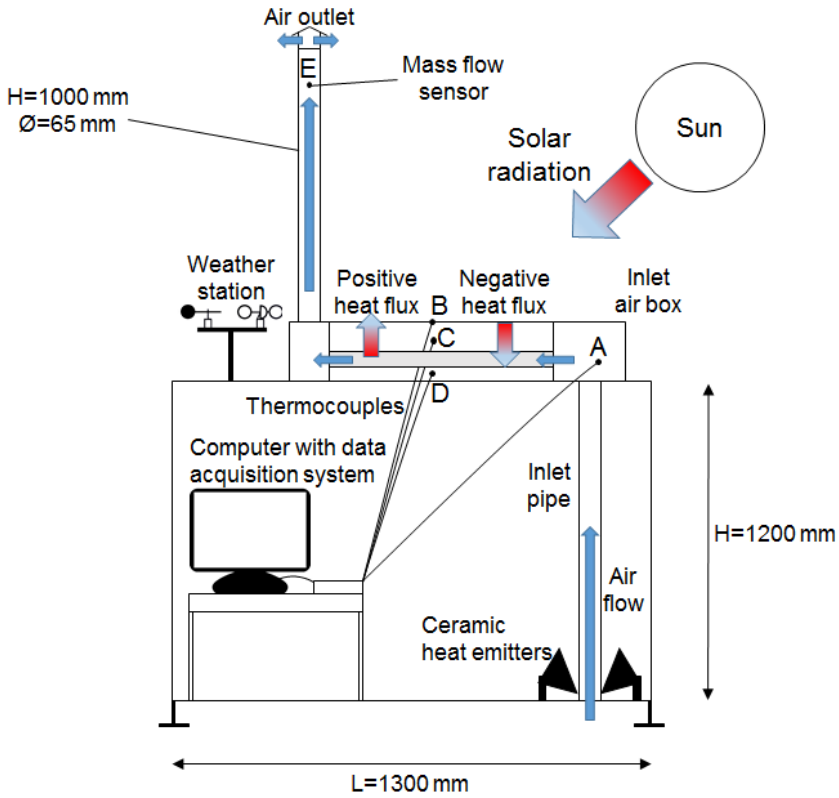

Figure 5.4: Scheme of the Ground Source Heat Simulator (GSHS), width= 1300 mm. Points A, B, C, and D indicate the position of the thermocouples.

data logging equipment.

The measuring tools seen in Fig. 5.4 and used for the experimental trials are an OMEGA OMB-DAQ-54 datalogger[1] with OMEGA K-type thermocouples (limits of error: $\pm 1.1°C$)[2] and a PCE-FWS 20 weather station[3]. Furthermore, two tools were used to measure the outlet air speed in the prototype - a PCE-423 anemometer[4] (see Chiarelli et al. (2016)) and an IST FS5 thermal mass flow sensor[5]. The thermal anemometer was used in the laboratory tests in steady state conditions, while the thermal mass flow sensor was used in a field study,

[1]Manufactured by OMEGA ENGINEERING, United Kingdom, see www.omega.co.uk.
[2]ibid.
[3]Manufactured by PCE Instruments, United Kingdom, see www.pce-instruments.com.
[4]ibid.
[5]Manufactured by Innovative Sensor Technology, Switzerland, see www.ist-ag.com.

Table 5.1: Parameters measured in the GSHS

Parameter	Unit	Instrument Used
Surface temperature of the prototype pavement, T_B	°C	OMEGA OMB-DAQ-54 datalogger
Temperature at 50 mm from the surface of the prototype pavement, T_C	°C	
Temperature at 130 mm from the surface of the prototype pavement, T_D	°C	
Temperature in the inlet air box, T_A	°C	
Surface temperature of the control slab	°C	
Outlet air speed, v_E	m/s	OMEGA OMB-DAQ-54 datalogger PCE-423 anemometer IST FS5 thermal mass flow sensor
Outdoor temperature	°C	PCE-FWS 20 weather station
Outdoor relative humidity	%	
Dew point	°C	
Absolute pressure	hPa	
Wind speed	m/s	
Gust	m/s	
Wind chill corrected temperature	°C	
Rainfall	mm	
Rainfall in the previous 24 h	mm	

since it has data logging capabilities. The use of these tools, allowed the measurement of the parameters seen in Table 5.1.

5.2 Laboratory testing of the GSHS

Before installing the GSHS in the field, it was thoroughly tested in the laboratory in order to verify that the equipment behaved as expected. As seen in Fig. 5.3, the energy harvesting prototype coupled with the GSHS is the same one described and tested in Chapter 3 (chimney height 1000 mm, internal diameter 65 mm). With reference to Fig. 5.4, the temperatures measured in the laboratory experiments were T_A, T_B, T_C, and T_D, while the air speed was measured at point E.

Table 5.2: Simulated winter and summer conditions in the laboratory.

Simulated season	Temperature in the inlet air box, T_A (°C)								IR bulbs	Chimney
Winter	23	24	25	26	27	28	29	30	Off	Yes/No
Summer	22	24	26	28	30	32	34	36	On	Yes

The laboratory testing was performed by considering simulated summer conditions and simulated winter conditions. Simulated conditions were used because in a laboratory environment it is not possible to reach real winter or summer conditions, unless a very large environmental chamber is used. The experimental conditions that were considered are summarised in Table 5.2. The main difference between the two simulated seasons is that, in the case of summer, infrared bulbs (6 bulbs, 250 W each) were used to reach a surface temperature of about 78°C. This temperature is almost 10°C higher than maximum asphalt temperatures reported by Pascual-Muñoz et al. (2013) for summer conditions. This was done so that inlet temperatures between 22°C and 36°C, which are about 10°C above realistic inlet temperatures, could be used. In this way, the lower end of the asphalt inlet temperature interval represents the temperature difference that would exist with a realistic soil temperature, while the higher end of the interval represents the temperature difference if the inlet air were to be the exhaust air from a hypothetical building.

On the other hand, in order to simulate winter conditions the ambient temperature in the laboratory (20.5°C) was considered as the soil minimum temperature elevated by approximately 15°C, while the temperature in the inlet air box was set between 23°C and 30°C (representing a 15°C elevation above the temperature of air that had been passed through the ground containing heat from the previous summer). Therefore, the temperature difference between the pavement and the simulated reservoir in simulated winter conditions was between 2.5°C and 9.5°C. During the tests in simulated winter conditions, the

temperature of a control asphalt slab with no energy harvesting pipes was also monitored, so that the effects of the air flow on the pavement prototype could be easily monitored.

A further difference between the simulated seasons is that the tests were performed both with and without a chimney in the case of winter, while the chimney was always used in the case of summer. The reason for this is that, in Section 3.1, the lack of a chimney caused a very poor performance during energy harvesting, which here corresponds to simulated summer conditions. As a result, performing tests with no chimney in this scenario was expected not to yield any relevant insight.

It is clear that fixing a temperature difference is not the same as testing the prototype in the environment. However, the experiments performed provided insight on the working mechanism of the GSHS and proved its effectiveness. In addition, the approach was deemed acceptable because the amount of energy that is harvested by air in the pipes is a function of the temperature difference between inlet air and surface temperature, rather than of these temperatures alone. As a result, if thermal phenomena on the surface are neglected, studying the effects of a temperature difference between inlet air and surface temperature is expected to approximate reasonably in-situ conditions. Furthermore, in Section 5.3, tests of the same experimental setup, but in the natural environment, are described so that more realistic information can be analysed.

5.2.1 General description of the experimental results

To begin with, it is important to point out that due to the different working mechanisms of the system in simulated winter and summer conditions the data need to be analysed differently. In the former case, the most important parameter to consider is the temperature increase caused by the air flowing in the

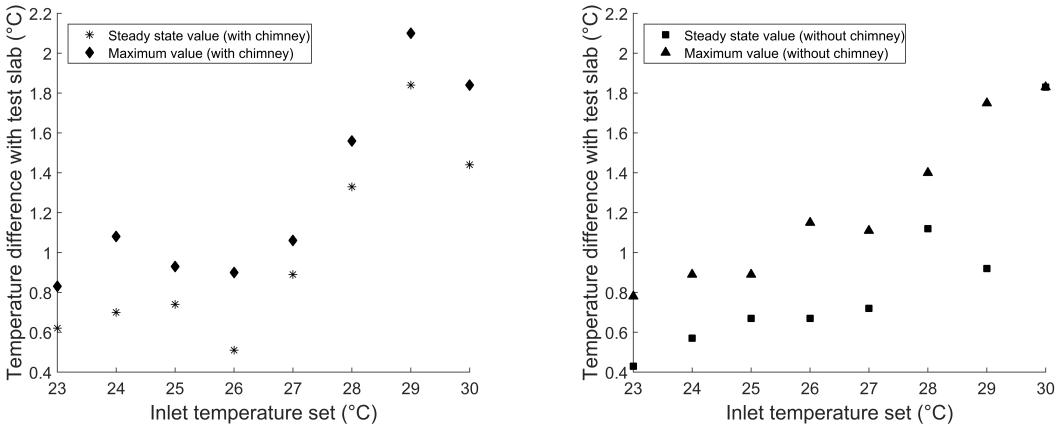

(a) Tests with chimney.

(b) Tests without chimney.

Figure 5.5: Temperature differences with control slab (Laboratory simulated winter conditions).

pipes on the pavement prototype. This was achieved by comparing the surface temperature of the prototype to the surface temperature of the control slab mentioned in Section 5.2. On the other hand, in simulated summer conditions, the most important parameters were the outlet air speed and the pavement temperature (relative to the temperature when no energy was harvested), which provide information on the amount of energy harvested from the pavement. Based on these principles, selected experimental results are shown in Fig. 5.5 and 5.6. The observation of Fig. 5.5 and 5.6 suggests that increases in the inlet temperature always cause increases in the other relevant parameters shown on the vertical axis. As a matter of fact, approximately linear relationships are seen in the above-mentioned figures, with higher linearity for summer than for winter. The small scatter seen in the simulated winter conditions was inevitable and is related to the fact that the environmental conditions in the laboratory were not perfectly stable from a thermodynamic standpoint. Furthermore, the comparison between Fig. 5.5a and 5.5b shows that in simulated winter conditions the presence of the chimney does not have a strong influence on the results.

As a preliminary proof of the effectiveness of the GSHS, it is important to point out that the temperature differences measured for simulated conditions were:

- between 0.48°C and 2.1°C for winter;
- between 2°C and 6°C for summer.

While the temperature difference for winter was calculated using the control slab, this was not possible for summer due to the experimental configuration chosen. Therefore, the difference found for summer conditions was calculated by comparing the temperatures obtained in the experimental trials with that obtained by a prototype with no energy harvesting (i.e., with the pipes obstructed), which was about 80°C.

Finally, in Chapter 3 (see Fig. 3.5) peaks in the air speed were observed, while no trace of them is seen in Fig. 5.6. The reason for this is simply that in Fig. 3.5 varying experimental configurations in terms of chimney height and diameter were considered, while, in Fig. 5.6, such parameters were kept constant. As a result, the air speed was solely influenced by the inlet temperature, which could not cause any local maximum or minimum point for the range of variation considered (see Table 5.2).

5.2.2 Simulated winter conditions

In order to analyse the results obtained with the GSHS, it was decided to use the Pearson's correlation coefficient. For more information on this approach, see, e.g., Rodgers & Nicewander (1988), Ferguson (2009), or Kent et al. (2015). The Pearson's correlation coefficient ranges between -1 (total negative correlation) and +1 (total positive correlation) and is able to show if a linear relationship exists between any couple of parameters under investigation. For the analysis of the experimental results obtained from the laboratory trials of the GSHS,

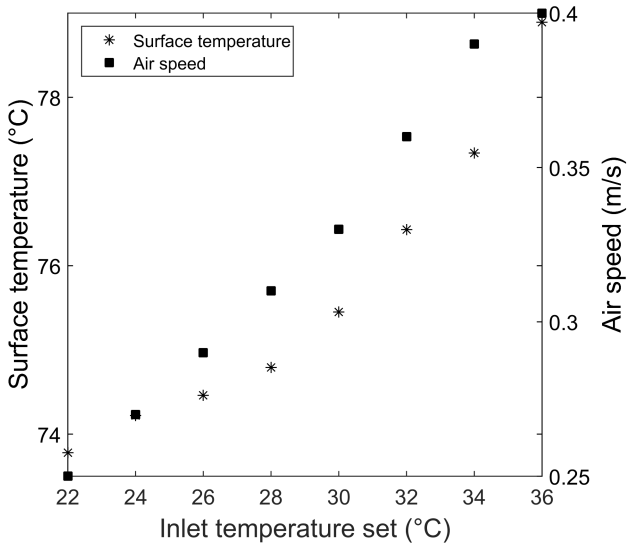

Figure 5.6: Surface temperature and air speed vs. Set inlet temperature (Laboratory simulated summer conditions, with chimney).

values of the Pearsons's coefficient, r, below -0.8 or above +0.8 were considered as an indication of a strong correlation. All other values were discarded, as they were not relevant for the purposes of the study.

Furthermore, due to the size of the dataset and to the lack of consistent directionality in the experimental results, the 2-tailed level of significance was calculated to investigate the trends of data in both directions (see Table 5.3).

In Table 5.3, an analysis of the Pearson's correlation coefficient found in simulated winter conditions is shown. A combined analysis was made for the configurations with and without chimney, because Fig. 5.5 suggested that the chimney's presence did not influence trends in the results. The analysis of Table 5.3 clearly shows that many linear correlations are present in the dataset under investigation. The most important results are the strong and positive linear correlations between:

- the temperature set and the outlet air speed ($r = 0.933$);
- the temperature set and the surface temperature ($r = 0.961$ for the maximum value and $r = 0.853$ for the steady state value).

Table 5.3: Pearson's correlation coefficient for the simulation of winter conditions. The subscripts refer to the thermocouple positions shown in Fig. 5.4.

	T_B	ΔT_{max}	ΔT_f	v_E	$T_{control}$	T_D	T_C	T_A	T_{set}
T_B	1								
ΔT_{max}	0.129	1							
ΔT_f	-0.275	0.846**	1						
v_E	-0.079	0.850**	0.835**	1					
$T_{control}$	0.959**	-0.137	-0.536	-0.316	1				
T_D	0.739*	0.734*	0.365	0.573	0.541	1			
T_C	0.996**	0.154	-0.273	-0.051	0.955**	0.752*	1		
T_A	0.518	0.837**	0.557	0.766*	0.290	0.949**	0.531	1	
T_{set}	0.123	0.961**	0.853**	0.933**	-0.144	0.753*	0.141	0.891**	1

*Correlation is significant at the 0.05 level (2-tailed).

**Correlation is significant at the 0.01 level (2-tailed).

Legend:

All temperatures are in °C, air speed (v_e) is in m/s.

T_B=surface temperature of prototype pavement, $T_{control}$= surface temperature of control slab,

$\Delta T_{max} = max(T_B - T_{control})$, $\Delta T_f = (T_B - T_{control})_{steady\ state}$,

v_E= air speed, T_D= temperature at 130 mm from surface of prototype pavement,

T_C= temperature at 50 mm from surface of prototype pavement,

T_A= temperature at inlet air box, T_{set}= inlet temperature chosen

These results represent the proof that the system can be controlled by setting an appropriate inlet temperature. The temperature set also has a strong linear correlation with the temperature in the inlet air box ($r = 0.891$), which is a sign that (i) the thermostat-controlled temperature regulation is effective and (ii) there is air stagnation in the inlet air box, which keeps the temperature very similar to the temperature set. In fact, this correlation would, probably, not be as strong if the inlet pipe was connected to the energy harvesting prototype, e.g., with a manifold. A further discussion on air stagnation in the system is found in Chapter 6.

The correlation between the temperature set and the bottom temperature of

the prototype ($r = 0.753$) is not as strong as the other correlations described, however, it is relevant to mention it because it characterises the experimental setup used. In fact, such a correlation describes heat accumulation in the prototype and is related to the presence of thermal insulation around the pavement prototype.

Furthermore, one should consider the correlations between the surface temperature and the temperatures in the deeper layers of the pavement ($r = 0.996$ for T_C and $r = 0.739$ for T_D). These correlations are important because they show that the pavement behaves in accordance with the physical laws that are described in Section 2.3, i.e. thermal conduction in the top layer and thermal convection at a higher depth. The presence of thermal convection is not explicitly described by the Pearson's correlation coefficient, however, it is implied by its lower value when T_D is considered. This is because thermal convection is not a linear phenomenon (see, e.g., White (2002)) and it causes the strength of the linear correlation to decrease.

Finally, there exists a strong and positive correlation between the temperature difference between the pavement prototype and the control slab and the outlet air speed ($r = 0.850$ for the maximum value and $r = 0.835$ for the steady-state value). This is in agreement with the findings of Bobes-Jesus et al. (2013), who reported that a higher speed of the fluid is able to improve heat transfer phenomena due to a higher convective heat transfer coefficient.

5.2.3 Simulated summer conditions

The correlation analysis performed for simulated summer conditions is shown in Table 5.4. The most interesting observation about Table 5.4 is that all the values are positive and higher than 0.485, which means that almost all correlations were linear. The inlet temperature chosen has a strong and positive linear cor-

Table 5.4: Pearson's correlation coefficient for the simulation of summer conditions. The subscripts refer to the thermocouple positions shown in Fig. 5.4.

	T_B	v_E	T_D	T_C	T_A	T_{set}
T_B	1					
v_E	0.917**	1				
T_D	0.995**	0.932**	1			
T_C	0.997**	0.942**	0.996**	1		
T_A	0.774*	0.516	0.738*	0.739*	1	
T_{set}	0.907**	0.997**	0.928**	0.935**	0.485	1

*Correlation is significant at the 0.05 level (2-tailed).

**Correlation is significant at the 0.01 level (2-tailed).

Legend:

All temperatures are in °C, air speed (v_e) is in m/s.

T_B=surface temperature of prototype pavement, v_E= air speed,

T_D= temperature at 130 mm from surface of prototype pavement,

T_C= temperature at 50 mm from surface of prototype pavement,

T_A= temperature at inlet air box, T_{set}= inlet temperature chosen

relation with the surface temperature ($r = 0.907$), the air speed ($r = 0.997$), the bottom temperature ($r = 0.928$), and the top temperature ($r = 0.935$). Therefore, the experimental data gathered suggests that setting lower temperatures on the inlet thermostat will cause lower pavement temperatures. The reason for this is that if the inlet temperature is lower there will be a higher temperature difference between the pavement surface and the air flowing in the pipes, thus, allowing more effective heat transfer.

In addition, there is a positive correlation between air speed and all the pavement temperatures measured. This means that the air in the outlet air box has a higher energy content when the pavement is hotter. Therefore, a higher pressure difference exists with the environment, which results in a higher speed at the system outlet due to buoyancy. Furthermore, if simulated winter and

summer conditions are compared, it can be noticed that the air speed is not linearly related to the surface temperature in winter ($r = -0.079$), while it is in summer ($r = 0.917$). The reason for this is likely to be that simulated winter and summer had different boundary conditions:

- in summer, an incident heat flux provided energy directly to the pavement;
- in winter, the air in the pipes released low temperature heat to the pavement.

Therefore, during simulated summer conditions the air flow was caused by a heat flux and, consequently, by the temperatures in the pavement layers, while, in winter, the cause for the movement of air was the inlet temperature set. This means that during simulated winter conditions heat transfer to the pavement was very low and its effect can hardly be seen on the outlet air speed.

Finally, it can be observed that there was a strong linear correlation between the surface temperature and the other pavement temperatures. This confirms again the validity of the principles described in Section 2.3. The correlation coefficient between the surface temperature (T_B) and the bottom temperature (T_D) is higher in summer than it is in winter. The reason for this is just that the surface heat flux in simulated summer conditions has a far stronger effect than the internal convection flux seen in simulated winter conditions. Furthermore, the presence of thermal insulation makes this effect even stronger. As a result, the non-linear effect due to convection has a smaller influence on the bottom temperature during summer conditions, because it is overcome by the stronger heat flux on the pavement surface.

5.3 Performance of energy harvesting in the environment

After preliminary testing in the laboratory, the GSHS was installed in the natural environment to evaluate its performance in more realistic conditions. The target temperature chosen for the inlet air box for these trials was 15°C. The equipment was installed at the University of Nottingham, UK (see Fig. 5.7), for the period of time between September 4th, 2015 and January 4th, 2016. The data logging frequency chosen was 15 minutes and about 7500 data points were gathered for the parameters shown in Table 5.1. The equipment used was turned off for routine maintenance for about 1 week every month. In the next sections, the methods of analysis used and the results obtained from the external installation of the GSHS are gathered.

5.3.1 Theoretical and statistical methods for the analysis of the dataset

The data obtained from the external installation included parameters of different nature and with non-trivial relationships with one another. Therefore, a statistical analysis of the results obtained was performed by means of the Pearson's correlation coefficient, as explained in Section 5.2.2. The only difference with what was stated in Section 5.2.2 is that, in the present case, new conditions were used to analyse the data due to the larger size of the dataset. In particular, values of the coefficient between 0.7 and 1 or -0.7 and -1 were considered as a sign of a strong relationship between the data, while values between 0.4 and 0.7 or -0.4 and -0.7 were considered as a sign of a moderate relationship. This difference is simply related to the fact that, in the investigation carried out in the laboratory (see Section 5.2), the number of data points was much smaller,

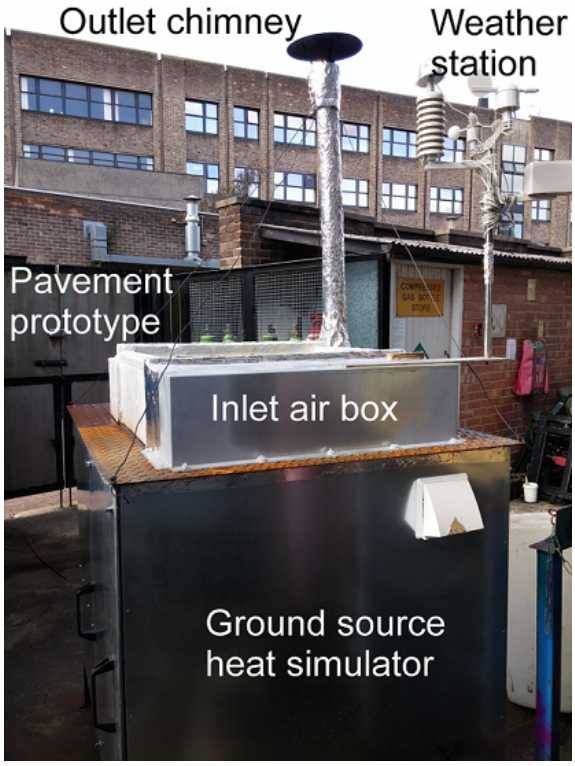

Figure 5.7: GSHS installed in the environment at the University of Nottingham, UK, adapted from Chiarelli et al. (2016).

thus, more stringent criteria had to be selected to develop reasonably strong conclusions based on the experimental results.

During the operation of the system in the environment, the air flowing through the pipes installed in the pavement prototype was expected to release or absorb heat based on the weather conditions. Therefore, it is possible to try and evaluate the amount of energy that was exchanged between the pavement and the air in the pipes. In order to achieve this, the pavement prototype installed on the top of the GSHS was compared to a control slab, as done in Section 5.2. This approach is reasonable only under an assumption, i.e., that the pavement prototype and the control slab are highly similar. This hypothesis was deemed acceptable because the thermal mass (product of mass and specific heat capacity) of the two pavement sections is similar, since having a mass of air inside the pavement prototype cannot not influence much its thermal prop-

erties, especially considering that, in this case, it occupied only about 2% of the overall volume.

Thanks to this assumption, a further simplification was made, i.e., the pavement sections were considered as if they had a constant temperature throughout their bodies, which is the same as considering them as points with a given mass, temperature, and physical properties averaged over the components of the mixtures. This simplification is arbitrary, however, it was justified by the fact that the average difference between the surface temperature and the temperature in the top layer of the prototype was as low as 1.10°C for the data that was collected.

Therefore, if the slabs are considered at thermal equilibrium with the environment at all measurement steps, it is possible to evaluate the thermal energy absorbed or released by the air in the pipes, Q, as:

$$Q = m_{slab} \cdot c_p \cdot (T_B - T_{control}) \tag{5.3.1}$$

where m_{slab} is the mass of the pavement Section, c_p is the specific heat capacity, T_B is the surface temperature of the prototype pavement, and $T_{control}$ is the surface temperature of the control slab. The values of the parameters used are $m_{slab} = 121$ kg and $c_p = 0.93$ kJ/(kg K) and the specific heat capacity is a mass weighted value including both layers of the prototype. These values were calculated based on the properties reported by Hassn et al. (2016b).

The use of Eq. 5.3.1 allows the evaluation of the heat exchange that is caused by the air flowing in the energy harvesting pipes. In particular, the following conditions can exist:

- $T_B > T_{control}$, meaning that the heat exchanged is positive for the pavement, i.e., it receives energy from the air flow;
- $T_B < T_{control}$, meaning that the heat exchanged is negative for the pavement, i.e., the air flow is harvesting heat.

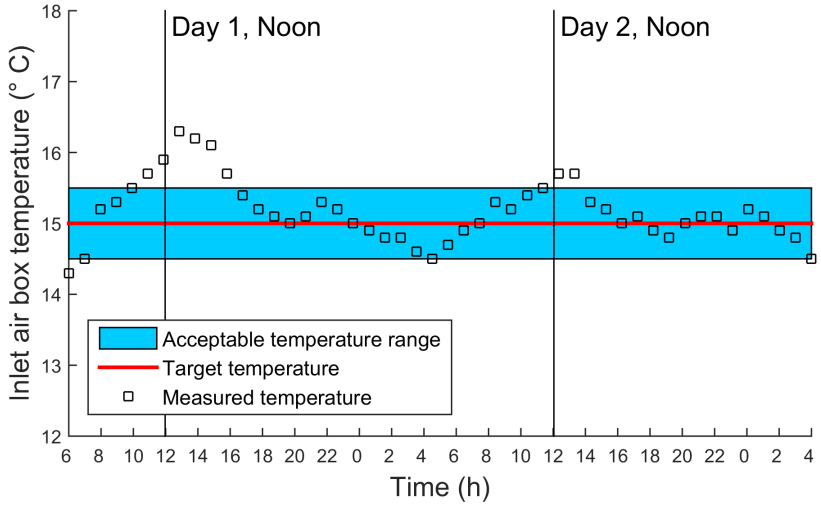

Figure 5.8: Variation of the inlet air temperature for 48 consecutive hours (September 2015).

5.3.2 Results of the experimental trials and discussion

In the next sections, an analysis of the results obtained in the experimental trials in the environment of Nottingham, UK, is presented. The analysis provided further understanding of the phenomena at work and insight for future developments of the technology (see Section 8.2).

Effectiveness of the experimental setup and weather conditions

The very first step in the analysis of the results was to verify if the experimental setup would behave as expected in terms of the set inlet temperature (15°C, as seen in Section 5.3). This was successfully done in Chiarelli et al. (2016) for a short period of time, however, data from longer experimental trials (see Section 5.3) can be regarded as more reliable. In order to check the effectiveness of the temperature control mechanism, the experimental data can be plotted as done in Fig. 5.8 for 48 consecutive hours. It can be observed that the temperature in the inlet air box stays within an acceptable range around the target temperature (T_{set}±0.5°C) for most of the time. However, during peak condi-

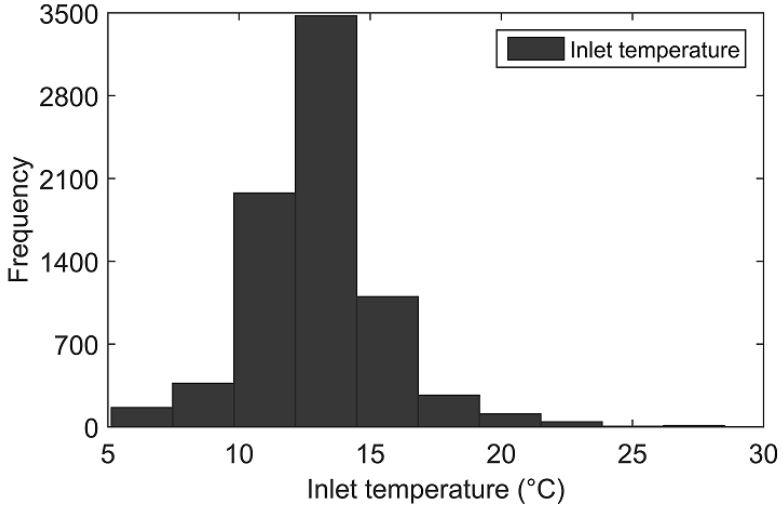

Figure 5.9: Histogram of the inlet temperature in the ground source heat simulator.

tions, the temperature in the inlet air box could not be controlled fully. The reasons for this are that:

- when environmental air is very cold, the ceramic heat emitters aren't always powerful enough to meet the target temperature;
- when environmental air is very warm, there is no way for the GSHS to cool it down (see Section 5.1) and, thus, the target temperature can be exceeded.

In Fig. 5.9, a histogram of the inlet temperatures measured during the whole period of analysis is shown. The data shown in the histogram confirms that the GSHS was able to simulate a controlled inlet temperature around the set value of 15°C, which is in accordance with the results seen in Fig. 5.8 for a shorter period of time. Nevertheless, temperatures between 10°C and about 13°C were also quite frequent, due to the fact that during winter the very cold ambient air would cool down the inlet air box and reduce the effectiveness of temperature control. It is worth noticing that this phenomenon is also seen in Fig. 5.8, however, for a very low number of data points.

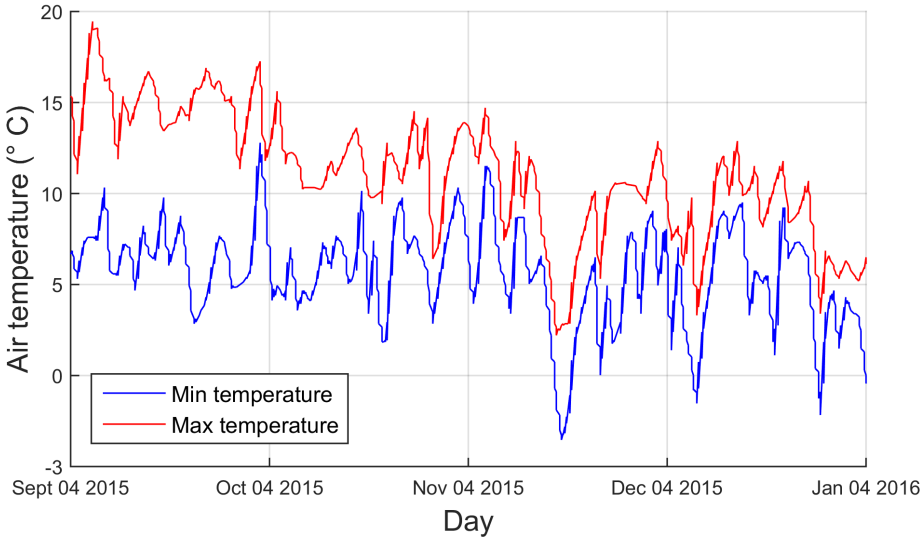

Figure 5.10: Variation of the daily air temperature during the experimental campaign.

The variability of the inlet temperature is not a cause of concern for these trials, as in a real scenario it would not be expected to be exactly constant. In addition, since the environmental air temperatures measured ranged between about 19 °C and -2 °C (see Fig. 5.10), it would be unrealistic to expect a perfect regulation of the inlet temperature, unless impractical amounts of thermal insulation were to be installed around the inlet air box.

The highest environmental temperature was recorded during the month of September 2015, while the lowest was recorded during a very cold week in November 2015. Based on historical observations in Nottingham, UK, the maximum temperature measured was slightly higher and the minimum temperature was rather lower than the corresponding values for the climate period 1981-2010 (see Met Office (UK) (n.d.)). The temperatures measured, however, are reliable, as they are similar to the maximum and minimum temperatures reported for the period of the investigation, as seen on Weather Online (2015-2016) for the location of interest. It is important to specify that these temperatures are not the surface temperatures of the asphalt slab, as those are also

influenced by thermal convection, heat accumulation, and thermal radiation.

During the period of the analysis, an absolute pressure of 1017 Pa to 1020 Pa was measured, while the relative humidity varied considerably in the range 30-100%.

Temperatures measured

During the experimental trials at the University of Nottingham, UK, the GSHS was able to provide the expected temperature management features (heating and cooling of the material) to the energy harvesting pavement prototype. In particular, two scenarios could be observed:

- Scenario 1: ambient temperature higher than inlet temperature during daytime (15°C);
- Scenario 2: ambient temperature lower than inlet temperature (15°C).

The situation described as Scenario 1 corresponds to September 2015, when the temperature was rather high during daytime, but it dropped to low values in the night. Both the pavement prototype and the control slab were influenced by the daily changes in the ambient temperature, however, in Scenario 1, the pavement prototype was always colder than the control slab during the day and warmer in the night. This behaviour can be seen in Fig. 5.11, where the surface temperature of the asphalt slabs are shown for two sample days. On the other hand, Scenario 2 was characterised by environmental temperatures typical of winter and by a surface temperature of the pavement prototype higher than that of the control slab at all times. This phenomenon is shown in Fig. 5.12, where two sample winter days are represented.

The presence of these two scenarios suggests that the GSHS made the pavement work in two modes, i.e.:

- as an energy source, in both Scenarios;

- as an energy harvesting system, in Scenario 1 during daytime.

In Scenario 1, the mode of operation changed with the daily oscillations of the ambient temperature, while, in Scenario 2, it did not change and the system acted as an energy source at all times. In addition to Scenarios 1 and 2, a third situation would be observed in a hotter climate. In fact, if the ambient temperature were always higher than the inlet temperature, the system would be harvesting energy at all times. As can be observed in Table 5.5, the two

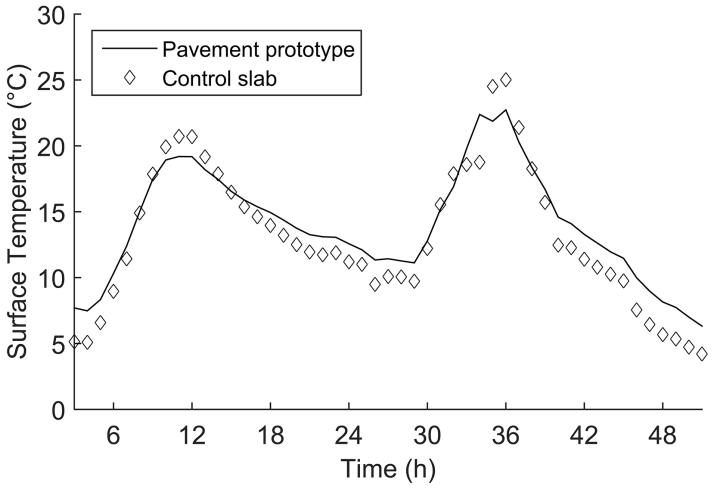

Figure 5.11: Surface temperature evolution of the prototype pavement and the control slab during two days in Scenario 1.

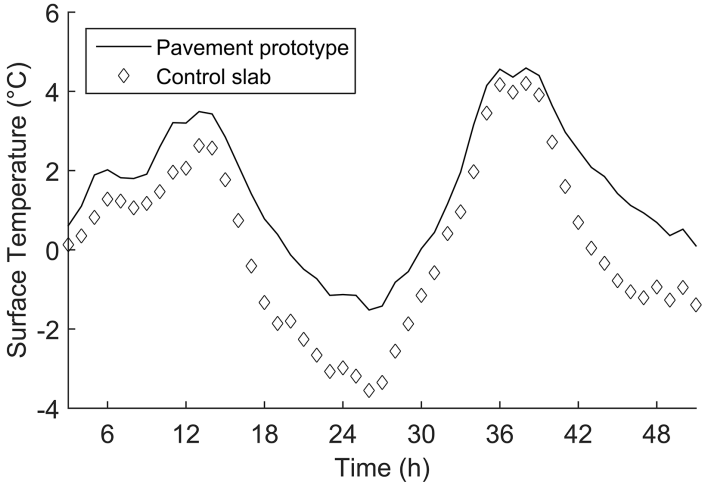

Figure 5.12: Surface temperature evolution of the prototype pavement and the control slab during two days in Scenario 2.

Table 5.5: Pearson's correlation, r, between weather conditions and surface temperature of the prototype pavement (T_B). *=strong correlation, **=moderate correlation.

	T_B Energy harvesting	T_B Energy release
Outdoor Temperature	+0.28	+0.88*
Wind Speed	-0.50**	+0.03
Gust	-0.52**	+0.04
Dew Point	+0.46**	+0.63**
Wind chill corrected temperature	+0.33	+0.87*
24 Hour antecedent Rainfall	+0.55**	-0.25

modes of operation had different correlations with the environmental conditions measured. It is relevant to point out that some of the parameters gathered in Table 5.1 are not present in Table 5.5. The reason for this is that some parameters did not have significant correlations with the surface temperatures measured, thus, their correlation coefficients are not shown. The data gathered in Table 5.5 shows that the flow of pre-heated air through the pavement prototype had measurable effects.

To begin with, the observation of the correlation coefficients for the energy harvesting mode of operation suggests that no strong correlation exists in this situation. This means that the energy harvesting process along with the simulated geothermal source was able to partially uncouple the prototype surface temperature from the environmental conditions. In particular, the data gathered in Table 5.5 shows that the surface temperature of the pavement prototype was not influenced much by the outdoor temperature, but it had a moderate correlation with the wind speed (r=-0.50), gust (r=-0.52), dew point (r=+0.46), and 24 hours antecedent rainfall (r=+0.55).

During energy harvesting, wind caused the surface temperature to decrease (r=-0.50 for wind speed, r=-0.52 for gust), which is in accordance with the re-

port of Liu & Harris (2013). The negative linear correlation between the surface temperature and the wind speed and gust is related to the fact that a higher wind intensity increases the heat exchange between ambient air and the warm surface, thus removing energy from the asphalt slab. It is important to keep in mind that while this is highly beneficial for the reduction of the pavement temperature, heat removal means that less energy is available for harvesting. As a result, the presence of wind and/or gust is a drawback if transferring energy to the air flowing through the pipes is required.

In the case of the dew point, its correlation with the surface temperature comes from meteorology. In fact, a higher dew point is generally related to higher ambient air temperatures, while a lower dew point corresponds to colder periods. The Pearson's correlation coefficient between the atmospheric air temperature and the dew point for the whole dataset (including both modes of operation) was calculated as r=+0.72, which suggests that the surface temperature of the pavement prototype is influenced by the temperature of environmental air. This, however, did not happen in the energy harvesting mode of operation because the air in the pipes acted as a damper and mitigated the potential temperature increase that would normally be associated with a higher atmospheric air temperature.

Finally, a moderate positive linear correlation was found between the surface temperature of the pavement prototype and the 24h antecedent rainfall. This was unexpected, because usually water on a warm or hot surface is expected to reduce its temperature by absorbing energy to power evaporation. However, in the case of the energy harvesting pavement under analysis, it is likely that the temperature reduction effect related to evaporation was overcome by the increase in the thermal mass caused by the presence of rainwater. In fact, the thermal mass of water in the pores and asphalt is higher than that of

air in the pores and asphalt. The reason why the enthalpy of evaporation was overcome by the increase in the thermal mass is that the pavement temperature was never very high nor did it stay high for long periods of time. As a result of an increased thermal mass, the pavement had a higher thermal inertia, thus, it was able to retain its temperature for a longer time as expressed by the first law of thermodynamics (see Bejan (2013)), where the thermal inertia appears in the form of the volumetric heat capacity (i.e., specific heat capacity times density). It is also relevant to mention that, due to the rather high humidity that was measured, air was often close to vapour saturation, which makes evaporation less achievable and slower.

In the energy source mode of operation, the correlations between the parameters considered in Table 5.5 and the surface temperature of the pavement prototype were very different. In this case, the surface temperature was mostly influenced by the temperature of the atmospheric air (r=+0.88) and the wind chill corrected temperature (r=+0.87). The correlation with the dew point is discussed above and the same ideas apply in this mode of operation, too.

The correlations between surface temperature and both outdoor air temperature and wind chill corrected temperature are similar because these weather parameters are tightly related to each other. As reported by Bluestein (2015), the wind chill corrected temperature is defined as the decrease in the air temperature felt by the human body due to air flow and it is similar to the temperature of the atmospheric air when the wind speed is low. In the experimental trials performed at the University of Nottingham, rather low wind speeds were recorded (see Fig. 5.13), thus, the similar correlations are easily explained.

In the case of energy release from the air in the pipes to the pavement, the surface temperature depends quite strongly on the temperature of the atmospheric air. The reason for this is that the air in the pipes cannot provide

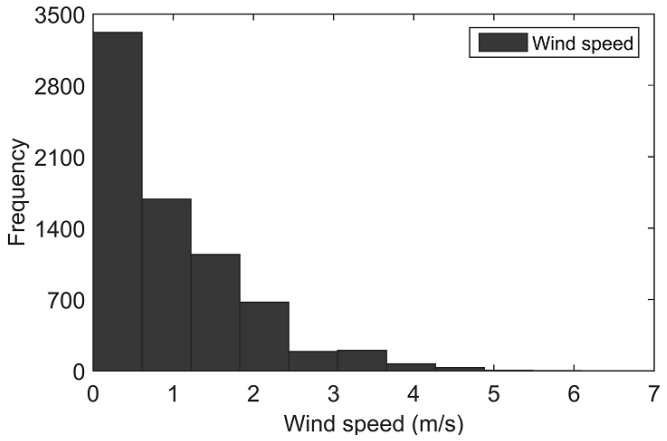

Figure 5.13: Histogram of the wind speed during the experimental campaign.

damping against the environmental conditions due to the fact that the outdoor temperature is lower than the inlet temperature at all times. Therefore, the warmed-up air coming from the simulated geothermal source was not able to counter the cooling effect caused and maintained by the very cold environment and, thus, the pavement was not uncoupled from the atmospheric conditions.

Furthermore, neither wind nor gust were able to influence the pavement temperature during the energy release mode of operation. This happened because, in the conditions of Scenario 2, there was a temperature gradient from the air in the pipes to the pavement surface, thus, implying that only a very small amount of heat could be removed by thermal convection on the asphalt surface. This effect was strengthened by the fact that, due to the stratification of air based on density, the coldest share of ambient air was in contact with the pavement, thus, contributing to a lower surface temperature.

Finally, the sign of the correlation coefficient between the prototype surface temperature and the 24h antecedent rainfall changes between the energy harvesting (r=+0.55) and energy release modes of operation (r=-0.25). The reason for the change in the sign of this coefficient is that during parts of Scenario 1 and Scenario 2, and generally during cold periods, air is drier than in hot periods. As a result, if water is accumulated on the asphalt surface it is more likely

to evaporate. As mentioned above, water evaporation needs heat to happen, thus, energy is removed from the pavement. Consequently, as reported by Tarleton (2006), it is likely that a higher amount of rainfall will cause a reduction of the surface temperature. This effect, however, was not very significant in the experimental trials performed in the context of the present study, as the value of the correlation coefficient for the case of energy release is rather low.

In conclusion, it can be observed that the air in the pipes buried under the pavement and coupled with the (simulated) geothermal heat source was able to mitigate the oscillations in the pavement temperature with varying weather conditions. The extent of the mitigation is quantified in the next section in the case of the experimental setup considered here. However, it is recommended that further studies with no thermal insulation and larger pavement surfaces are performed in order to develop more practical criteria for design.

Energy exchanged

Based on Eq. 5.3.1, it is clear that positive or negative values can be obtained for the energy exchanged between the prototype pavement and the air in the pipes. The sign of the heat exchanged describes its direction, which could also be inferred by the observation of Fig. 5.11 and 5.12. In fact, when the temperature of the prototype pavement is higher than that of the control slab the mode of operation is energy release, while, in the opposite case, the air in the pipes is harvesting energy. It is relevant to mention that the sign of the heat exchanged changes only in Scenario 1, when the curves in Fig. 5.11 intersect, while, in Scenario 2, the energy always flows towards the prototype pavement.

If the energy exchanged is calculated for all 7500 data points and then sorted in ascending order (see Fig. 5.14) what is said above can be clearly appreciated. In Fig. 5.14, it can be observed that the highest portion of the horizontal axis

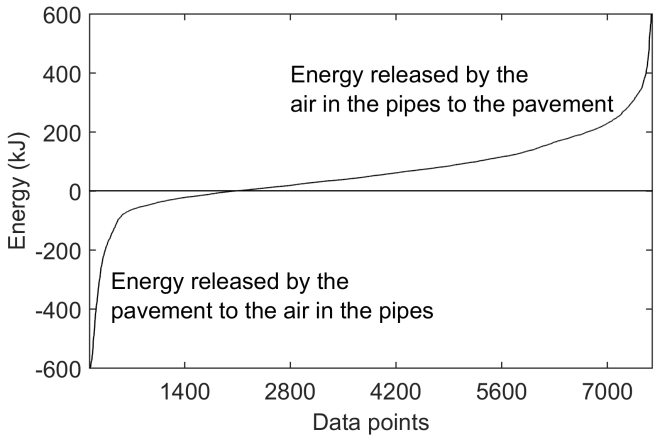

Figure 5.14: Energy absorbed and released by the prototype pavement according to Eq. 5.3.1.

is occupied by positive values of energy, meaning that for most of the time the pavement received energy from the air in the pipes. The reason for this is that the largest part of the experimental trials took place in the coldest part of the year, thus, the pavement most often needed energy rather than containing harvestable heat. Therefore, the fact that the curve appears unbalanced towards the energy release mode of operation should not be seen as a negative aspect, but only as a consequence of the time frame considered for the field study. In fact, if a whole year had been considered, the curve in Fig. 5.14 would be likely to be more balanced, with a similar amount of data points for the two modes of operation considered. Generally speaking, it is also likely that the scale of the vertical axis would change based on the climate, as the maximum and minimum temperatures measured and used in Eq. 5.3.1 would change.

Furthermore, the analysis of the slope of the curve plotted in Fig. 5.14 shows that the number of data points with a corresponding energy exchange higher than about 220 kJ or lower than about -220 kJ was rather low. This can be understood considering the left and right ends of the graph (x <500 and x >7000), where the temperature difference between the prototype pavement and the control slab was higher than 2 °C and up to 5 °C. Such conditions were far from

average and were observed only with very high or very low ambient temperatures. Based on the values of energy seen in Fig. 5.14 and on the data gathered it can be observed that the average temperature difference was between -2 °C and +2 °C. This range of temperature differences is high enough for such a small installation, however, it is essential for further studies to evaluate if the benefits obtained through the use of the technology are high enough to justify the cost and materials required to build and maintain the prototype pavement.

Finally, the maximum and minimum values of energy seen in Fig. 5.14 (about $\pm$600 kJ) correspond to temperature differences of about $\pm$5.5°C between the prototype pavement and the control slab, which are in agreement with the results of the laboratory trials (see Chiarelli et al. (2015*b*)). The maximum and minimum values of the energy exchanged seen in Fig. 5.14 are larger than those reported in Section 4.4. Multiple reasons caused this mismatch, as the data in Section 4.4 was (i) about another prototype pavement, (ii) measured in steady state conditions at equilibrium with the environment, and (iii) calculated with a different approach. Nevertheless, the maximum temperature differences match, thus, confirming the reliability of the experimental results.

Air speed at the chimney outlet

The thermal mass flow sensor mentioned in Table 5.1 and positioned at the outlet of the chimney (see point E in Fig. 5.4) was used to monitor the air speed during the experimental trials. The values of air speed measured ranged between 0 m/s and 0.3 m/s, which means that the performance in terms of outlet speed was quite low and generally lower than in the laboratory trials.

The statistical analysis of the results showed that the outlet air speed is related to the surface temperature but that this link is rather weak (r=0.4). A further analysis of the data, however, could uncover a hidden explanation

for such a low correlation coefficient. In fact, if the two modes of operation described above (energy release and energy harvesting) are considered, it is possible to calculate new correlation coefficients based on this subdivision. In particular, the correlation coefficient during energy harvesting is as high as r=0.73, which means that there exists a strong and positive relationship linking the prototype surface temperature to the outlet speed. In this case, the air speed ranged between 0.08 m/s and 0.30 m/s. Moreover, in the energy harvesting mode of operation, a moderate negative correlation (r=-0.53) was found linking the outlet air speed with the wind speed. This phenomenon is easily explained, as a higher wind speed increases the surface cooling effect on the pavement, thus, reducing the energy available for harvesting and, therefore, the outlet air speed, which is a function of the air density.

On the other hand, in the energy release mode of operation, the air speed at the chimney outlet was very low and in the range 0-0.08 m/s, which corresponds to a very slow air flow due to natural convection and caused by the heat left in the air after releasing energy to the pavement.

Finally, it is relevant to mention that, in the context of these experimental trials, the effect of the roof installed over the chimney outlet to prevent water infiltration (see Fig. 5.4 and 5.7) was not studied. It is expected that this aspect could be somewhat optimised, as the outlet velocity profile depends on the shape and orientation of the opening that is allowed.

CHAPTER 6

Modelling convection-powered energy harvesting

6.1 One-dimensional thermal modelling

The results shown in the previous chapters strongly suggest that the behaviour of buoyancy-powered flows is influenced by both thermodynamics and fluid dynamics. However, as a part of this Thesis, an attempt at modelling the system by considering only thermodynamics was made. This approach was pursued because it is more simply implemented, thus, it could potentially be available to a wider number of researchers and practitioners. All the equations and ideas presented in this section are adapted from the discussions seen in Chiarelli et al. (2015*a*) and Chiarelli et al. (2015*b*).

Keeping in mind that the main aim of this part of the research was to test the simplest possible modelling approach, it was decided to perform a one-dimensional (1D) analysis. Therefore, the original prototype described in this Thesis (see fig. 3.1) was simplified as a 1D domain, as shown in Fig. 6.1. This was done because a parametric experimental study had been carried out on this prototype, thus, numerous data points were available for comparison with

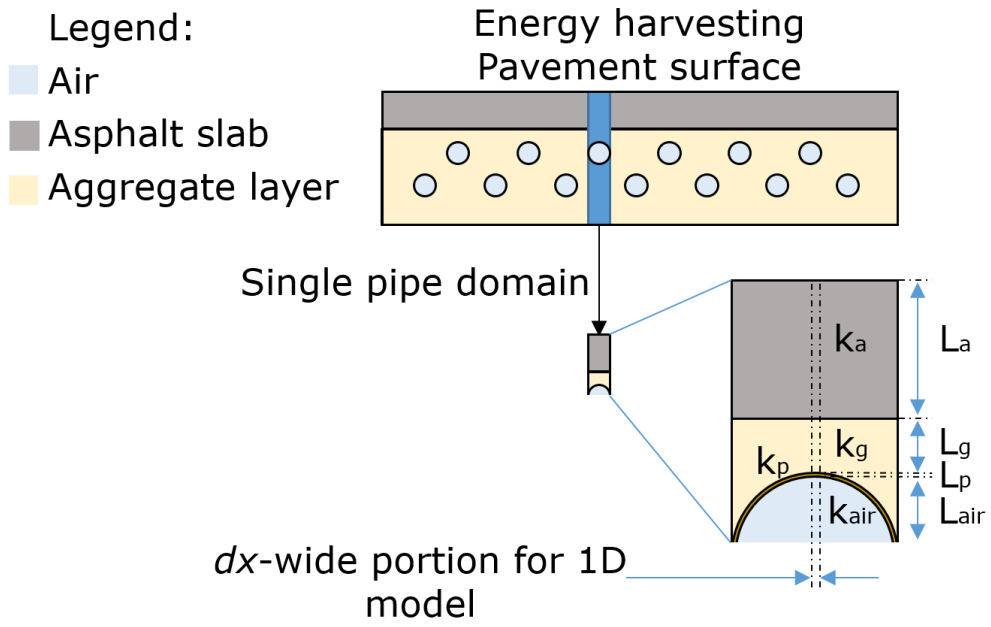

Figure 6.1: Simplification of the domain for the 1D thermodynamic model and subscripts used in the equations (prototype from Chapter 3).

the results obtained through modelling.

For the purposes of the analysis 13 separated sections were considered, each made of an asphalt layer, an aggregate layer, and a pipe. The pipe wall shown in Fig. 6.1 was considered as a solid part, thus, two boundaries exist, i.e., $p,\ ext$ and $p,\ int$, representing the external and internal walls of the pipe, respectively. Furthermore, only a dx wide portion of the domain of interest seen in Fig. 6.1 was considered. Therefore, even if the pipe has a curved wall it is here considered as a horizontal slab for simplification purposes.

Owing to the simplifications introduced above and under the hypothesis of no heat losses or heat accumulation, it is possible to apply Fourier's law to the domain of interest:

$$\begin{cases} q''_{max} = k_a \cdot (T_a - T_g)/L_a \\ k_a \cdot (T_a - T_g)/L_a = k_g \cdot (T_g - T_p^{ext})/L_g \\ k_g \cdot (T_g - T_p^{ext})/L_g = k_p \cdot (T_p^{ext} - T_p^{int})/L_p \end{cases} \tag{6.1.1}$$

where the subscript a refers to the asphalt layer, the subscript g refers to the aggregate layer, and the subscript p refers to the pipes, as shown in Fig. 6.1. Moreover, k and L are the thermal conductivity and the thickness of the layers, respectively. The values of thermal conductivity and thickness are shown in Table 6.1, along with all the parameters that will be introduced in this section from this point onwards. Based on Eq. 2.3.3, the temperature of air flowing in the pipes installed beneath the pavement surface can be calculated by rearranging the following equation:

$$q_{max} = h_{p-air} \cdot A_p \cdot (T_p^{int} - T_{av,air}) \tag{6.1.2}$$

where h_{p-air} is the convective heat transfer coefficient between the pipe wall and air, A_p is the internal surface of the pipes, and $T_{av,air}$ is the average temperature of the air flowing in the pipes. However, Eq. 6.1.2 cannot be used in the case of the prototype described in this chapter, because h_{p-air} is a function of the speed of air in the pipes, which was not measured. Therefore, a simplification was made to allow the application of this 1D model, i.e., the equation for thermal conduction was used to calculate $T_{av,air}$ in the place of Eq. 6.1.2, which describes thermal convection. This simplification was deemed reasonable due to the very low values of speed that were measured at the system outlet, which suggest that the speed inside the pipes will be reasonably lower than 0.5 m/s. As a result, the equation of thermal conduction was used to provide an approximate estimation of a temperature that is, instead, the result of thermal convection:

$$k_p \cdot (T_p^{ext} - T_p^{int})/L_p = k_{air} \cdot (T_p^{int} - T_{av,air})/L_{air} \tag{6.1.3}$$

where L_{air} is equal to the internal radius of a pipe.

In order to validate this hypothesis, it was decided to use the equations described so far to calculate the chimney temperature and to compare it to the

Table 6.1: Constants used for the model developed (see Fig. 6.1).

Symbol	Value	Unit	Source
k_a	1.2	W/(m K)	Stempihar et al. (2012)
k_g	0.55	W/(m K)	Kömle et al. (2007)
k_p	~ 15 ($\sim 50^o$ C)	W/(m K)	Assael et al. (2004)
k_{air}	0.02785 ($\sim 50^o$ C)	W/(m K)	Haynes (2012)
L_a	0.05	m	
$L_{top\ layer}$	0.015	m	
$L_{bottom\ layer}$	0.115	m	
L_p	0.001	m	
L_{air}	0.015	m	

values obtained experimentally. To do so, additional equations were added under the assumption that the system does not suffer any heat loss in the air box or throughout the chimney.

The first step for the calculation of the temperature at the system outlet was the evaluation of $T_{av,air}$ for all the pipes by the means of Eq. 6.1.3. Of course, the value of L_g used in Eq. 6.1.3 depended on whether the pipe considered was in the top or in the bottom row in the prototype. From this point onwards, the top row will be addressed with the subscript t, while the subscript b will be used for the bottom row. Thus, $T_{av,air}$ will be replaced by T_t or T_b based on the layer under consideration. Knowing the average air temperature in the pipes, it is possible to calculate the equilibrium temperature in the air box using the principle of energy conservation:

$$m_b^{tot} \cdot c_{p,air} \cdot (T_{eq} - T_b) = m_t^{tot} \cdot c_{p,air} \cdot (T_{eq} - T_t) \tag{6.1.4}$$

where m_b^{tot} is the total mass of air in the bottom layer of pipes, m_t^{tot} is the total mass of air in the top layer of pipes, T_{eq} is the equilibrium temperature in the air box, and $c_{p,air}$ is the specific heat capacity of air. The use of Eq. 6.1.4 implies the air from the 13 pipes considered mixes adiabatically (with no heat losses) in the

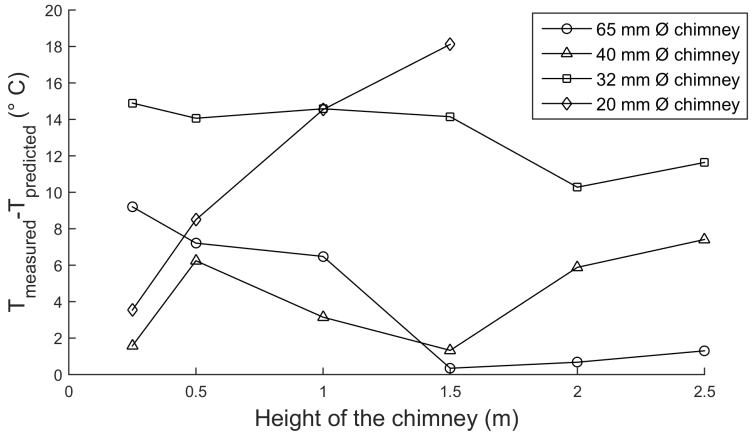

Figure 6.2: Difference between measured chimney temperatures (T_E) and predicted values (T_{eq}).

air box. The specific heat capacity used in the energy balance was considered as constant, as it does not vary significantly in the temperature and pressure range considered in this study.

The last missing input parameter of Eq. 6.1.4 is the mass of air in each pipe and it was calculated as

$$m_{air}^{pipe} = \rho_{air} \cdot V_{air} \tag{6.1.5}$$

where ρ_{air} is calculated with the ideal gas law at the relevant $T_{av,air}$ and V_{air} is the volume of a pipe. As a result, the combination of Eq. 6.1.4 and Eq. 6.1.5 yields:

$$T_{eq} = \frac{7 \cdot m_b^{pipe} \cdot T_b - 6 \cdot m_t^{pipe} \cdot T_t}{7 \cdot m_b^{pipe} - 6 \cdot m_t^{pipe}} \tag{6.1.6}$$

which, under the assumption of no heat losses, will be equal to the temperature at the chimney outlet.

The process described so far can be followed to try and approximate the outlet temperature for all cases considered in the parametric analysis mentioned above and the difference with the measured values can be calculated. The observation of the values shown in Fig. 6.2 clearly suggests that the results obtained using the 1D thermodynamic approach can be considered as an

approximation only when the chimney diameter is above 40 mm. This means that it is very likely that if the diameter is decreased fluid dynamics will play a more important role (specifically frictional losses between air flow and conduit walls) and that a thermodynamic model alone will not be fit to describe the phenomena at work. As a result, computational fluid dynamics (CFD) should be considered to deal with the prediction of the experimental results and to provide a better estimation of the actual performance of the system.

Finally, it is important to keep in mind that even if the temperature at the chimney outlet cannot always be estimated with the method described in this section, the temperature in other locations inside the prototype can be estimated quite precisely with a 1D model. As an example, the values of T_C and T_D (see Fig. 3.2) can be estimated with a relative error between 0.004% and 8%.

6.2 Computational fluid dynamics and energy harvesting pavements

The equations considered in Section 6.1 apply only to a 1D domain and they describe the thermodynamic phenomena that happen in a given energy harvesting pavement prototype. Therefore, they are not fit to fully describe the behaviour of convection-powered energy harvesting pavements when fluid flow is taken into account. Moreover, the equations listed in Section 6.1 were found to be too inaccurate for the purposes of design, as their results are often too approximate.

This means that new and more complex equations should be used to describe the physics of an energy harvesting pavement and that a different approach to their solution must be introduced as well. In fact, 1D equations can be solved easily with a spreadsheet, however, 3D fluid-dynamics require more

Table 6.2: Variables used in Eq. 6.2.1 and 6.2.2.

Variable	Physical meaning	Unit
ρ	density of fluid (air) in the system	kg/m^3
c_p	specific heat capacity	$J/(kg\,K)$
T	temperature	K
t	time	s
u	velocity in x-direction	m/s
v	velocity in y-direction	m/s
w	velocity in z-direction	m/s
k	thermal conductivity	$W/(m\,K)$
q_v	heat source	W/m^3
g_x	gravitational acceleration in x direction	m/s^2
μ	dynamic viscosity	$kg/(m\,s)$

advanced numerical solutions..

The description of the relevant physical phenomena for computational fluid-dynamics (CFD) simulations can be performed combining the Navier-Stokes equations, the First Law of Thermodynamics, and the law of mass conservation. As a result, momentum, energy, and continuity in the system are considered. To begin with, as reported by White (2002), the momentum equation for the x direction is:

$$\rho\frac{\partial u}{\partial t}+\rho u\frac{\partial u}{\partial x}+\rho v\frac{\partial u}{\partial y}+\rho w\frac{\partial u}{\partial z}=\rho g_x-\frac{\partial p}{\partial x}+\frac{\partial}{\partial x}\left[2\mu\frac{\partial u}{\partial x}\right]+ \\ \frac{\partial}{\partial y}\left[\mu\left(\frac{\partial u}{\partial y}+\frac{\partial v}{\partial x}\right)\right]+\frac{\partial}{\partial z}\left[\mu\left(\frac{\partial u}{\partial z}+\frac{\partial w}{\partial x}\right)\right] \tag{6.2.1}$$

The formulation of Eq. 6.2.1 for the y and z directions can be adapted easily by substitution of the variables of interest. All the variables used in Eq. 6.2.1 and in the following Eq. 6.2.2 and Eq. 6.2.3 are listed in Table 6.2. Due to the fact that buoyancy causes the air flow in convection-powered energy harvesting pavements, the gravity term in Eq. 6.2.1, ρg_x, is expected to dominate the flow.

Furthermore, the First Law of Thermodynamics (also known as the energy

equation, see White (2002)) can be expressed as:

$$\rho c_p \frac{\partial T}{\partial t} + \rho c_p u \frac{\partial T}{\partial x} + \rho c_p v \frac{\partial T}{\partial y} + \rho c_p w \frac{\partial T}{\partial z} = \frac{\partial}{\partial x}\left[k \frac{\partial T}{\partial x}\right] + \frac{\partial}{\partial y}\left[k \frac{\partial T}{\partial y}\right] + \frac{\partial}{\partial z}\left[k \frac{\partial T}{\partial z}\right] + q_v \tag{6.2.2}$$

Finally, the continuity equation (see White (2002)) can be written as:

$$\frac{\partial \rho}{\partial t} + \frac{\partial \rho u}{\partial x} + \frac{\partial \rho v}{\partial y} + \frac{\partial \rho w}{\partial z} = 0 \tag{6.2.3}$$

Since in this Thesis steady-state conditions are studied, the time-dependent terms in Eq. 6.2.1, 6.2.2, and 6.2.3 are neglected (i.e., all the terms with ∂t in the denominator). In addition, since there are neither volumetric heat generation nor heat sinks within the energy harvesting pavement, q_v can be neglected, too.

Finally, since the air flow is ruled by density differences, this parameter needs to change based on the physical state of air. This can be implemented using either Boussinesq's approximation (see, e.g., Quéré et al. (2005), George (n.d.), or Lee & Kim (2011)) or the low Mach number assumption (see, e.g., Quéré et al. (2005) or Medale & Haddad (2012)). In this Thesis, the low Mach number assumption is used, therefore, the pressure in Eq. 6.2.1 is replaced with:

$$p = P_{ref} + \rho_\infty g_i x_i + p^* \tag{6.2.4}$$

where P_{ref} is the atmospheric pressure, ρ_∞ is the density at ambient temperature and pressure, g_i is the gravity vector, and x_i is the distance vector from the origin. Since Eq. 6.2.4 is used, p^* will be the new variable describing pressure in the momentum equations for all directions.

All the equations described in this section can be combined and solved through numerical models to describe the behaviour of convection-powered energy harvesting pavements. Further details on the use of these equation are shown in the next sections.

6.2.1 Testing the CFD approach

The equations described in Section 6.2 need to be implemented in an appropriate software and applied in a 3D model that reproduces an energy harvesting pavement. Since the most complex experimental layout considered in this Thesis is the GSHS (see Section 5.1), it was used to study all the phenomena happening in the system. In the next sections, the details of the implementation are discussed and the results obtained from this case study are used to verify the validity of the approach.

Computational reproduction of temperature modifying pavements

The software chosen to implement the computational solution of the equations listed in Section 6.2 was Autodesk Simulation CFD. The reason for this choice is that other Autodesk products (AutoCAD and Inventor) were used to design the prototypes, thus, allowing for a rather simple workflow when handling the files.

Before starting the simulations, a simplified 3D model of the GSHS was built and meshed, as shown in Fig. 6.3. In the 3D model, the inlet pipe, the inlet air box, and the pavement prototype were represented. It was decided to represent all these components because the system has many sharp turns for the air flow (sharp changes in the dominant air direction), thus, it was expected to see eddies causing pressure drops in the system. In order to solve the set of equations mentioned above, boundary conditions were needed in the setup of the computational solver. It was chosen to use the steady-state temperatures measured by the thermocouples in the laboratory experiments described in Section 5.2 as boundary conditions. This allowed a comparison of the outlet air speed obtained in real and virtual experiments, thus, providing a way to assess the effectiveness of the approach chosen. The temperatures used as boundary

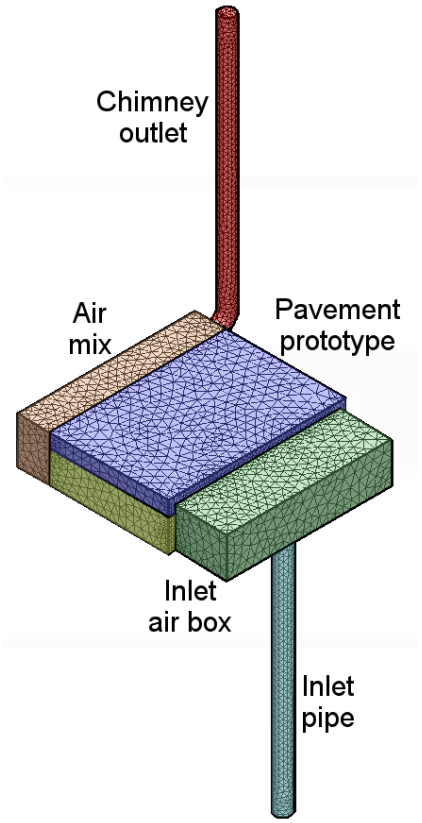

Figure 6.3: Meshed 3D model of the prototype pavement studied.

conditions were the surface temperature in steady state, the temperature set at the inlet, and the environmental temperature at the end of the physical tests. The environmental pressure was set at the inlet and outlet of the system by setting a null gauge pressure. Since in the computational study small variations of the ambient temperature and surface convection were neglected, it is clear that the results of the simulations were not expected to be a perfect match with the the experimental ones, but a good approximation.

It is relevant to mention that, in Autodesk Simulation CFD, the effects of friction were considered by the means of the parameter called roughness height when defining the solid parts of the system. By doing this, the solver applied this property to all the wetted surfaces of the part(s) under consideration (see Autodesk, Inc. (2015)).

The validation of the CFD approach was pursued considering the scenario

corresponding to simulated winter conditions. This choice was made because, in that case, temperature recorded both with and without the chimney outlet were available (in simulated summer conditions, only tests with the chimney were performed, see Section 5.2), thus, a more complete analysis was possible. In addition, for the purposes of the computational setup of the problem, choosing winter or summer conditions would not make a difference, as the boundary conditions used for summer conditions would be selected based on an identical logic.

Validation of the numerical model

The results obtained for the outlet air speed with the CFD simulations are represented in Fig. 6.4a and 6.4b. A quick visual comparison suggests that the CFD models were able to reproduce effectively the experimental results. This can be inferred by the observation of the fitting lines of experimental and computational results, which are very close to one another. The slopes of the fitting lines represented in Fig. 6.4a and 6.4b are 0.0181 m/(s °C) and 0.0219 m/(s °C) for the experimental results with and without chimney, respectively, with goodness of fit of 0.929 and 0.871. The slopes of the fitting lines for the CFD results are 0.0182 m/(s °C) and 0.0224 m/(s °C) for the datasets with and without chimney respectively, with goodness of fit values of 0.936 and 0.873. These results combined with the visual assessment of the figures provide a confirmation of the effectiveness of CFD simulations to describe the physics of the energy harvesting pavement prototype powered by air convection. It is, however, important to keep in mind that the success of computational simulations always depends on the choice of the most appropriate boundary conditions, which, in this case, were based on experimental results that were obtained in the laboratory. It can be observed that the results shown in Fig. 6.4a and 6.4b

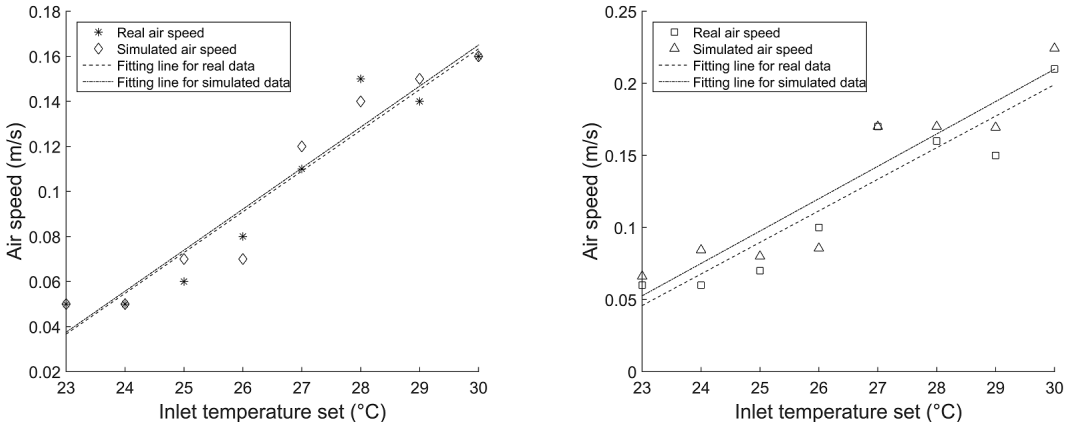

(a) Tests with chimney.

(b) Tests without chimney.

Figure 6.4: Real data vs. computational results (Winter conditions).

are a bit scattered around the fitting lines. The reason for this is closely related to the fact that measured temperatures were used as boundary conditions. In fact, it is expected that using the same surface temperature or incident heat flux and the same ambient temperature for all simulations the results would be less scattered and show a smoother relationship.

In fact, the target of the CFD simulations performed was to match the experimental values of air speed that were measured, which is not the aim that a designer would normally pursue. In the case of the design of an energy harvesting pavement for a real life application, the boundary conditions should be different, i.e., real weather conditions from databases about a specific location should be used. The weather data that should be used in this case include surface temperature, air temperature, and soil temperature at a given depth.

Furthermore, accurate values should be used for the inlet and outlet of the system, because the behaviour of the energy harvesting technology considered is based on buoyancy, which is ruled by density gradients. Finally, for the design of convection-powered energy harvesting pavements, CFD simulations should consider transient conditions and not steady-state as done here. This is because, in a real life scenario, the variation of the environmental conditions

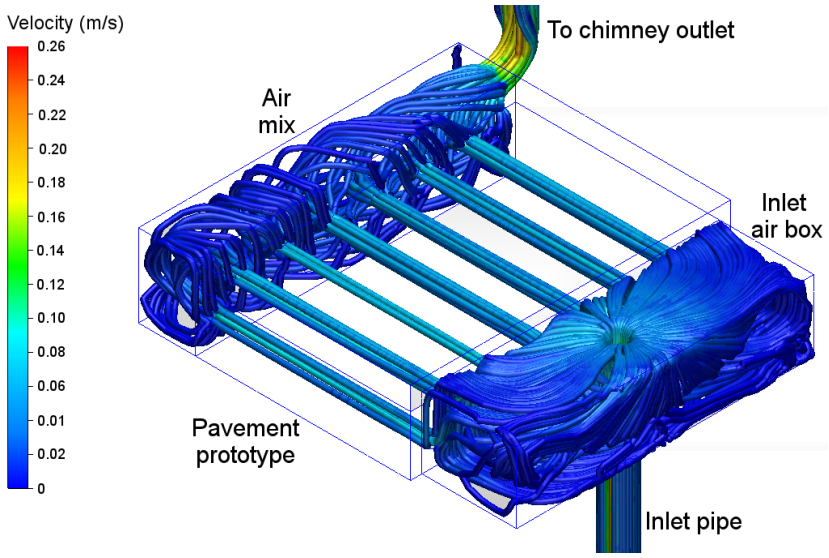

Figure 6.5: Particle traces with velocity magnitude (Winter conditions).

must be considered to fully assess the performance of the system, since their daily oscillation is what determines the gradients that affect the behaviour of the buoyancy-powered air flow.

6.2.2 Predictive use of numerical models

a) Inlet box air flow

Since CFD simulations were shown to be fit to describe air convection in the system, they were also used to (i) look into some aspect of the GSHS that were mentioned in Section 5.2.2 but could not be verified experimentally and (ii) further improve the understanding of the phenomena at work. To begin with, in Section 5.2.2, it was mentioned that there was air stagnation in the inlet air box. This could not be tested experimentally, due to the fact that the GSHS was thoroughly sealed and no physical access was possible in the inlet air box. Therefore, after the CFD simulations were run particle traces were added to graphically see how air moves in the system. In Fig. 6.5, it can be easily seen that the velocity in the inlet air box is very low (almost 0 m/s), because of the geometry of the system. In fact, air coming from the inlet pipe of the GSHS

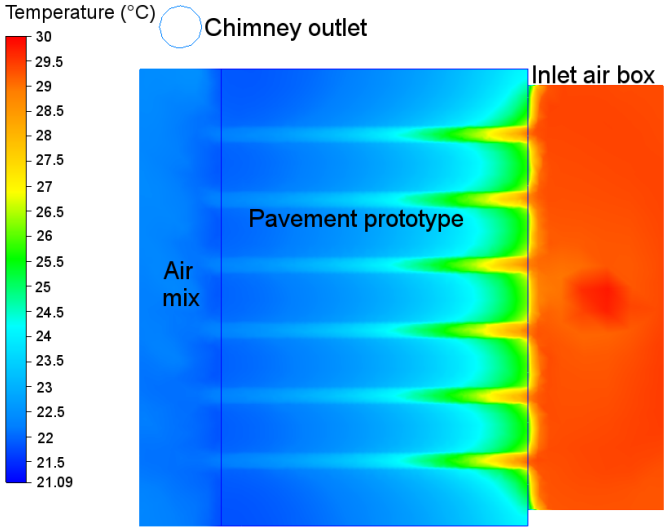

Figure 6.6: Stagnation of air in the inlet air box (Winter conditions).

flows upwards, then it is scattered by the upper wall of the inlet air box, and finally enters the energy harvesting pipes. This causes high head losses and is acceptable for a first study of energy harvesting pavements (i.e., the aim of this Thesis), but such a high energy loss due to friction and eddy effects may not be acceptable for a real life installation. The same phenomenon is seen in the outlet air box, however, its study is more complex and requires further considerations (see Section 6.2.2), as changes in its geometric configuration have strong effects on the outlet air flow. The presence of stagnation can also be observed in Fig. 6.6, where the temperature inside the inlet air box is almost the same as the inlet temperature chosen (30°C, in the case of Fig. 6.6). Air stagnation is also observed in the outlet air box, as the air speed in this volume is approximately the same across the whole cross section represented.

Finally, it is possible to compare the temperature profiles in Fig. 6.6 and 6.7. A visual analysis of Fig. 6.6 suggests that, in simulated winter conditions, the temperature of air in the pipes is highly affected by the inlet temperature chosen up to a certain length, then it decreases because of the release of heat to the pavement. On the other hand, in Fig. 6.7, it can be seen that, in simulated

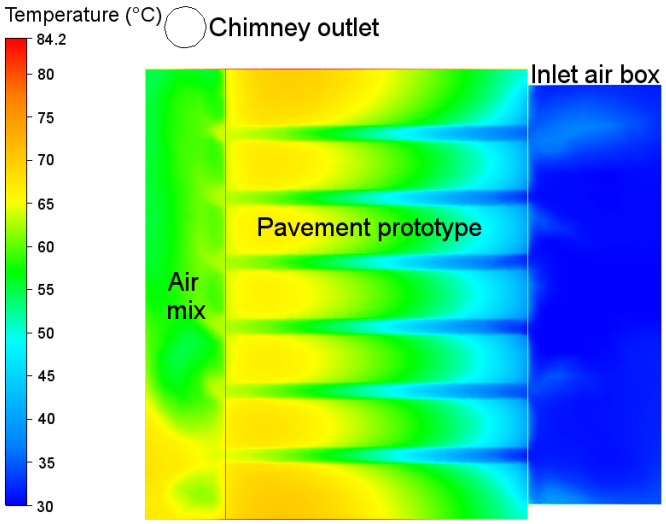

Figure 6.7: Cross section with temperature profile (Summer conditions).

summer conditions, the temperature in the pipes increases throughout the energy harvesting system thanks to heat absorption. In this case, temperature stagnation is mostly limited to the inlet air box, while the temperature in the outlet air box is not as constant. The reason for this is related to the higher air speed that was found in summer conditions, which draws hot air outside the system more effectively.

b) Size and shape of the outlet air box

Since the CFD approach provided satisfactory results for the description of the buoyancy-powered air flow, it was decided to use simulations to evaluate the effect of the size and shape of the (outlet) air box in convection-powered energy harvesting pavements. Such a study was performed because, in previous laboratory experiments (see Chiarelli et al. (2015*b*)), it was found that the air box is able to influence the behaviour of the energy harvesting setup.

The analysis described in this Section is based on the prototype seen in Chapter 4 (configuration corresponding to Test 1, as seen in Table 4.2). The configuration of the prototype chosen for the CFD simulations was picked ar-

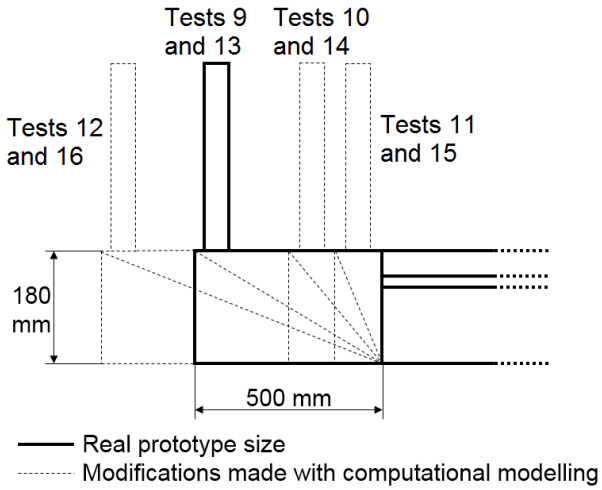

Figure 6.8: Modifications to the air box considered in the CFD simulations.

bitrarily based on the assumption that the pipe arrangement cannot have a very strong effect on the trend of the results if the air box is modified. This is because of the significantly lower amount of air in the pipes compared to the amount held in the air box, which means that the pipe arrangement should influence the temperature obtained in the air box but not the overall behaviour of the system. Therefore, the configuration was fixed based on the assumption that changes to the design of the air box should influence the trends of the results more intensely than changes in the layout of the energy harvesting pipes.

The study of the size and shape of the air box was performed by changing the volume and cross section of the air box as seen in Table 6.3 (the numbers in the table continue from Table 4.2, as they were part of the same study). A graphical explanation of the layouts described in Table 6.3 is shown in Fig. 6.8. In addition, a test where the air box was replaced with a manifold geometry was performed (see Fig. 6.9), in order to assess the effects of a more direct connection between the energy harvesting pipes and the environment.

The boundary conditions fixed in the simulations were a surface temperature of 70°C and environmental conditions at the inlet and outlet of the system. This means that, in this study, thermal convection and radiation on the proto-

Table 6.3: Overview of the CFD simulations performed (V=volume of the air box).

Test number	Objective
9	Real air box volume with rectangular section (V=30.6 dm^3)
10	Air box with 1/2 length and rectangular section (V=15.3 dm^3)
11	Air box with 1/4 length and rectangular section (V=7.65 dm^3)
12	Air box with 1 1/2 length and rectangular section (V=45.9 dm^3)
13	Air box with real length and triangular section (V=15.3 dm^3)
14	Air box with 1/2 length and triangular section (V=7.65 dm^3)
15	Air box with 1/4 length and triangular section (V=3.825 dm^3)
16	Air box with 1 1/2 length and triangular section (V=22.95 dm^3)
17	Manifold geometry (V=0 dm^3, see Fig. 6.9)

type surface were neglected. Such a decision was made because the analysis of these phenomena would require further hypotheses, e.g., the air speed on the pavement surface and the temperature of air, which would make the simulation more complex and would not contribute to the analysis of changes in the geometric configuration of the air box.

Finally, it is relevant to point out that the boundary conditions chosen do not allow for an analysis of the cooling potential related to each configuration of the air box. To achieve this, it would be sufficient to use a surface heat flux as the boundary condition on the pavement surface. The choice of a surface temperature as the boundary condition on the pavement surface was made because of the need to compare all the configurations based on a common parameter. In fact, if a heat flux were set on the pavement surface, it would cause different pavement temperatures related to the changes in the size and shape of the air box, which would not allow an effective comparison.

The results obtained from the CFD simulations described above are shown in Fig. 6.10-6.12. The results are represented as interpolated curves obtained

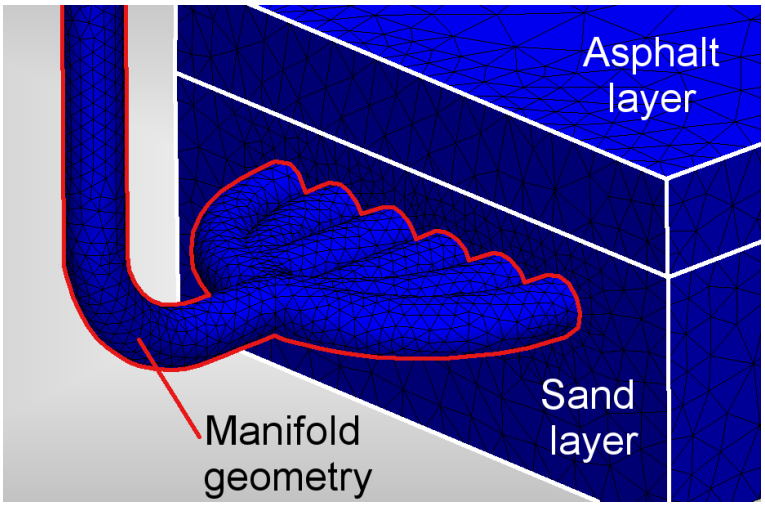

Figure 6.9: Manifold geometry used for test 17.

from the computational simulations.

In Fig. 6.10, it is possible to see the asphalt temperature, the sand temperature, the air box temperature, and the outlet temperature for simulations with a rectangular air box. All the results shown are volume-weighted averages for the subdomain they belong to. With the exception of the asphalt temperature, all the other temperatures increase when the air box volume is increased. Furthermore, the air box temperature and the outlet temperature have very close values with the highest air box volumes considered.

When the air box has a triangular cross section longitudinally, a very similar behaviour is observed. In fact, in Fig. 6.11, it can be seen that all temperatures except for the asphalt temperature increase when the air box volume increases. In particular, the asphalt temperature peaks at an intermediate value of the air box volume, while it decreases towards higher and smaller volumes.

Furthermore, the behaviour of the air speed can be seen in Fig. 6.12. It can be observed that the curves have a peak corresponding to about 0.435 m/s and 0.43 m/s for a rectangular and a triangular cross section of the air box, respectively.

Finally, it is important to point out that the CFD simulations considering

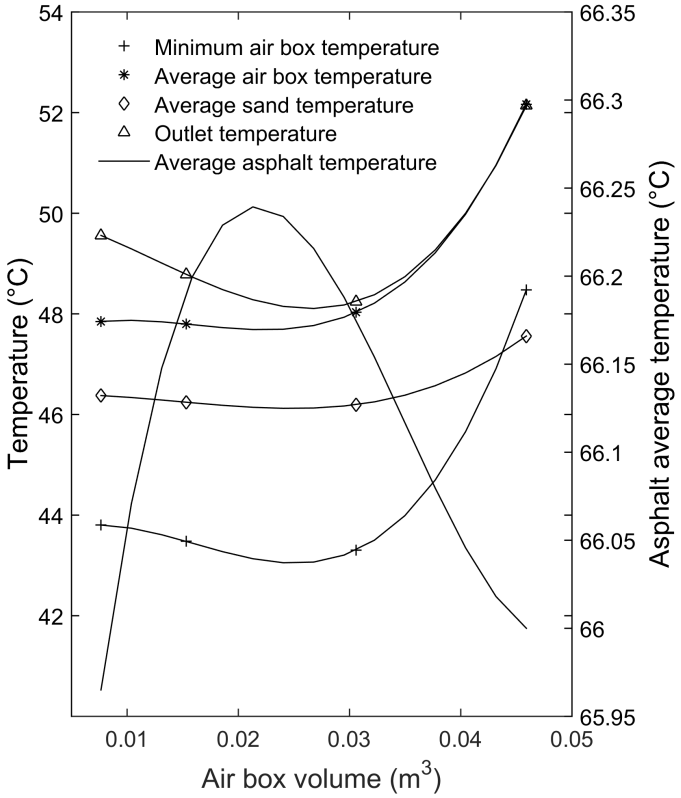

Figure 6.10: Effects of the air box size (rectangular cross section).

a manifold (Test 17) resulted in an average asphalt temperature of 68.8°C, an average sand temperature of 62.2°C, an outlet temperature of 69.2°C, and an outlet air speed of 0.32 m/s. Therefore, the use of a manifold allows air speeds that are similar to those obtained with larger air box volumes, but the pavement cooling potential is reduced.

The outlet air speed obtained with CFD simulations considering the original air box volume (0.435 m/s) is very close to the real value obtained experimentally (0.44 m/s, see Fig. 4.8 and 6.12). This is a further confirmation of the validity of the approach for the simulation of the buoyancy powered air flow under the asphalt pavement. In fact, due to a slightly lower surface temperature set in the CFD tests (70°C) compared to that obtained experimentally in Test 1 (74.5°C, see Section 4.4), a slightly lower outlet air speed was expected in

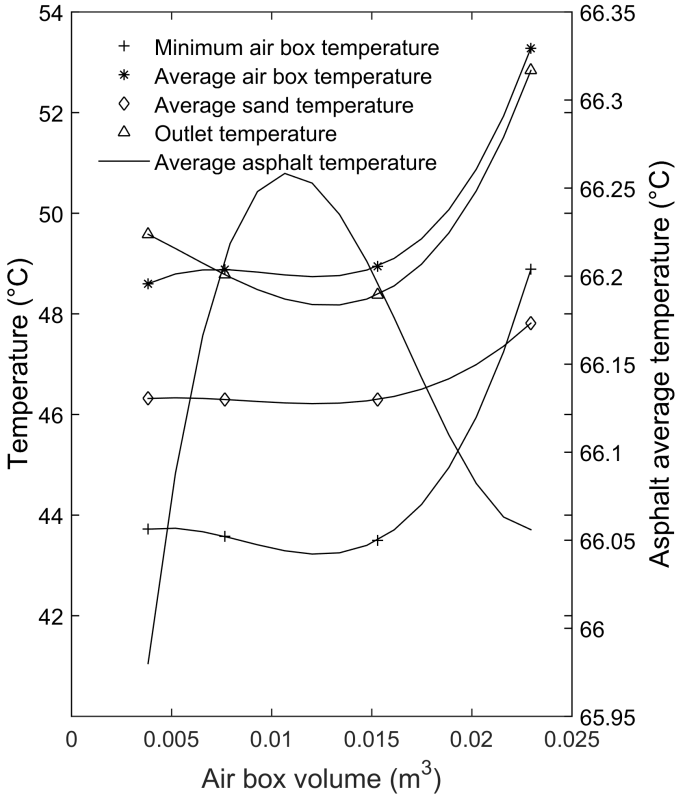

Figure 6.11: Effects of the air box size (triangular cross section).

the former case.

The most important result of the simulations that were run is that the air box was confirmed to have a fundamental role in the design of convection-powered energy harvesting pavements. In fact, when a manifold is used in the place of the air box, the only application for the system is the use of the harvested heat, as a very small pavement cooling effect is achieved.

An analysis of Fig. 6.12 suggests that the maximum values of air speed were obtained for air box volumes in the intervals 0.025-0.030 m^3 and 0.010-0.015 m^3 for a rectangular and a triangular cross section, respectively. If the same intervals are considered in Fig. 6.10 and 6.11, it can be observed that all temperatures except for the asphalt temperature are approximately at their minimum point. In contrast, the asphalt temperature is maximum in the above-mentioned inter-

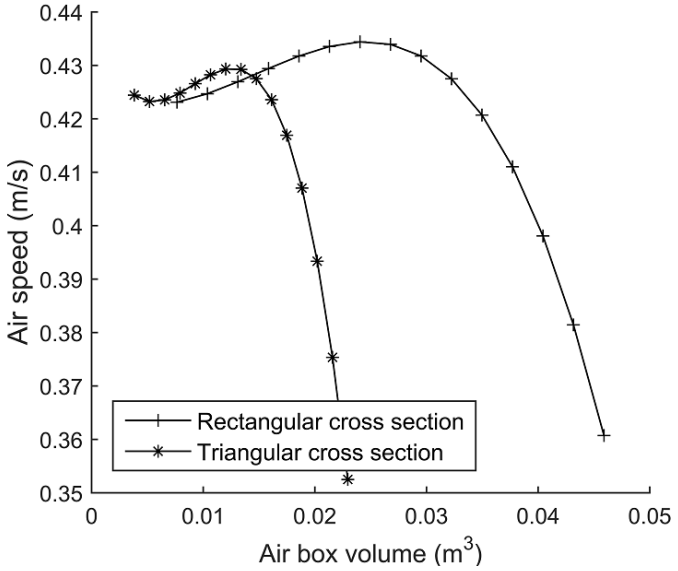

Figure 6.12: Outlet air speed obtained in the CFD simulations.

vals of air box volumes. This means that, in these intervals, the thermal energy available at the chimney outlet is the lowest, because the outlet temperatures represented in Fig. 6.10 and 6.11 are at their minimum points.

Moreover, the outlet temperatures seem to show an increasing trend in Fig. 6.10 and 6.11, which means that even higher air box volumes may lead to higher outlet temperatures. However, based on the analysis of Fig. 6.12, it appears that increases in the air box volume would cause the outlet air speed to decrease to negligible values.

Based on the results obtained in the simulations, it can be concluded that the design of the air box has to be based on the effect that needs to be obtained. If the designer is looking for a high outlet temperature, larger air boxes are recommended, while, if the air speed is the most important parameter, the intervals of air box volumes mentioned above should be used. Moreover, it can be observed that the highest values of air speed with a rectangular cross section cover a higher volume interval when compared to a triangular cross section, thus, suggesting that the former configuration allows more flexibility.

It is important to keep in mind that the shape of the air box also depends on the features of the location where the technology is installed, since an area larger than the one considered for the pavement prototype is generally available in the case of a real application.

Finally, in Section 3.3, it was shown that with half the air box volume of the first prototype (see Fig. 3.1) a lower surface temperature was obtained than with the whole volume. A similar result was obtained here with CFD simulations, which is a further confirmation of the effectiveness of this approach, especially considering that different system geometries were used.

c) Scaling up the simulations for larger installations

The prototypes and simulations considered so far were small-sized, thus, it is natural to wonder what would happen if they were to be scaled up to the size of a regular road. It is important to keep in mind that if this technology will be used in real pavements the length of the system will not be very variable, as it will be constrained by the size of the road. Therefore, in this section, two simulations with increased pavement lengths of 3500 mm and 7000 mm are discussed. Theses sizes were considered as they roughly correspond to the width of one and two-lane roads. Energy harvesting pipes could be installed in large areas, such as car parks, however, the lack of experimental data or design requirements makes their simulation meaningless for the purposes of this Thesis. Consequently, it was decided to use the exact same experimental setup outlined in Chapter 4 and to simply increase its length. Note that this section is meant to offer qualitative insight to guide future developments of this energy harvesting technique, therefore, no parameters will be varied to try and improve the performance of the system. This kind of analysis should be pursued in future work along with an experimental validation, as the simulations with increased

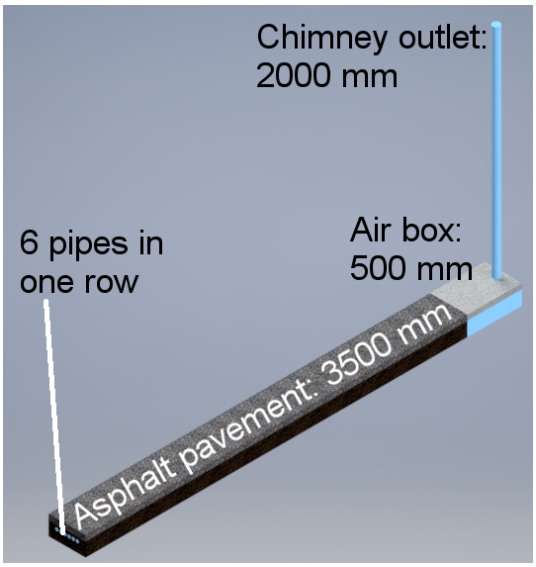

Figure 6.13: Rendered image of the domain of simulation (3500 mm length).

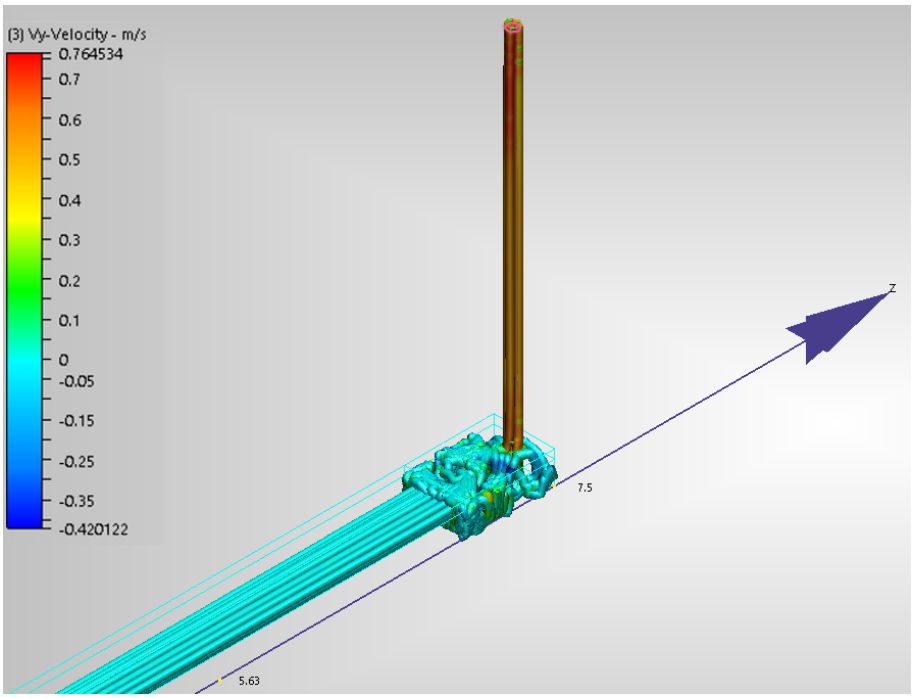

Figure 6.14: Particle traces showing the velocity in the vertical direction (7000 mm length).

length could not be compared to laboratory results or field tests due to the size and cost of such a large installation. Based on the experiments described in Chapter 4, the following features of the simulated one and two-lane roads were

fixed:

- pipe diameter: 30 mm;
- pipe pitch ratio: 37.5 mm;
- pipe arrangement: all pipes in one row;
- air box length: 500 mm;
- surface temperature: 70°C.

In the experiments performed in the context of this Thesis, it was shown that shorter chimney heights should be preferred due to a better performance (see Section 3.1), however, this may not be practical for an installation in a real road. Consequently, the outlet of the system was placed in a hypothetical 2000 mm long pole placed in the sidewalk, as seen in Fig. 6.13. The sidewalk represented in Fig. 6.13 is 500 mm long and represents the portion of a real sidewalk that could be hypothetically dedicated to the installation of an outlet air box.

The same computational setup outlined in the previous sections was used, as it was shown to be reliable for the representation of the physical phenomena at work. Under the assumption that the CFD model developed for small prototypes is also valid for a larger system, the two simulations were run to evaluate if a higher length of pipes and larger surface area of the pavement could cause an increase in the outlet air speed. In fact, in Section 3.1, it was shown that with the low air speed measured in the laboratory experiments the air flow was too slow to allow the extraction of energy through small-sized turbines. It is, thus, interesting to verify if this aspect could be improved by increasing the length of the pipes installed. The simulations yielded mean outlet air speeds of:

- 0.60 m/s for a pipe length of 3500 mm;
- 0.47 m/s for a pipe length of 7000 mm.

The result obtained for a pipe length of 3500 mm is higher than that shown in Chapter 4 for the experimental trials, while the result obtained for a length of

7000 mm is rather similar. Note that a direct comparison with the experimental results cannot be made, as the chimney height used in these computational simulations was different from that used in the pavement prototype. It can, however, be confirmed that eddies form in the air box even with a larger system, as seen by comparing Fig. 6.5 and 6.14.

The values of outlet air speed obtained in the simulations suggest that there should exist an optimal length of pipes that allows the best performance of the system. In fact, a higher length of pipes and a larger surface area of the pavement may cause a reasonable expectation for a higher outlet speed, as there is a higher path available for the air to harvest heat. This, however, is not observed in the results of the computational simulations, and the reason is that there exists a threshold length of the system above which the air in the pipes reaches equilibrium with the pavement temperature and, thus, cannot absorb more energy to power the buoyant flow. Therefore, if such threshold length is reached, the benefits from the larger surface area are overcome by the unavoidable fluid-dynamic losses that come with a longer path of the air flow. In the case of the simulations performed, the effect of these phenomena is a lower air speed at the system outlet, which is caused by a lower speed in the air box. The speed in the air box can be found rather easily by calculating the average air speed in this sub-domain in both cases. Note that the speeds in the outlet air box and at the chimney are different, as the former needs to be averaged across a volume, while the latter is the result of integration over a surface.

Further research could focus on the search for the threshold length for natural convection in this kind of system, as it is certainly a parameter of interest in the design of the technology. This, however, will not be a simple task, as the threshold length is expected to be a function of the weather conditions and of the location, because the buoyant flow is originated by heat exchanges between

the pavement and the environment. As a result, it is expected that such parameter will vary significantly based on the location chosen for a hypothetical installation.

6.3 Perspectives for modelling the performance of energy harvesting in the environment

While in the previous Section 6.2 the simulation of the whole phenomena at work in energy harvesting pavements was addressed, the aim of the present section is to evaluate if it is possible to predict the behaviour of the technology in the environment with simpler equations based on experimental results. The difference between this section and the discussion presented in Section 6.1 is that here no physical laws are considered. The approach presented in this Section is based on the data gathered in the experimental trials performed in the environment (see Section 5.3). The equipment used for the experimental trials consists of the GSHS coupled with an energy harvesting pavement prototype, as seen in Fig. 5.4 and 5.3, along with a control slab used for comparison purposes.

If the surface temperature of the control slab is represented versus the temperature difference with the prototype pavement and sorted in ascending order it can be observed that these parameters are not linearly related (see Fig. 6.15). Plotting data as shown in Fig. 6.15 can be useful if information on the pavement temperature in a chosen location is available, because it could be used to predict what would happen if energy harvesting pipes coupled with a heat source (e.g., a geothermal source) were installed. Such a prediction, however, is not simple, because of the non-linear behaviour seen in Fig. 6.15. In order to solve this issue it is possible to use a fitting equation, which, in the case under analy-

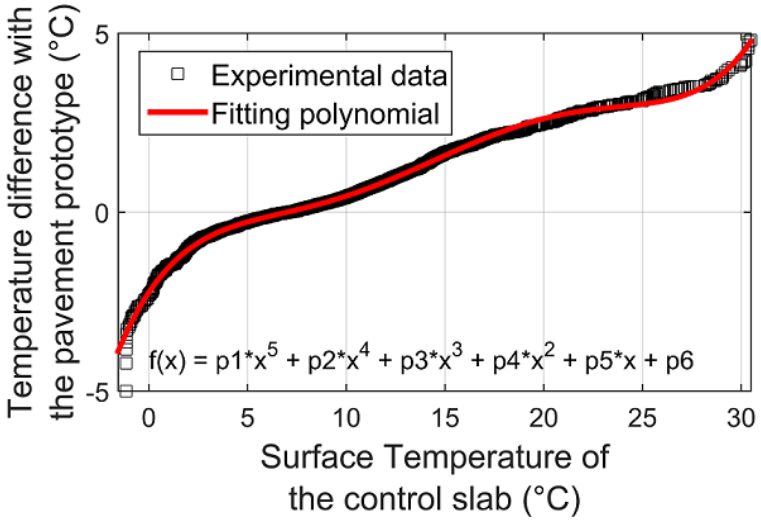

Figure 6.15: Surface temperature of the control slab vs. Temperature difference with the prototype pavement.

sis, is a fifth order polynomial ($R^2 = 0.9975$) with coefficients $p1 = 5.725e-6$, $p2 = -0.0004303$, $p3 = 0.01153$, $p4 = -0.1333$, $p5 = 0.8229$, and $p6 = -2.245$. The use of this fitting polynomial yields the results seen in Fig. 6.16, where it can be observed that the curves representing real and predicted temperatures are reasonably close to each other and that the error rarely exceeds ± 2°C. In the case of peaks, a higher error up to ± 5°C can be observed. This means that using a fitting equation to try and predict the effects of air flow under an asphalt pavement is acceptable only at an early design stage. Furthermore, the fitting equation is specific to the location considered, thus, the curve seen in Fig. 6.15 is very unlikely to be applicable in other locations. Finally, it is necessary to keep in mind that the curve might differ if other geometric configurations of the pipes or different inlet temperatures were considered. Therefore, a possible solution could be creating families of curves similar to the one in Fig. 6.15 corresponding to different designs of the system. This, however, is highly impractical, especially considering that the technique is not mature at the moment. Another obstacle to this approach is that databases of pavement temperatures are not common, thus, models should be used to predict the pavement tem-

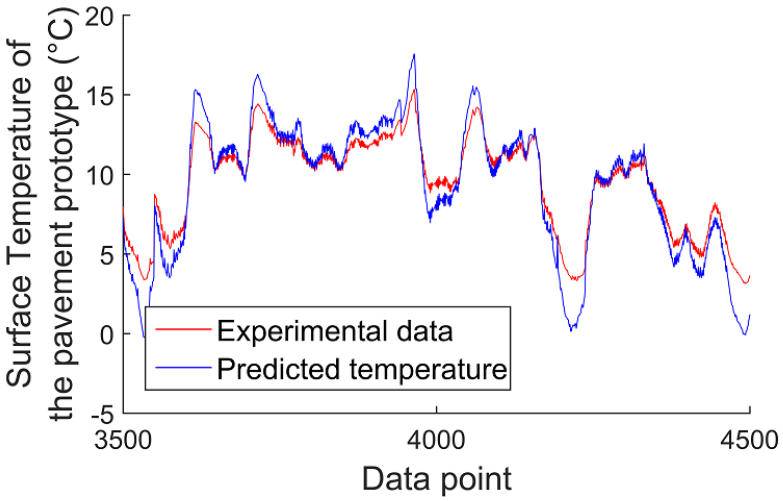

Figure 6.16: Prediction of the surface temperature of the prototype pavement.

perature based on the weather conditions. This could be achieved as explained by Minhoto et al. (2006), Sreedhar & Biligiri (2016), or Abo-Hashema (2013). The predicted temperature could then be used as an input for the above-mentioned fitting equation to try and evaluate the temperature mitigation effect caused by the air flowing under the pavement.

CHAPTER 7

Can pores replace pipes in convection-powered energy harvesting?

In this chapter, the fitness of air pores for a convection-powered flow is studied using computational fluid dynamics. Fluid flow in porous media has been approached computationally in various studies, e.g., Ghassemi & Pak (2010), Gruber et al. (2012), Umiliaco & Benedetto (2013), Siena et al. (2014), or Chen & Williams (2014), where pore networks obtained through a variety of approaches were analysed in 2D or 3D.

The approach chosen in this Chapter is different, as it was decided to analyse single pores rather than pore networks. Such pores were extracted from tomographies of a real asphalt core with air void content of 20%.

The use of single pores rather than pore networks is somewhat arbitrary, but it allows (i) to better understand the role of pipes in convection-powered energy harvesting pavement, and (ii) to verify if single connected air pores could be suitable for the creation of a reasonably effective air flow.

In order to perform this kind of analysis, two main aspects must be con-

sidered, namely, the choice of the air pores to use and the development of fluid-dynamic simulations. In the next sections, these matters are discussed in depth and the results obtained in the simulations are described.

7.1 Selection of suitable air voids for the analysis

Even if the approach chosen for the analysis of fluid flow in isolated asphalt air pores is arbitrary, care must be taken in the selection of suitable geometries for the analysis. For an air pore to be suitable it must (i) connect the top of the above-mentioned asphalt core to its bottom, and (ii) not be on the edges of the core, as this would yield unrealistic results. Furthermore, it is important to randomly choose the connected air pores needed for the analysis, so that the results will be unbiased and representative for the chosen core.

In order to pick connected air pores randomly it is necessary to analyse the tomography images and to verify whether each pore connects the top of the material to the bottom or not. In this Thesis, it was decided to approach this problem through a series of consecutive steps:

1. Loading the tomographies in image format in MATLAB;
2. Thresholding the tomographies (see, e.g., Masad et al. (1999)) to separate the air voids from the rest of the cores;
3. Saving the voids in a 3D Boolean matrix, where, e.g., 1 represents a void and 0 represents a pore;
4. Selecting random starting points in the air void space on the bottom of the imported asphalt core;
5. Verifying if the starting points belong to a pore that is connected to the top of the asphalt core;
6. Saving the starting points that belong to connected pores;

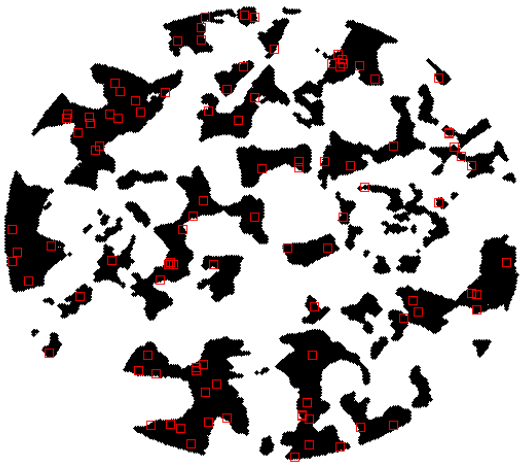

Figure 7.1: Example of starting points (red squares) used in the crawling algorithm in asphalt cores.

7. Interrupting the search when a satisfactory number of connected pores are found.

Step 5 is the most complex operation in the list above, as it requires the use of an algorithm that is able to navigate inside the pore space to check whether pores connect the top to the bottom of the material or not. For this purpose, a crawling algorithm was developed to analyse the connectivity of the samples. The algorithm works by seeding a particle (i.e., a point, as mentioned in step 4 above) on the bottom surface of the asphalt core and then allowing it to randomly travel inside the porous space and try to reach the top surface. An example of random starting points in the core considered is available in Fig. 7.1. The generation of the random patterns by the means of the crawling algorithm is possible because the void space is saved as a Boolean matrix, therefore, voids and matter can be easily told apart in a computational process. Random paths are generated by considering the 26 points surrounding a particle at any time (except for the top and bottom surfaces), as depicted in Fig. 7.2. In particular, at any step of the crawling algorithm a random number between 1 and 26 is picked based on the uniform distribution to determine the next position in the

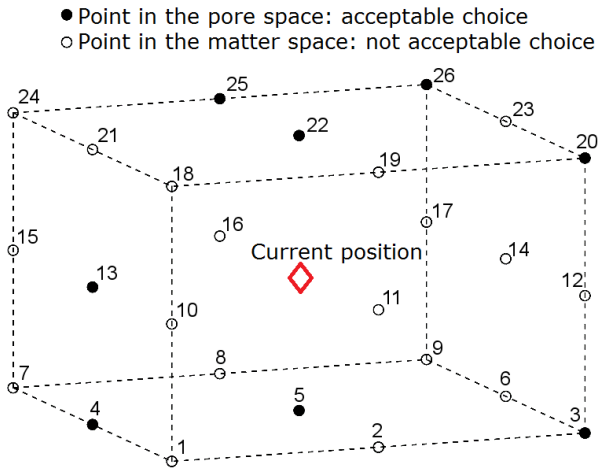

Figure 7.2: Graphical visualisation of a step of the crawling algorithm with positions available for the construction of the random path.

path through the pore space. Of course, the particle seeded is only allowed to move within the air voids, while the rest of the sample is not accessible. Therefore, the pattern in the pore space that is generated is completely randomised. The process is stopped if the seeded particle reaches the top surface (meaning that a connected path has been found) or if the number of steps inside the porous medium has reached an excessive value. The maximum number of steps that can be allowed has to be assessed based on the material and on the complexity of the porous space, however, it must be noted that due to the randomness of the process false negatives may be shown even if connected paths do exist. In the case of the asphalt mixture used in this study (thickness of 50 mm), 600,000 steps were effective for the detection of connected channels.

To better understand the operation of the crawling algorithm, a flowchart is available in Fig. 7.3. As seen in Fig. 7.3, if a starting point belongs to a connected air void it is saved along with its random path. Such saved path can be displayed in 3D (see Fig. 7.4), and then used to locate and isolate the connected pore in the 3D reconstruction of the whole pore network obtained from the thresholded tomography images.

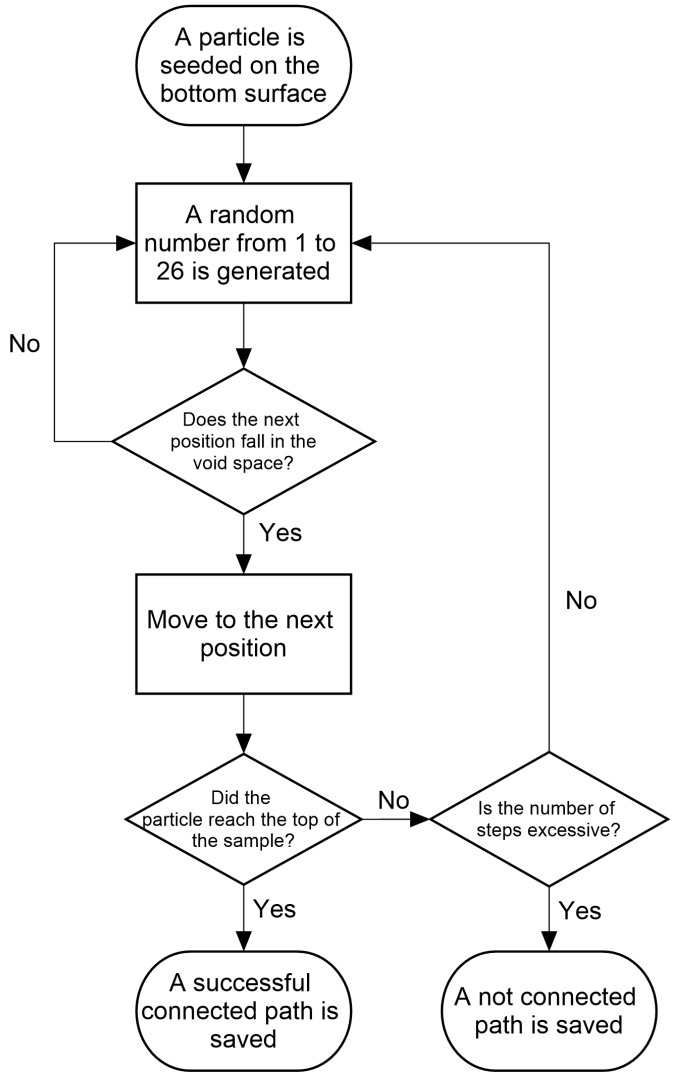

Figure 7.3: Flowchart of the algorithm used to analyse the connectivity of the void space.

The process described so far allows to find connected pores in an asphalt sample, however, further work is needed before they can be used for fluid dynamic simulations. This is because the isolated pores may have branches that end up in inner parts of the asphalt mixture and not to either end (top or bottom) of the material. Note that due to the randomness of the paths generated by the crawling algorithm these branches may or may not be present in 3D representations such as that shown in Fig. 7.4. A possible way to visualise all the existing branches is the skeletonisation of the isolated pores performed using

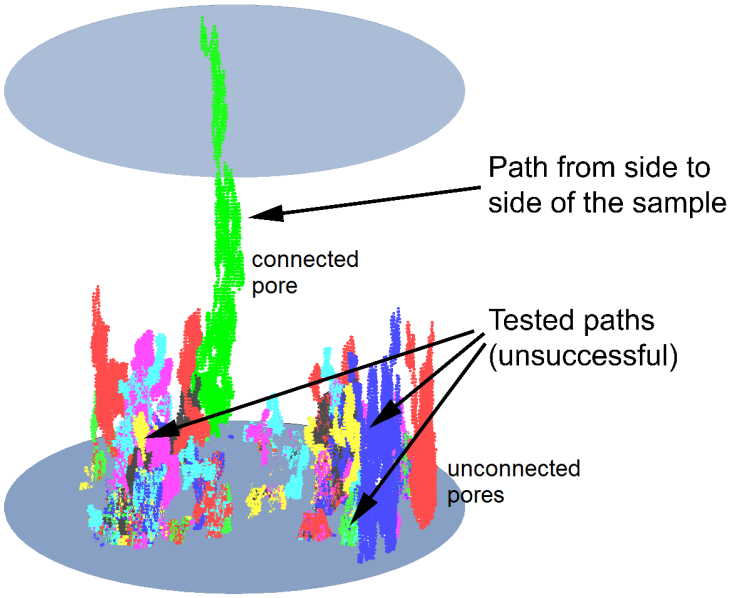

Figure 7.4: Examples of connected and unconnected paths found by the crawling algorithm.

the BoneJ plugin (v1.4.1, see Doube et al. (2010)) of ImageJ. As explained by Lee et al. (1994), the skeletonisation of a 3D image (in this case, a connected pore) is a thinning operation that aims to show the topology of a complex structure by the means of connected lines.

Once the skeleton of a pore is created, it is possible to effectively visualise the branches that do not lead to either end of the core. Thanks to this approach, such branches can be manually removed from the reconstructed pore structure, performing an operation called pruning. Pruning the unconnected branches is an important step, because it reduces the computational domain and, thus, the computational time required by the simulations. Furthermore, this operation is justified by the fact that these branches do not contribute to fluid flow and, consequently, can be classified as dead ends, as reported by Kutay (2009) (see Fig. 7.5). The result of the process used to modify the connected pores found with the crawling algorithm is the creation of a much simplified representation of a single pore in an asphalt sample, which allows for the study of fluid flow.

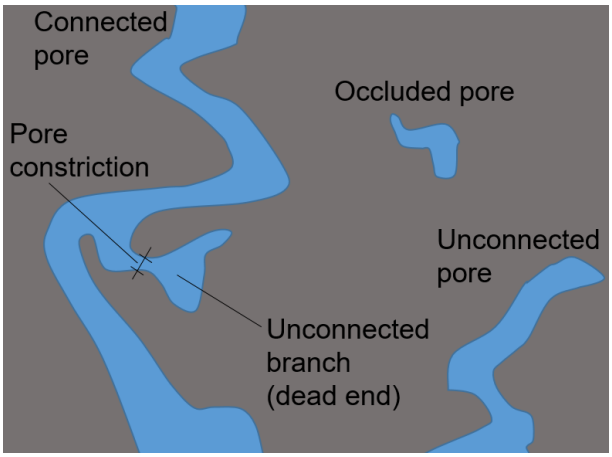

Figure 7.5: Scheme of a cross section of an asphalt sample with definition of the main types of pores.

For further technical details on the creation of the isolated pores, please see Appendix A.

7.2 Air flow simulations in asphalt pores

The process described in Section 7.1 was used to isolate 10 air pores from the above-mentioned asphalt core. Cylindrical inlets and outlets were added to the pores, as seen in Fig. 7.6 and further explained in Appendix A. The structure obtained for each pore was 170 mm long, with a 50 mm long pore placed between inlet and outlet. Examples of pores used in the analysis are available in Fig. 7.7. Note that the pores in Fig. 7.7 do not show sharp edges as one may expect in the case of asphalt mixtures. The reason for this is that the mesh of the pores had to be smoothed and refined several times to achieve convergence in the simulations.

In order to analyse the results of the simulations, the pores were classified based on their mean equivalent diameter, D_{eq}. Such a parameter was found by calculating the mean of the equivalent diameters for 10 cross sections of each pore (sampling every 5 mm). This procedure led to the following classification:

- small pore: 0 mm<D_{eq}<5 mm;
- medium pore: 5 mm <D_{eq}< 9 mm;
- large pore: 9 mm <D_{eq}< 20 mm.

It is important to point out that this classification is arbitrary and only relevant for the analysis presented here. This is because the number of structures that were isolated is not high enough to state that no better categorisation is possible and because the pore sizes considered refer to specific asphalt mixtures and air void contents and, thus, may not apply to other cases. Based on these three categories, the random selection of the void channels using the method described in Section 7.1 led to the following range of air pores:

- 5 large pores;
- 3 medium pores;
- 2 small pores.

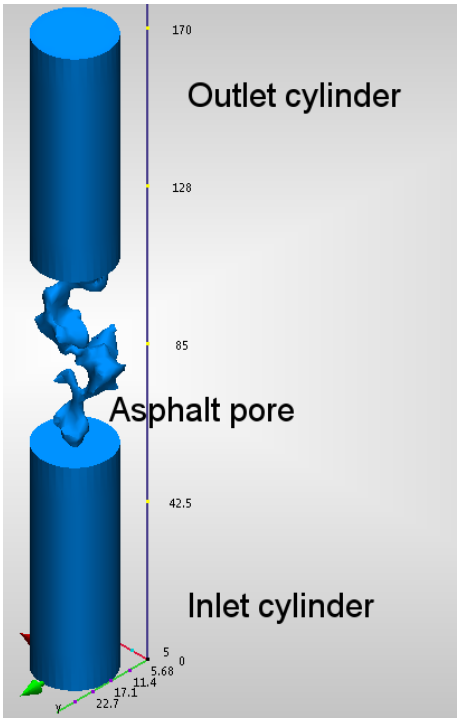

Figure 7.6: Pore with inlet and outlet imported in Autodesk Simulation CFD, sizes in mm.

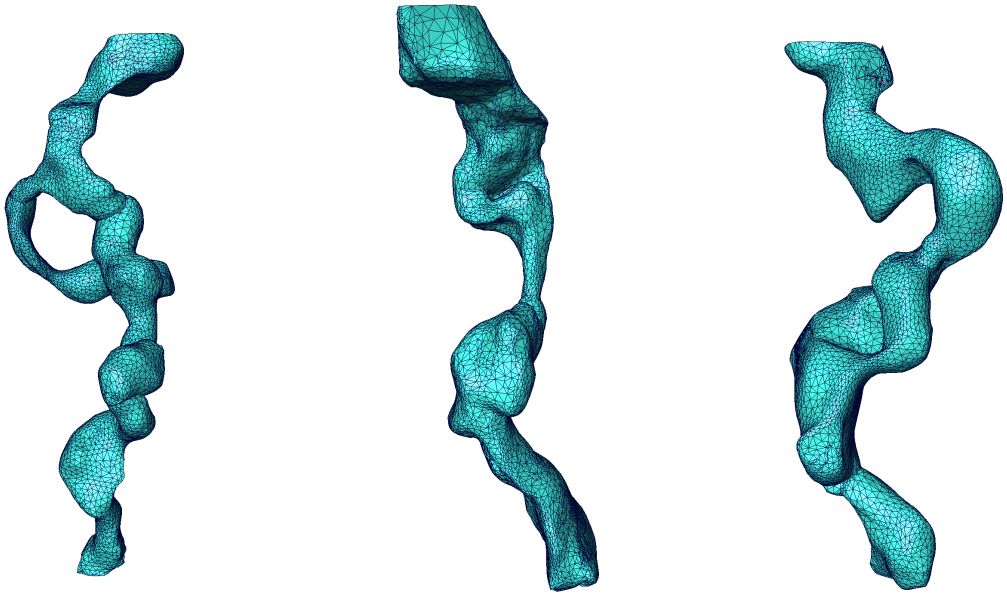

(a) Small: Sample 8 **(b)** Medium: Sample 4 **(c)** Large: Sample 2

Figure 7.7: Isolated pores used for the CFD simulations.

The 10 domains considered were loaded in Autodesk Simulation CFD and meshed. The mesh size in the isolated pores was set in the simulation software based on the level of precision that was required to achieve convergence in the solutions and to obtain stable results for at least 50 consecutive iterations, as done by Gruber et al. (2012).

Using 3D models as opposed to 2D cross sections of the materials obviously increases the computational cost of the simulations, however, this approach was chosen as Chen & Williams (2014) reported that results of 2D simulations in the case of asphalt mixtures are not always reliable. The reason given by Chen & Williams (2014) for this statement is that 2D representations of air pores fail to capture some important features, such as their shape, size, and 3D flow paths.

The boundary conditions considered in the simulations included an inlet air speed of 0.3 m/s and ambient pressure in the form of a gauge pressure of 0 Pa. In this Thesis, the air speed through the energy harvesting pavement proto-

types has not been studied, however, it can be hypothesised that it would likely be lower or equal to the speed at the chimney outlet. As a result, the value of 0.3 m/s as the inlet air speed was chosen because it represents an average of the values of outlet air speed measured (between 0 m/s and about 0.60 m/s).

Furthermore, in this section, gravity was not considered, as the air flow was not powered by buoyancy and the variation of the physical properties of the fluid was not relevant. As a result, the vertical orientation seen in Fig. 7.6 is simply convenient for illustration and does not carry any further meaning.

As done by other studies on this topic, the simulations were performed considering laminar flow (see, e.g., Kutay (2005), Ghassemi & Pak (2010), Gruber et al. (2012), Siena et al. (2014), or Chen & Williams (2014)). These sources show that the flow in the connected pores is always likely to be laminar, especially with the small velocity considered. It was, however, reported that local turbulent flow may exist (see, e.g., Chen & Williams (2014)). In this Thesis, this aspect is neglected, as the focus is on the average performance in the pores rather than on the analysis of local effects. The equations considered to solve the fluid-dynamic problem are the same as described in Section 6.2.

It is relevant to mention that, in a laboratory environment, it is very complex (if not impossible) to test single pores. Therefore, the results presented in this section must be considered as a qualitative description of the phenomena at work due to the lack of an experimental validation of the approach. The results obtained in the simulations are gathered in Table 7.1 along with the variance and the mean equivalent diameter of each pore considered. As done by Siena et al. (2014), the results are reported in terms of the mean air speed in the vertical direction in each sample considered.

The first observation that can be drawn from Table 7.1 is that decreasing values of the mean pore diameter D_{eq} cause the air speed in the axial direction

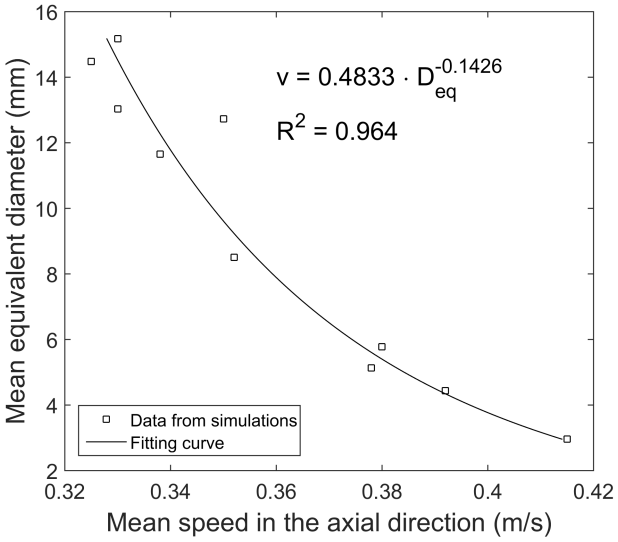

Figure 7.8: Relationship between mean pore diameter and mean speed in the axial direction.

to increase, due to the principle of conservation of mass. In fact, due to the Venturi effect, a lower diameter (i.e., a constriction) also causes the pressure of the fluid to drop. To some extent, the velocity increase will be offset by increased friction between air and the pore walls as the constriction gets smaller. Furthermore, based on the results obtained, it appears that the mean pore diameter and the mean speed in the axial direction are linked by a power law, as shown in Fig. 7.8. The relationship used is in the form $v = k_1 \cdot D_{eq}^{-k_2}$ and the values of k_1 and k_2 obtained for the fitting curve are shown in Fig. 7.8.

The variance in the computational results is rather low when calculated for the whole dataset (see Table 7.1). In addition, if the variance is calculated by category, even smaller values are obtained. This indicates that the categories that were identified are reasonable and that there may exist some relationship between mean air speed and some form of classification of the mean diameter of the pores. Note that tortuosity is not used to comment on the computational results that were obtained, as this parameter is not expected to vary extensively in a single asphalt core.

Table 7.1: Results of air flow simulations in isolated pores.

Pore number	D_{eq} (mm)	Category	Mean axial air speed (m/s)	Variance (m^2/s^2)	Variance in the category (m^2/s^2)
1	11.65	Large	0.338	5.57E-04	1.43E-05
2	12.73	Large	0.350	1.35E-04	2.49E-04
3	14.48	Large	0.325	1.34E-03	8.50E-05
4	5.13	Medium	0.378	2.69E-04	5.88E-05
5	13.03	Large	0.330	9.99E-04	1.78E-05
6	15.17	Large	0.330	9.99E-04	1.78E-05
7	8.51	Medium	0.352	9.22E-05	3.36E-04
8	4.44	Small	0.392	9.24E-04	7.06E-05
9	2.96	Small	0.415	2.85E-03	2.13E-04
10	5.78	Medium	0.380	3.39E-04	9.34E-05

Furthermore, even if Table 7.1 only shows positive values of the mean air speed, it is important to keep in mind that this parameter can, locally, sometimes be negative in the 3D domains. This phenomenon was seen in the majority of the single air pores considered and its presence in asphalt samples was previously reported by Chen & Williams (2014). The presence of backward flow, however, was only a localised phenomenon and did not affect significantly the overall air flow through the pores considered.

In addition to the study of the air speed in the pores seen in Table 7.1, it is worth considering the pressure drops caused by their 3D shape. In the simulations performed, such pressure drops were found to be 4 ± 0.3 Pa over a length of 50 mm. Under the simplification that the pressure drops increase linearly with the length of a pore, the losses per metre may be estimated as up to 86 Pa. For the purpose of a comparison, the pressure drop per metre ($\Delta p/L$, in Pa/m) in laminar flow in a pipe with a diameter of 30 mm can be estimated with the Darcy-Weisbach equation:

$$\frac{\Delta p}{L} = f_D \cdot \frac{\rho}{2} \cdot \frac{v^2}{D} \tag{7.2.1}$$

where f_D is the Darcy friction factor, ρ is the density of the fluid, v is the mean flow velocity, and D is the internal diameter of the pipe. The Darcy friction factor in laminar flow is found as:

$$f_D = \frac{64}{Re} \tag{7.2.2}$$

where Re is the Reynolds number (see Eq. 3.1.1). The result of this calculation for a pipe yields about 0.2 Pa/m, which is much lower than the value found for isolated pores. The main reasons for this rather large difference are that (i) a pore is not straight, thus, it includes several minor losses caused by changes in its shape, cross section and orientation; and (ii) the average diameter of the pores is, in some cases, much lower than that of the pipe considered. In fact, if a smaller pipe were to be considered, the following pressure drops would be obtained with the Darcy-Weisbach equation:

- 0.3 Pa/m for a diameter of 25 mm;
- 0.5 Pa/m for a diameter of 20 mm;
- 0.8 Pa/m for a diameter of 15 mm;
- 2 Pa/m for a diameter of 10 mm;
- 8 Pa/m for a diameter of 5 mm.

It is easy to show how the pressure losses in a pipe over a length of 50 mm could be up to 0.4 Pa and that this value is still much lower the lowest pressure loss found in the simulations using the air pores.

Furthermore, based on the same assumptions outlined in Section 4.6, let us assume that the pressure difference between the ends of a 1000 mm long energy harvesting pipe is 20 Pa. In this case, it appears clear that all the pipe diameters mentioned above would be suitable for air flow, while the air pores would not, even in the best case scenario of a large and mostly straight pore. In fact, the minimum pressure drops found in the isolated pores are 74 Pa/m.

Should a pore network be considered in the place of a single pore, the

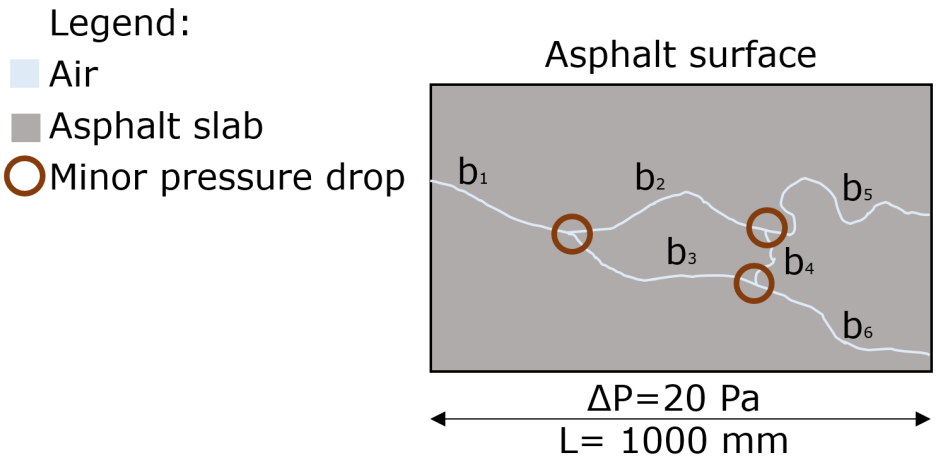

Figure 7.9: Simplified scheme of a portion of a pore network (b=branch).

situation would likely be even less advantageous. In fact, several additional pressure drops would have to be considered at every bifurcation of the flow path (see Fig. 7.9). This would cause the total pressure losses to be too high to be overcome by the assumed pressure differential of 20 Pa between two sides of the material (if the same pressure losses per metre computed above are considered). The issues related to pressure losses would also be exacerbated by the fact that the flow is convection powered. Due to the very mechanism regulating natural convection, i.e., buoyancy, the heated air would tend to flow upwards. Thus, the presence of vertically oriented branches (see b_4 in Fig. 7.9) would likely cause part of the air flowing in branch b_3 to rise through b_4 and exit the asphalt slab through b_5. Furthermore, were a branch such as b_4 connected to the surface, it would cause the air flowing through the asphalt slab to escape to the environment, which would have to be considered as an additional outlet. This issue was previously reported by Pascual-Muñoz et al. (2013), who state that leaks to the surface exist unless a solution such as a multi-layered pavement with a porous layer embedded between two very dense layers is used.

Based on the concepts discussed so far, if appears that a low-speed air flow in short pores can be sustained with the range of mean equivalent diameters considered. However, it is clear that two types of issues would arise when

considering natural and full length pore networks as a replacement for energy harvesting pipes, i.e., fluid-dynamic and practical issues.

Fluid-dynamic issues are related to the fact that a longer path for the fluid is intrinsically characterised by higher head losses. Furthermore, it is expected that, in a longer pore network, more changes in the pore shape, size, and orientation will exist. As a result, minor losses would probably causing the air speed over a length of several metres to drop to values too low to be either measured or effective. Note that this effect cannot be reproduced with the boundary conditions used in this section. In fact, when an inlet speed and a pressure are set at the boundaries of the domain, the CFD solver will compute the properties of the flow based on them, meaning that the outlet speed cannot be null unless the simulation is set up to achieve this. Further theoretical considerations to support the principles mentioned above can be found in Section 4.5. Moreover, it must be kept in mind that the concepts presented so far are valid only in the case where very long pore networks exist, which is a rather big assumption that should be verified based on the real asphalt mixtures that would be used.

In addition, the number of connected pores would influence the total mass flow obtained at the end of the pavement section, thus, making it very hard to design a system based on a target performance. This is because the analysis of the fluid-dynamic phenomena at work is much simpler when pipes are considered, as they have a constant cross section and a regular shape, which allow for a clearer and more reliable analysis. This is the very reason why practical issues exist along with the concerns mentioned above. In fact, since the design of asphalt mixtures is not based on physical models but rather on empirical principles, it is not easy to predict how many pores will exist in a designed sample, what percentage of them will be connected, and which shapes they will have. As a result, the design of energy harvesting pavements based on the

use of natural pores would not be reliable as an air speed and mass flow could hardly be hypothesised. A solution to this could be to gather a large amount of asphalt samples and to test them to verify how asphalt design influences convective air flow through pores. However, this subject should be pursued only in the case this technology will gather a wider interest from researchers and industry.

Furthermore, another practical issue is that asphalt pavements with the somewhat high pore size required to allow air flow may or may not be suitable in terms of the mechanical properties required for them to be used as infrastructure. Therefore, further studies on this topic should be performed before considering the use of natural pores for energy harvesting purposes.

7.3 Final remarks on air flow in asphalt pores

In conclusion, even if small pores seem suitable to allow a low-speed air flow, it is clear that many secondary issues must be considered for a full-length system. These issues may prevent natural pore networks from being used for energy harvesting purposes, as pipes allow a more reliable thermal and fluid-dynamic design thanks to their simplicity. Therefore, the natural conclusion of this section is that, at least for the time being, pipes should be used for practical implementations of the technique to support its early adoption. This is because the use of air convection for energy harvesting is a rather young technique, thus, better and simpler approaches for its design must be developed before more complex matters such as convective flow through pores are tackled.

CHAPTER 8

Conclusions and future work

8.1 Conclusions

In the following sections, the most important findings obtained through the experimental trials and computational studies reported in this Thesis are summarised along with some recommendations for future work. Most of these have been prepared as papers, as listed in Appendix B.

Probably, the most important conclusion of this research is that it is possible to build and use convection-powered energy harvesting pavements where air is the operating fluid. This conclusion might seem trivial, however, this had been previously discussed only by García & Partl (2014) and no comprehensive analysis was present in the scientific literature before the research described here was carried out. The proof of the feasibility of this approach to energy harvesting was found through the analysis of two main features of the technology, namely:

- the presence of an air flow at the outlet of the system without using any sort of flow-forcing equipment;
- the fact that the surface temperature of a hot pavement can be reduced when air is allowed to flow through it.

These aspects were analysed in one or more experimental and computational trials, which confirmed the feasibility of the approach and evaluated the extent of the temperature mitigation achieved.

From the point of view of the air flow, it was found that the outlet air speed in the energy harvesting prototypes ranged between 0 m/s and 0.58 m/s. This finding led to the discovery that it is unlikely that electrical energy can be produced using small-sized energy harvesting pavements coupled with small-sized turbines, as the air flow did not reach the cut-off speed that is commonly required by such turbines. However, at this stage, it cannot be excluded that this will be possible with purposely-designed larger installations.

In laboratory trials and in the case of short flow paths, it was found that the temperature reduction effect achieved by the energy harvesting prototype pavements considered was up to 6°C. This result was confirmed during trials in the natural environment, where the temperature mitigation effect was quantified for both warm and cold periods as about $\pm$ 5°C. Note that a heating effect during cold periods can only be achieved if the inlet of the energy harvesting pavement is coupled with a heat source. In fact, when the pavement is cold, air needs another driving force to be able to flow upwards through the pipes and the chimney outlet. In this Thesis, this was achieved by the means of a novel piece of equipment called the Ground Source Heat Simulator, which was used to feed air at a stabilised temperature (representative of geothermally heated air) to the pavement during both warm and cold weather. It is important to keep in mind that the results obtained in the environment are specific to the prototype used and the weather conditions reported for Nottingham, UK, thus, a different performance may be found elsewhere.

From a general point of view, it can be concluded that the use of convection-powered energy harvesting pavements could be helpful for the maintenance

of pavements, as it causes a reduction of the oscillations in their temperatures. As a result, this technology could be beneficial throughout the year for the following reasons:

- when the environmental temperature is high, the use of energy harvesting allows a reduction of the pavement surface temperature. Therefore, it can allow a reduction in asphalt thermal cracking and in premature rutting. In addition, the Urban Heat Island (UHI) effect can be reduced, thus, implying a reduction of the energy consumption for ambient cooling in adjacent buildings and an improvement in the level of thermal comfort for people in urban areas.
- When the environmental temperature is low, energy harvesting pavements coupled with external heat sources (e.g., geothermal) can increase the pavement surface temperature, thus, reducing the risk of ice formation. In turn, this increases the reliability of the road network and the safety for road users.

Furthermore, in this Thesis, the features related to the construction and configuration of energy harvesting pavement prototypes were investigated by the means of numerous experimental and computational trials. In particular, the following aspects were studied:

- the height and diameter of the chimney;
- the pipe arrangements in the aggregate layer;
- the influence of the size and shape of the outlet air box;
- the use of precast concrete slabs in the place of pipes.

The data gathered during the experimental trials was used to set up and validate Computational Fluid Dynamics (CFD) models of the energy harvesting prototype pavement, which allowed the formulation of some of the conclusions listed below. The investigations on the construction and configuration of the

technology that were performed led to a number of specific conclusions, i.e.:

- the height and the diameter of the system outlet have an equal importance for the final performance of the system, which means that an optimal balance needs to be found based on the aims of the energy harvesting process;
- the speed at the chimney outlet is the result of a combination of thermodynamics and fluid-dynamics effects, thus, it is influenced by the design of the system (i.e., its shape, size, and material);
- the maximum thermal efficiency of the energy harvesting process was found to be up to 15%;
- the calculation of the mass flow through the chimney outlet suggested that this parameter is closely related to the performance of the system. In addition, the fact that the mass flow has a high importance for the performance of the system is an indication that a fluid-dynamics understanding is needed for the description of the physical phenomena at work;
- the pipe arrangement allowing the highest performance in terms of surface temperature reduction and outlet air speed is the installation of all the energy harvesting pipes or channels in a row;
- it is possible to use precast concrete channels in the place of the pipes installed under the asphalt wearing course, however, further studies are required owing to their reduced performance, which is linked to a combination between thermophysical properties and head losses. In order to have a good fluid-dynamic performance, the concrete channels should have a semicircular cross section because it causes lower head losses;
- the air box (the pipe exit manifold) should have a rectangular cross section to provide more flexibility in the design, as this shape allows relatively high air speeds for a wide range of air box volumes;

- by modifying the air box volume it is possible to emphasise either the temperature reduction effect or the outlet air speed, thus, this volume must be chosen appropriately based on the aim of the installation;
- it is not recommended to replace the air box with a smoothed manifold geometry, as this allows very little temperature reduction effect (although a reasonable outlet air speed of 0.32 m/s was achieved in the simulations reported herein);
- a CFD approach is required to model the performance of the technology, as a simplified analysis based on one-dimensional thermodynamics yielded relative errors that, in some cases, exceeded 20%;
- the use of CFD simulations showed that there exists a threshold length of the pavement above which thermal equilibrium with the surface temperature may be reached: as a result, while the temperature of the air flowing under the pavement cannot increase further, the head losses will increase with the length of the system, thus, causing the air speed to decrease.

Along with these results, the harvested energy and exergy were calculated. In particular, it was found that the maximum difference between the various geometric configurations of the energy harvesting prototypes in terms of harvested exergy was about 20 kJ (for a surface area of about 0.30 m^2), which is a rather small value. This suggests that modifications of the structure of the system do not have a strong impact on the final performance. Moreover, the harvested energy was generally low, meaning that low-enthalpy systems such as heat pumps should be considered when studying applications for this technology.

Experimental trials in the natural environment allowed the clarification of the link between the temperature mitigation effect and the weather conditions. The experimental results showed that during warm weather the pavement temperature was principally influenced by moisture and by the presence of

rainwater on the pavement surface, while no strong link was found with the temperature of atmospheric air. Furthermore, wind was found to have a negative correlation with the pavement temperature, which means that higher wind speeds lower the amount of energy that can be harvested. This is clearly not a bad aspect for the durability of the pavement, however, if the objective is harvesting energy, the presence of wind has to be considered as an issue. On the other hand, during cold periods, the pavement temperature was found to depend strongly on the temperature and humidity of the atmospheric air.

The experimental trials in the environment allowed a quantification of the amount of energy that was exchanged in the system. On average, the energy exchanged was found to be in the range between -200 kJ and 200 kJ ($\pm$606 kJ/m^2), with peaks up to $\pm$600 kJ. In the case of the prototype considered, this range corresponds to an average temperature difference of up to $\pm$2°C. In addition, these experiments yielded lower outlet speeds than the laboratory trials, with values between 0 m/s and 0.30 m/s. This is a further indication that the likelihood of harvesting electricity exploiting the air flow obtained from the small-sized prototypes used is low. It is, however, important to mention that the lowest values of outlet air speed (between 0 m/s and 0.08 m/s) in the environmental trials corresponded to the cold periods. This means that when no energy harvesting is possible the air flow is powered only by the very small density difference between the geothermally pre-heated air in the pipes and the environmental air.

The conclusion of this Thesis is that it is possible to harvest energy by the means of an air flow through asphalt pavements. However, due to the strong dependency of the performance of the system on the environmental conditions and to the lack of mechanical ventilation, their design and configuration require a high attention to detail and solutions specific to the chosen location. In

addition, the energy considered in this Thesis was only thermal, which may be a limitation for future developments, since heat is generally not regarded as a highly valuable form of energy.

Consequently, further studies in this field must be performed to evaluate if the benefits that come with the use of this technology are high enough to justify the design effort and the investments required. This could be done by comparing the convection-powered energy harvesting technique to other pavement temperature management options (e.g., changes in the physical properties of the mixture or water-based systems) in order to evaluate the benefits in terms of sustainability, life cycle cost and economic cost (see, e.g., Brown et al. (2014)).

8.2 Future work

In this Thesis, numerous aspects related to convection-powered energy harvesting pavements were analysed and discussed. As a result, it was possible to gather information that can provide guidance for future studies on the topic.

Since it was shown that the pavement may be coupled with a geothermal source, it is suggested that this option is further explored. In fact, this configuration allowed a reasonably good performance during both summer and winter, thus, meaning that this would be a good starting point for further studies. A possible improvement to this configuration would be to find an optimal temperature for the underground reservoir that would maximise the effects of air flow on the pavement independently from the weather conditions. A lower temperature for the ground source heat would improve the performance of the system in summer conditions, as there would be a higher temperature difference between the air and the pavement surface (which would improve heat transfer), while a higher underground temperature would lead to a better per-

formance in winter. However, finding an optimal temperature is not an easy task, because it will depend on:

- the climate of the location: based on the weather conditions, it may be smart to preferentially optimise the arrangement for either warm or for cold weather;
- the availability of geothermal heat: if this condition is not satisfied, different heat sources such as heat storage or the exploitation of residual heat from buildings may need to be considered. In addition, in the case these technological solutions are needed, the location of the installation will mostly be constrained to urban areas;
- the costs of the excavation works: in the case of winter-optimised installations, heat at a higher temperature will normally be found deeper beneath the surface, but it may not always be financially feasible to exploit this.

This optimisation can be pursued in two alternative ways, i.e., by trial-and-error experiments in the location of interest or by performing computational simulations. The former option is interesting because it is theoretically simpler and does not require much knowledge, however, it certainly is more expensive, while the latter offers solid cost savings and the possibility to test a large number of configurations in a short time. Nevertheless, it must be kept in mind that the computational path requires input data on the weather conditions and geothermal heat in the location of interest, thus, proving impossible in cases where this information is not available.

Both the experimental and the computational approach can also be used to analyse what was called the threshold length of the pavement. In fact, since the pressure differences driving the buoyant flow are rather low, it is very important to make sure that the system is fully optimised before an installation is finalised. If this is not done, pressure losses may cause a lower air speed and,

consequently, a lower performance. It is easy to understand that care must be taken in the choice of an optimal temperature and length for the installation, as the energy harvesting system will be embedded in the pavement and in the soil, thus, it will be expected to stay there for a long period of time. As a result, bad design will almost certainly lead to an ineffective installation that will bring few benefits.

A study of the effects caused by buildings near an energy harvesting pavement could be pursued (see, e.g., Nasir et al. (2015)) in order to evaluate their influence on the performance of the system. In fact, it is expected that shading and thermal radiation from the structures surrounding an energy harvesting installation will highly influence its behaviour.

From the point of view of the energy harvesting pavement itself, it is recommended that pipes in a single row are used in future studies. Furthermore, dense asphalt mixtures seem to be the the best option for the wearing course, as they do not allow water infiltration. In fact, water is able to subtract energy from pavements by the means of evaporation, thus, influencing the performance of the energy harvesting or pavement heating processes. In addition, it is expected that better designs could be developed for the system outlet in order to optimise the air speed in the chimney in the case where it is relevant for the final use chosen. These aspects could be studied either experimentally or computationally. If the computational path is chosen, it is recommended that transient models are developed and tested, because, in this Thesis, only steady-state simulations were performed.

Finally, it is recommended that future investigations on energy harvesting pavements consider the use of the harvested energy, the financial suitability of the technology, its structural resistance, and the sustainability and recyclability of the material used.

References

Abo-Hashema, M. (2013), Modeling pavement temperature prediction using artificial neural networks, *in* '2013 Airfield & Highway Pavement Conference, Los Angeles, California', pp. 490–505.

Akbari, H., Berhe, A. A., Levinson, R., Graveline, S., Foley, K., Delgado, A. H. & Paroli, R. M. (2005), Aging and weathering of cool roofing membranes, *in* '2005 Cool Roofing Symposium, Atlanta, Georgia'.

Akbari, H., Rose, L. S. & Taha, H. (1999), *Characterizing the fabric of the urban environment: A case study of Sacramento, California*, U. S. Environmental Protection Agency. LBNL-44688.

Arabani, M. & Mirabdolazimi, S. (2011), 'Experimental investigation of the fatigue behaviour of asphalt concrete mixtures containing waste iron powder', *Materials Science and Engineering* **528**, 3866–3870.

Assael, M. J., Gialou, K., Kakosimos, K. & Metaxa, I. (2004), 'Thermal conductivity of reference solid materials', *International Journal of Thermophysics* **25**, 397–408.

Autodesk, Inc. (2015), 'Working with fluid materials', *Autodesk Knowledge Network* .

Avila, K., Moxey, D., de Lozar, A., Avila, M., Barkley, D. & Hof, B. (2011), 'The onset of turbulence in pipe flow', *Science* **333**, 192–196.

Barbato, M., Bowman, M. & Herbin, A. (2010), *Performance Evaluation of Buried Pipe Installation*, Louisiana Transportation Research Center , 53–55.

Bejan, A. (2013), *Convection Heat Transfer*, Wiley, 537–546.

Bluestein, M. (2015), *Reference Module in Earth Systems and Environmental Sciences, Encyclopedia of Atmospheric Sciences (Second Edition), Basic Atmospheric Structure and Concepts | Wind Chill*, Elsevier B.V., 7–11.

Bobes-Jesus, V., Pascual-Muñoz, P., Castro-Fresno, D. & Rodriguez-Hernandez, J. (2013), 'Asphalt solar collectors: A literature review', *Applied Energy* **102**, 962–970.

Brown, H., Kraus, M. & Bowders, J. (2014), 'Decision methodology for temperature control of pavements', *Transportation Research Record: Journal of the Transportation Research Board* **2403**.

Carnielo, E. & Zinzi, M. (2013), 'Optical and thermal characterisation of cool asphalts to mitigate urban temperatures and building cooling demand', *Building and Environment* **60**, 56–65.

Çengel, Y. (2008), *Introduction to Thermodynamics and Heat Transfer*, McGraw-Hill, 27–30.

Çengel, Y. & Boles, M. (2010), *Thermodynamics: An Engineering Approach*, McGraw-Hill, 423–470.

Chen, C. & Williams, R. (2014), 'Water flow simulation and analysis in hma microstructure', *Journal of Traffic and Transportation Engineering (English Edition)* **1**, 362–370.

Chen, M., Wu, S., Wang, H. & Zhang, J. (2011), 'Study of ice and snow melting

process on conductive asphalt solar collector', *Solar Energy Materials and Solar Cells* **95**, 3241–3250.

Chiarelli, A., Dawson, A. & García, A. (2015*a*), 'Analysis of the performance of an air-powered energy harvesting pavement', *Transportation Research Record: Journal of the Transportation Research Board* **2523**, 156–163.

Chiarelli, A., Dawson, A. & García, A. (2015*b*), 'Parametric analysis of energy harvesting pavements operated by air convection', *Applied Energy* **154**, 951–958.

Chiarelli, A., Dawson, A. & García, A. (2016), Mitigation of asphalt pavement temperatures by the means of natural air convection, *in* '4th International CEW, Delft, The Netherlands'.

Dawson, A. R., Dehdezi, P., Hall, M., Wang, J. & Isola, R. (2012), 'Enhancing thermal properties of asphalt materials for heat storage and transfer applications', *Road Materials and Pavement Design* **13**, 784–803.

Dongellini, M., Naldi, C. & Morini, G. (2015), 'Seasonal performance evaluation of electric air-to-water heat pump systems', *Applied Thermal Engineering* **90**, 1072–1081.

Doube, M., Klosowski, M., Arganda-Carreras, I., cordeliéres, F., Dougherty, R., Jackson, J., Schmid, B., Hutchinson, J. & Shefelbine, S. (2010), 'Characterization of the packing of aggregate in concrete by a discrete element approach', *Bone* **47**, 1076–1079.

Ferguson, C. J. (2009), 'An effect size primer: A guide for clinicians and researchers', *Professional Psychology: Research and Practice* **40**, 532–538.

Gago, E. J., Roldan, J., Pacheco-Torres, R. & J.Ordonez (2013), 'The city and urban heat islands: A review of strategies to mitigate adverse effects', *Renewable and Sustainable Energy Reviews* **25**, 749–758.

García, A., Norambuena-Contreras, J., Bueno, M. & Partl, M. (2014), 'Influence of steel wool fibers on the mechanical, termal, and healing properties of dense asphalt concrete', *Journal of Testing and Evaluation* **42**, 1–12.

García, A. & Partl, M. (2014), 'How to transform an asphalt concrete pavement into a solar turbine', *Applied Energy* **119**, 431–437.

George, W. K. (n.d.), 'An introduction to natural convection flows', `http://www.turbulence-online.com/Publications/Lecture_Notes/Natural_Convection_Lectures.pdf/`. Accessed Oct. 14, 2015.

Ghassemi, A. & Pak, A. (2010), 'Pore scale study of permeability and tortuosity for flow through particulate media using lattice boltzmann method', *International Journal for Numerical and Analytical Methods in Geomechanics* **35**, 886–901.

Gommes, C., Bons, A., Blacher, S., Dunsmuir, J. & Tsou, A. (2009), 'Practical methods for measuring the tortuosity of porous materials from binary or gray-tone tomographic reconstructions', *American Institute of Chemical Engineers* **55**, 2000–2012.

Gruber, I., Zinovik, I., Holzer, L., Flisch, A. & Poulikakos, L. (2012), 'A computational study of the effect of structural anisotropy of porous asphalt on hydraulic conductivity', *Construction and Building Materials* **36**, 66–77.

Gui, J., Carlson, J., Phelan, P. E., Kaloush, K. E. & Golden, J. S. (2007), 'Impact of pavement thickness on surface diurnal temperatures', *Journal of Green Building* **2**, 121–130.

Guldentops, G., Nejad, A. M., Vuye, C., den bergh, W. V. & Rahbar, N. (2016), 'Performance of a pavement solar energy collector: Model development and validation', *Applied Energy* **163**, 180–189.

Guntor, N. A. A., Din, M. F. M., Ponraj, M. & Iwao, K. (2014), 'Thermal performance of developed coating material as cool pavement material for tropical regions', *Journal of Materials in Civil Engineering* **26**, 755–760.

Hall, M., Dehdezi, P., Dawson, A., Grenfell, J. & Isola, R. (2012), 'Influence of the thermophysical properties of pavement materials on the evolution of temperature depth profiles in different climatic regions', *Journal of Materials in Civil Engineering* **24**, 32–47.

Hassn, A., Chiarelli, A., Dawson, A. & García, A. (2016b), 'Thermal properties of asphalt pavements under dry and wet conditions', *Materials and Design* **91**, 432–439.

Haynes, W. M. (2012), *Handbook of chemistry and physics*, CRC Press, 240–241.

Kakaç, S., Liu, H. & Pramuanjaroenkij, A. (2012), *Heat Exchangers: Selection, Rating, and Thermal Design, Third Edition*, CRC Press, 283–298.

Katona, M. (2015), 'Culvert analysis and design (cande) user manual and guideline', `http://www.candeforculverts.com/f/CANDE-2015_User_Manual.pdf`. Accessed June. 10, 2016.

Kaye & Laby Online (2005), 'Tables of Physical & Chemical Constants. 2.3.7 Thermal conductivities, Version 1.0', `http://www.kayelaby.npl.co.uk/general_physics/2_3/2_3_7.html`. Accessed Apr 12, 2016.

Kent, M. G., Altomonte, S., Tregenza, P. R. & Wilson, R. (2015), 'Temporal variables and personal factors in glare sensation', *Lighting Research and Technology* pp. 1–22.

Kömle, N. I., Bing, H., Feng, W. J., Wawrzaszek, R., Hütter, E. S., He, P., Marczewski, W., Dabrowski, B., Schröer, K. & Spohn, T. (2007), 'Thermal conductivity measurements of road construction materials in frozen and unfrozen state', *Acta Geotechnica* **2**, 127–138.

Kutay, M. (2009), 'Pore pressure and viscous shear stress distribution due to water flow within asphalt pore structure', *Computer-Aided Civil and Infrastructure Engineering* **24**, 212–224.

Kutay, M. E. (2005), Modeling Moisture Transport in Asphalt Pavements, PhD thesis, University of Maryland, 1–12, 49–54.

Lee, H. G. & Kim, J. (2011), 'A comparison study of the Boussinesq and the variable density models on buoyancy-driven flows', *Journal of Engineering Mathematics* **75**, 15–27.

Lee, T., Kashyap, R. & Chu, C. (1994), 'Building skeleton models via 3-d medial surface axis thinning algorithms', *CVGIP: Graphical Models and Image Processing* **56**, 462–478.

Li, H., Harvey, J., Holland, T. & Kayhanian, M. (2013), 'The use of reflective and permeable pavements as a potential practice for heat island mitigation and stormwater management', *Environmental Research Letters* **8**, 1–14.

Liu, Y. & Harris, D. (2013), 'Measurements of wind speed and convective coefficient on the external surface of a low-rise building', *International Journal of Ambient Energy* **36**, 225–234.

Loomans, M., Oversloot, H., de Bondt, A., Jansen, R. & van Rij, H. (2003), Design tool for the thermal energy potential of asphalt pavements, *in* 'Building simulation 2003 for better building design : 8th international IBPSA conference, Eindhoven, The Netherlands', pp. 745–752.

Lorensen, W. & Cline, H. (1987), Marching cubes: A high resolution 3d surface construction algorithm, *in* '14th annual conference on Computer graphics and interactive techniques, New York, New York', pp. 163–169.

Mallick, R. B., Chen, B. & Bhowmick, S. (2009*a*), 'Harvesting energy from asphalt pavements and reducing the heat island effect', *International Journal of Sustainable Engineering* **2**, 214–228.

Mallick, R. B., Chen, B. & Bhowmick, S. (2009*b*), Reduction of urban heat island effect through harvest of heat energy from asphalt pavements, *in* 'Second International Conference on Countermeasures to Urban Heat Islands, Berkeley, California'.

Mallick, R., Chen, B., , Bhowmick, S. & Hulen, M. (2008), Capturing solar energy from asphalt pavements, *in* 'ISAP 2008 Symposium, Zurich, Switzerland'.

Masad, E., Muhunthan, B., Shashidhar, N. & Harman, T. (1999), 'Internal structure characterization of asphalt concrete using image analysis', *Journal of Computing in Civil Engineering* **13**, 88–95.

Massoud, M. (2008), *Engineering thermofluids: thermodynamics, fluid mechanics, and heat transfer*, Springer, 561–578.

Medale, M. & Haddad, A. (2012), 'A 3D low mach number model for high performance computations in natural or mixed convection newtonian liquid flows', *Journal of Physics: Conference Series* **395**, 012095.

Met Office (UK) (n.d.), 'Average temperatures in Nottingham (Climate station of Watnall, UK)', `http://www.metoffice.gov.uk/public/weather/climate/gcrje93b8`. Accessed Jan. 18, 2016.

Minhoto, M., Pais, J. & Pereira, P. (2006), Asphalt pavement temperature prediction, *in* 'Asphalt Rubber Conference, Palm Springs, California', pp. 193–207.

Nasir, D., Hughes, B. & Calautit, J. (2015), 'A study of the impact of building geometry on the thermal performance of road pavement solar collectors', *Energy* **93**, 2614–2630.

Oliveira, J. R., Silva, H. M., Abreu, L. P. & Fernandes, S. R. (2013), 'Use of a warm mix asphalt additive to reduce the production temperatures and to improve the performance of asphalt rubber mixtures', *Journal of Cleaner Production* **41**, 15–22.

Padleckas, H. (2006), 'Straight-tube heat exchanger, Wikimedia Commons', `https://commons.wikimedia.org/w/index.php?curid=819134`. Accessed May 12, 2016.

Paniagua, I., Martiín, J., Fernandez, C., Álvaro, A. & Carlier, R. (2013), 'A new simple method for estimating exergy destruction in heat exchangers', *Entropy* **15**, 474–489.

Pascual-Muñoz, P., Castro-Fresno, D., Serrano-Bravo, P. & Alonso-Estébanez, A. (2013), 'Thermal and hydraulic analysis of multilayered asphalt pavements as active solar collectors', *Applied Energy* **111**, 324–332.

Paulescu, M., Paulescu, E., Gravila, P. & Badescu, V. (2013), *Weather Modeling and Forecasting of PV Systems Operation*, Springer, 17–42.

Pomerantz, M., Akbari, H., Chen, A., Taha, H. & Rosenfeld, A. H. (1997), *Paving materials for heat island mitigation*, Ernest Orlando Lawrence Berkeley National Laboratory, 1–10.

Quéré, P. L., Weisman, C., Paillère, H., Vierendeels, J., Dick, E., Becker, R., Braack, M. & Locke, J. (2005), 'Modelling of natural convection flows with large temperature differences: A benchmark problem for low mach num-

ber solvers. Part 1. Reference solutions', *ESAIM: Mathematical Modelling and Numerical Analys* **39**, 609–616.

Rodgers, J. L. & Nicewander, W. A. (1988), 'Thirteen ways to look at the correlation coefficient', *The American Statistician* **42**, 59–66.

Santamouris, M. (2013), 'Using cool pavements as a mitigation strategy to fight urban heat island - a review of the actual developments', *Renewable and Sustainable Energy Reviews* **26**, 224–240.

Sarat, A. A. & Eusuf, M. A. (2012), 'An experimental study on observed heating characteristics of urban pavement', *Journal of Surveying, Construction and Property* **3**, 1–12.

Seidel, J. C. & Haddock, J. E. (2014), 'Rheological characterization of asphalt binders modified with soybean fatty acids', *Construction and building materials* **53**, 324–332.

Sengoz, B. & Oylumluoglu, J. (2013), 'Utilization of recycled asphalt concrete with different warm mix asphalt additives prepared with different penetration grades bitumen', *Construction and Building Materials* **45**, 173–183.

Siebert, N. & Zacharakis, E. (2010), *Asphalt Solar Collector and Borehole Storage - Design study for a small residential building area*, MSc Thesis, Chalmers University of Technology, 5–20.

Siena, M., Riva, M., Hyman, J. D., Winter, C. L. & Guadagnini, A. (2014), 'Relationship between pore size and velocity probability distributions in stochastically generated porous media', *PHYSICAL REVIEW E* **89**, 013018.

Singh, R. K. & Ahmed, M. R. (2013), 'Blade design and performance testing of a small wind turbine rotor for low wind speed applications', *Renewable Energy* **50**, 812–819.

Speight, J. (2016), *Asphalt Materials Science and Technology*, Butterworth-Heinemann, 341–349.

Sreedhar, S. & Biligiri, K. (2016), 'Development of pavement temperature predictive models using thermophysical properties to assess urban climates in the built environment', *Sustainable Cities and Society* **22**, 78–85.

Stempihar, J. J., Pourshams-Manzouri, T., Kaloush, K. E. & Rodezno, M. C. (2012), 'Porous asphalt pavement temperature effects for urban heat island analysis', *Transportation Research Record: Journal of the Transportation Research Board* **2293**, 123–130.

Synnefa, A., Karlessi, T., Gaitani, N., Santamouris, M., Assimakopoulos, D. N. & Papakatsikas, C. (2011), 'Experimental testing of cool colored thin layer asphalt and estimation of its potential to improve the urban microclimate', *Building and Environment* **46**, 38–44.

Tarleton, J. (2006), 'Road Weather: Pavement Forecasting', American Public Works Association, `https://www.apwa.net/Resources/Reporter/Articles/2006/10/Road-Weather-Pavement-Forecasting`. Accessed May. 21, 2016.

Umiliaco, A. & Benedetto, A. (2013), New mathematical paradigm applied to fluid flow in porous media: the case of permeable asphalt pavement, *in* '2013 International Conference on Applied Mathematics and Computational Methods in Engineering, Rhodes Island, Greece', pp. 195–202.

Verda, V., Cosentino, S., Lo Russo, S. & Sciacovelli, A. (2014), Second law analysis of horizontal geothermal heat pump systems, *in* 'ECOS 2014 - The 27th International Conference on Efficiency, Cost, Optimization and Environmental Impact of Energy Systems, Turku, Finland'.

Wang, H., Wu, S., Chen, M. & Zhang, Y. (2010), 'Numerical simulation on the thermal response of heat-conducting asphalt pavements', *Physica scripta* **T139**.

Weather Online (2015-2016), 'Weather History in Nottingham (Climate station of Watnall, UK)', `http://www.weatheronline.co.uk/`. Accessed Jan. 18, 2016.

White, F. M. (2002), *Fluid Mechanics*, McGraw-Hill, 215–264.

WHO (2007), *Quality Assurance of Pharmaceuticals: A Compendium of Guidelines and Related Materials. Good manufacturing practices and inspection, Volume 2*, World Health Organization, 81–84.

Whyte, W. (2001), *Cleanroom Technology: Fundamentals of Design, Testing and Operation*, Wiley, 59–62.

Wu, S., Chen, M., Wang, H. & Zhang, Y. (2009), 'Laboratory study on solar collector of thermal conductive asphalt concrete', *International Journal of Pavement Research and Technology* **2**, 130–136.

Wu, S., Chen, M. & Zhang, J. (2011), 'Laboratory investigation into thermal response of asphalt pavements as solar collector by application of small-scale slabs', *Applied Thermal Engineering* **31**, 1582–1587.

Wu, S., Wang, H., Chen, M. & Zhang, Y. (2010), Numerical and experimental validation of full-depth asphalt slab using capturing solar energy, *in* '4th International Conference of Bioinformatics and Biomedical Engineering, Granada, Spain', pp. 1–4.

Xiao, F., Amirkhanian, S., Wangc, H. & Hao, P. (2014), 'Rheological property investigations for polymer and polyphosphoric acid modified asphalt binders at high temperatures', *Construction and building materials* **64**, 316–323.

Yavuzturk, C., Ksaibati, K. & Chiasson, A. (2005), 'Assessment of temperature fluctuations in asphalt pavements due to thermal environmental conditions using a two-dimensional, transient finite-difference approach', *Journal of Materials in Civil Engineering* **17**, 465–475.

Appendices

Appendix A

Preparation of connected pores for CFD simulations

The brief description of the process to generate single pores provided in Chapter 7 does not include any technical details. It is, however, interesting to explain how the steps followed to modify the pores were implemented in this work. In this Appendix, a connected air pore found with the crawling algorithm described in Section 7.1 is considered as an input. The process followed to prune and use such pore is described below.

Step 1: The image sequence created by an X-ray CT scanner or by algorithms can be opened in ImageJ and a black and white threshold can be applied.

Step 2: Using the BoneJ plugin the skeleton of the pore selected can be built (Skeletonise 3D option), as shown in Fig. A.1. The observation of the skeleton of the pore allows the user to see if there are branches of the pore that need to be pruned.

Step 3: Using the BoneJ plugin (Isosurface option, see Lorensen & Cline (1987)) the pore can be saved as a surface mesh in .stl file format.

Step 4: The .stl file can be opened with a 3D editing software of choice. In this Thesis, the free software Autodesk Meshmixer was used. Using this software, the unconnected branches seen in Fig. A.1 can be pruned manually using the sculpting tools. Afterwards, an inlet and an outlet must be added to the model in the form of two cylinders with diameter 20 mm and height 60 mm.

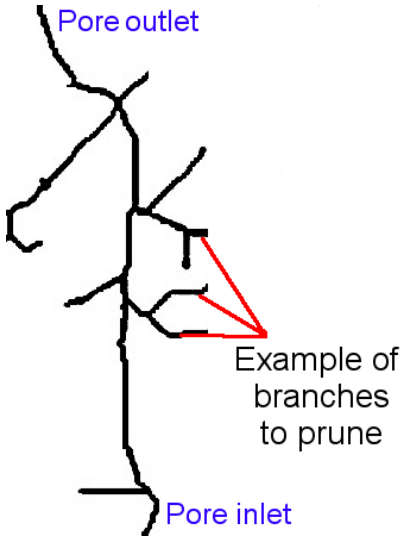

Figure A.1: Skeleton of a connected pore.

The inlet and outlet are then joined to the isolated pore by the means of the morphological operation called Boolean union. The result of this operation is a single 3D model composed of inlet, pore, and outlet.

Step 5: Before running simulations, the surface mesh needs to be converted to a suitable file format. Two options exist for this:

1. free software: a possible option is FreeCAD[1]. In this software, the .stl surface mesh can be imported and then converted to the .stp file format, which can be imported in Autodesk Simulation CFD and then meshed. In FreeCAD, this can be done using the Part menu and the options "Create shape from mesh" and then "Convert to solid". The resulting solid can be exported as an .stp file.
2. commercial software: a very simple way to deal with the .stl surface mesh is importing it in the software Avizo Fire (v.8.1) and then creating a 3D mesh (tetrahedral grid) in the .unv file format, which can be imported directly in Autodesk Simulation CFD. For further details on this process, please refer to the Avizo Fire 8 user guide.

[1]See http://www.freecadweb.org/, open source software, v0.15

It is relevant to mention that using option 1 is free but more complex. In fact, it is very important to make sure that the surface mesh of the file is suitable for 3D meshing, otherwise, Autodesk Simulation CFD will not be able to do this. As a result, a higher level of understanding of the topic is required and manual adjustments will have to be performed. On the other hand, Avizo Fire (or, possibly, other commercial software) comes with useful functions that automatically fix the surface mesh before starting the generation of a 3D tetrahedral grid. Consequently, the use of commercial software allows a much faster workflow, because an already meshed 3D file can be imported in Autodesk Simulation CFD and the simulation can be set up more quickly. An alternative to this would be the use of ICEM ANSYS 12.0, as done by Gruber et al. (2012), who performed a similar operation with ANSYS software.

In this Thesis, the first option (free software) was used. The commercial software route, however, was also tested, in order to provide a possible alternative workflow.

Once the 3D mesh is created (either in Autodesk Simulation CFD following option 1 or in Avizo Fire using option 2), a chosen simulation can be set up.

Appendix B

List of papers

The following list shows the papers that have been published in the context of the Ph.D. research carried out by the author:

1. Chiarelli, A., Dawson, A. & García, A. (2015a), 'Analysis of the performance of an air-powered energy harvesting pavement', Transportation Research Record: Journal of the Transportation Research Board 2523, 156–163.
2. Chiarelli, A., Dawson, A. & García, A. (2015d), 'Parametric analysis of energy harvesting pavements operated by air convection', Applied Energy 154, 951–958.
3. Chiarelli, A., Dawson, A. & García, A. (2016d), Mitigation of asphalt pavement temperatures by the means of natural air convection, in '4th International CEW, Delft, The Netherlands'.

Further publications are currently under peer-review and, thus, are not included in this list.